2018

STUDIES OF MAGNETICALLY INDUCED FARADAY ROTATION BY POLARIZED HELIUM-3 ATOMS

Joshua Abney
University of Kentucky, mttc34@gmail.com
Digital Object Identifier: https://doi.org/10.13023/etd.2018.377

STUDENT AGREEMENT:

I represent that my thesis or dissertation and abstract are my original work. Proper attribution has been given to all outside sources. I understand that I am solely responsible for obtaining any needed copyright permissions. I have obtained needed written permission statement(s) from the owner(s) of each third-party copyrighted matter to be included in my work, allowing electronic distribution (if such use is not permitted by the fair use doctrine) which will be submitted to UKnowledge as Additional File.

I hereby grant to The University of Kentucky and its agents the irrevocable, non-exclusive, and royalty-free license to archive and make accessible my work in whole or in part in all forms of media, now or hereafter known. I agree that the document mentioned above may be made available immediately for worldwide access unless an embargo applies.

I retain all other ownership rights to the copyright of my work. I also retain the right to use in future works (such as articles or books) all or part of my work. I understand that I am free to register the copyright to my work.

REVIEW, APPROVAL AND ACCEPTANCE

The document mentioned above has been reviewed and accepted by the student's advisor, on behalf of the advisory committee, and by the Director of Graduate Studies (DGS), on behalf of the program; we verify that this is the final, approved version of the student's thesis including all changes required by the advisory committee. The undersigned agree to abide by the statements above.

<div align="right">

Joshua Abney, Student

Dr. Wolfgang Korsch, Major Professor

Dr. Chris Crawford, Director of Graduate Studies

</div>

STUDIES OF MAGNETICALLY INDUCED FARADAY ROTATION BY
POLARIZED HELIUM-3 ATOMS

—————————————————

DISSERTATION

—————————————————

A dissertation submitted in partial
fulfillment of the requirements for
the degree of Doctor of Philosophy
in the College of Arts and Sciences
at the University of Kentucky

By
Joshua Abney
Lexington, Kentucky

Director: Dr. Wolfgang Korsch, Professor of Physics
Lexington, Kentucky 2018

ABSTRACT OF DISSERTATION

STUDIES OF MAGNETICALLY INDUCED FARADAY ROTATION BY
POLARIZED HELIUM-3 ATOMS

Gyromagnetic Faraday rotation offers a new method to probe limits on properties of simple spin systems such as the possible magnetic moment of asymmetric dark matter or as a polarization monitor for polarized targets. Theoretical calculations predict the expected rotations of linearly polarized light due to the magnetization of spin-1/2 particles are close to or beyond the limit of what can currently be measured experimentally (10^{-9} rad). So far, this effect has not been verified. Nuclear spin polarized ^{3}He provides an ideal test system due to its simple structure and ability to achieve high nuclear spin polarization via spin-exchange optical pumping (SEOP). To maximize the expected signal from ^{3}He, a SEOP system is built with a modern narrowband pumping laser and a ^{3}He target designed to use with a multipass cavity. Additionally, a sensitive triple modulation apparatus for polarimetry is utilized and further developed to detect Faraday rotations on the order of nanoradians. This works presents the results of the measurement of the magnetic Faraday effect.

KEYWORDS: polarized ^{3}He, optical rotation, Faraday effect, precision measurement, magneto-optical physics

Author's signature:　　　　Joshua Abney

Date:　　　　October 2, 2018

STUDIES OF MAGNETICALLY INDUCED FARADAY ROTATION BY
POLARIZED HELIUM-3 ATOMS

By
Joshua Abney

Director of Dissertation: Wolfgang Korsch

Director of Graduate Studies: Chris Crawford

Date: October 2, 2018

To my wonderful wife Angela and my daughter Felicity

ACKNOWLEDGMENTS

I would first like to thank my advisor, Wolfgang Korsch. His guidance throughout my graduate school career helped me to develop the ability to think and work as an independent researcher. Wolfgang's excellent knowledge of, and passion for, physics bolstered my own interest in the subject over the years. And his support and constant positive attitude, especially when there were difficulties in the lab, encouraged me to keep working at it.

I would like to thank my committee members, Susan Gardner, Renee Fatemi, and Robert Adams for their insight and feedback. Thanks to the guys in the machine shop and the electronics shop whose expertise and many parts they built for me helped me greatly. Also, thanks to my friends in the department for the time we spent together, especially Mark and Murchhana for all the help in the lab.

Thanks to my family and close friends for their encouragement and the fun times we had that provided a welcomed distraction from research.

Finally, I would like to thank my wife Angela. For celebrating the good times with me, supporting me through the not so good times, and the endless hours spent listening to practice talks. Without her this work would not have been possible.

TABLE OF CONTENTS

xiii

Chapter 1 Introduction

1.1   Introduction

Precision measurements are a important part of modern physics, providing increasingly stringent tests of the Standard Model in the effort to confirm its predictions and search for new physics. For example, the Standard model predicts very small permanent electric dipole moments for several particles such as the electron and neutron. There are many precision measurement experiments underway to put limits on the size of these EDMs. The unknown nature of dark matter, which takes up 24% percent of the energy budget of the universe, has also instigated a number of precision measurement experiments which seek any small interaction it may have with normal matter or its possible decay products. One theoretical method [1] was developed to detect Dark Matter through such a precision measurement experiment involving a Faraday effect from bare magnetic moments.

Especially in recent years the Faraday effect has evolved into a precision tool for a variety of applications. For example, it is used to measure permanent electric dipole moments in atoms [2], to determine magnetic field strengths and directions in the intergalactic medium [3], as part of precision magnetometers to test fundamental symmetries [4], to measure spin-noise [5], or to probe the process of light squeezing [6]. However, these applications involve the interaction of the probe light with the electric charge and thus the rotations are induced by electric polarizabilities of the studied systems. The theory of the interaction of light with electric free or bound charges is well established and is described classically and quantum mechanically [7]. In addition to this electrically induced rotation a similar effect should exist due to the magnetic interaction of light. This so called gyromagnetic Faraday effect is significantly weaker and it exhibits, to leading order, no dependence on the frequency of the probe light in contrast to its electric counterpart. The experimental verification of this magnetic Faraday effect would open up possibilities for studies of fundamental properties of Dark Matter, such as putting limits on possible anomalous magnetic

moments of composite low-mass Dark Matter particles [1]. In order to investigate the magnetically induced rotation, a neutral particle with minimal intrinsic structure and an anomalous magnetic moment is the ideal candidate. A system that has several of the advantages is ^{3}He. This helium isotope is predominantly in a singlet S ground state at room temperature and it has a spin-1/2 nuclear ground state with a magnetic moment of $-2.12\mu_N$. Additionally, two well developed technologies exist to produce relatively dense and nuclear spin-polarized targets with high values of polarization. Further applications can be considered, as the effect can be utilized as a new method to monitor the polarization of a dense target. This is useful for experiments that operate with a polarized helium target where the polarization has to be measured with magnetic resonance techniques.

1.2 Thesis Overview

This thesis presents the results of an experiment to measure the gyromagnetic Faraday rotation from a dense polarized ^{3}He gas. Chapter 2 gives an overview of the polarization of light and the Faraday effect. It describes the theory of the Faraday effect and how the gyromagnetic Faraday effect is derived. It concludes with a calculation of the expected rotation angle from ^{3}He. Chapter 3 describes how optical rotation angles are measured and the specific apparatus used in this experiment. It covers the triple modulation technique and the systematic studies done to determine the angular sensitivity of the setup. Chapter 4 begins with the a description of the spin exchange optical pumping process and how it polarizes the helium nucleus. It then covers the setup and target cells used in the experiment and how the helium polarization is measured. The chapter ends with what the helium polarization looks like during spin modulation. The final chapter describes the magnetic Faraday effect experiment. It begins by describing the multipass cavity and the simulations done to chose the right mirrors. It covers the full setup of the polarimetry apparatus combined with the polarized helium target. Then explains how a measurement is performed and the data is collected. It ends with the final results from the experiment and all the systematic studies done to find a reason as to why the magnetic

Faraday effect was not found in helium.

Chapter 2 Theory

The polarization of light provides a powerful tool to investigate a variety of systems and effects. As soon as light interacts through reflection, transmission, or scattering there is the opportunity for polarization to be introduced or the state of polarization to change. In particular, optical rotation, which is when the rotation of the plane of linear polarization is rotated due to circular birefringence, is a broad area of research. It is commonly used in density measurements of spin polarized gases [8, 9], as a probe to measure atomic EDM's [2], as part of sensitive co-magnetometers [10, 11], to determine concentrations of chiral molecule in solution, and to explore nuclear spin polarized mediums [12, 13]. This chapter will cover the basic characterization of light polarization, the theory of light interacting with magnetic fields and the Faraday effect, probing systems with light polarization and how to measure it, and the theory behind the gyromagnetic Faraday effect.

2.1   Polarization of Light

Light is a transverse wave made of electric and magnetic fields oscillating perpendicular to each other and the direction of propagation. By convention, the polarization of an electromagnetic wave is defined to be the direction of the electric field vector. There are three different bases of light polarization, linear polarization is when the electric field is confined to a plane along the direction of propagation, circular polarization is when the electric field vector does not change strength but rotates about the propagation axis tracing a circle in a plane perpendicular to the direction of travel, and elliptical polarization in which the electric field vector traces out an ellipse. Figure(2.1) is a graphical representation of the states. Mathematically, if the light travels along the $\hat{z}$ axis the two orthogonal components of the electric field can be written as

$$E_x = E_{0x} \cos\left(kz - \omega t + \delta_x\right)$$
$$E_y = E_{0y} \cos\left(kz - \omega t + \delta_y\right).$$

(2.1)

a) Elliptical polarization

b) Linear polarization

c) Circular polarization
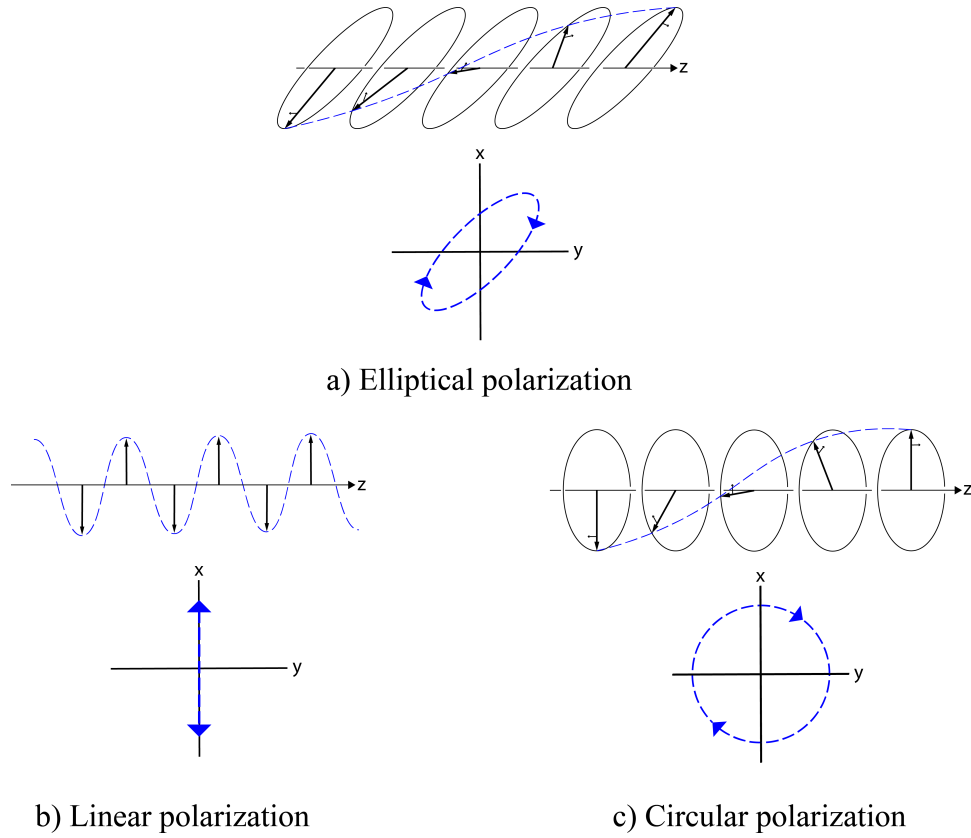
Figure 2.1: The three bases for the two states of polarized light. The electric field vector traces out the shape in a plane normal to the direction of propagation.

E_{0x}, E_{0y} are the maximum amplitudes in the respective directions, ω the angular frequency, k the wave number, and δ_x, δ_y are the phases of the oscillations. Eliminating the common components and combining the equations gives

$$\left(\frac{E_x}{E_{0x}}\right)^2 + \left(\frac{E_y}{E_{0y}}\right)^2 - 2\frac{E_x}{E_{0x}}\frac{E_y}{E_{0y}}\cos\left(\delta_y - \delta_x\right) = \sin^2\left(\delta_y - \delta_x\right). \qquad (2.2)$$

This is the equation of an ellipse, hence the most general state of polarization is when locus of points traced out by the electric field vector form an ellipse on a plane normal to the direction the light travels in. The polarization ellipse is shown in Fig.(2.2) and is characterized by the amplitudes E_{0x}, E_{0y} and phases δ_x, δ_y [14]. The semi-major (a) and and semi-minor (b) axes are

5
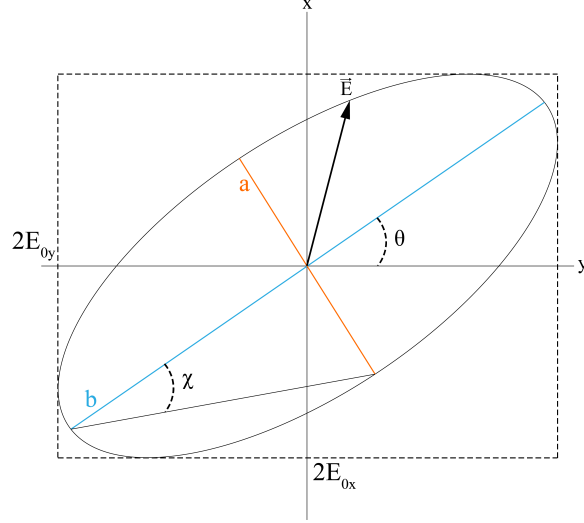
Figure 2.2: The polarization ellipse of elliptically polarized light. The ellipse is described by the semi-major and semi-minor axis and the angle with the coordinate axis.

$$a = \sqrt{(E_{0x}^2 + E_{0y}^2)} \sqrt{\frac{1 + \sqrt{1 - \sin^2(2\theta)\sin^2(\delta_y - \delta_x)}}{2}}$$

$$b = \sqrt{(E_{0x}^2 + E_{0y}^2)} \sqrt{\frac{1 - \sqrt{1 - \sin^2(2\theta)\sin^2(\delta_y - \delta_x)}}{2}} \qquad (2.3)$$

$$\tan(2\theta) = \frac{2E_{0x}\dot{E}_{0y}}{(E^2_{0x} - E^2_{0y})}\cos(\delta_y - \delta_x).$$

The quantity θ is defined as the angle between the semi-major axis and the $\hat{x}$ axis. From this it is clear that linear and circular polarization are special cases of elliptical polarization. Linear polarization is where $\delta_y - \delta_x = 0$ and the locus of points collapses to a straight line at angle θ. Typically, the convention is to call linearly polarized light s or p polarized if the plane of polarization is normal or perpendicular to the plane of incidence, respectively. Circular polarization is when $\delta_y - \delta_x = \pm\pi/2$ and $\theta = \pi/4$, the electric field vector has constant amplitude and rotates at a constant rate forming a circle. Additionally, when viewed along the propagation axis it can rotate clockwise or counterclockwise which are further defined as right and left circular polarization.

With this, linear polarized light can be regarded as the sum of a right circularly polarized beam and a left circularly polarized beam of equal amplitude and the orientation angle θ is the result of the relative phases of the two beams as shown in Fig.(2.3). Writing the electric field of right (σ^+) and left (σ^-) circular polarization as

$$\vec{\mathbf{E}}_+ = \frac{E_0}{2}[\cos{(kz - \omega t)}\hat{\mathbf{x}} - \sin{(kz - \omega t)}\hat{\mathbf{y}}]$$
$$\vec{\mathbf{E}}_- = \frac{E_0}{2}[\cos{(kz - \omega t)}\hat{\mathbf{x}} + \sin{(kz - \omega t)}\hat{\mathbf{y}}], \tag{2.4}$$

and then taking a superposition of the two equations yields $\vec{\mathbf{E}} = E_0 \cos{(kz - \omega t)}\hat{\mathbf{x}}$ which is a linear polarized beam along the $\hat{x}$ axis. If this linearly polarized beam passes through some medium that has different refractive indices for the right and left circular components (n_+ and n_-) each component will acquire a phase $\phi_+ = \omega t - \frac{\omega z}{c}n_+$ and $\phi_- = \omega t - \frac{\omega z}{c}n_-$. After traveling a distance d in the medium the phase difference will be $\phi_- - \phi_+ = \frac{\omega d}{c}(n_- - n_+)$ and the superposition of the components becomes
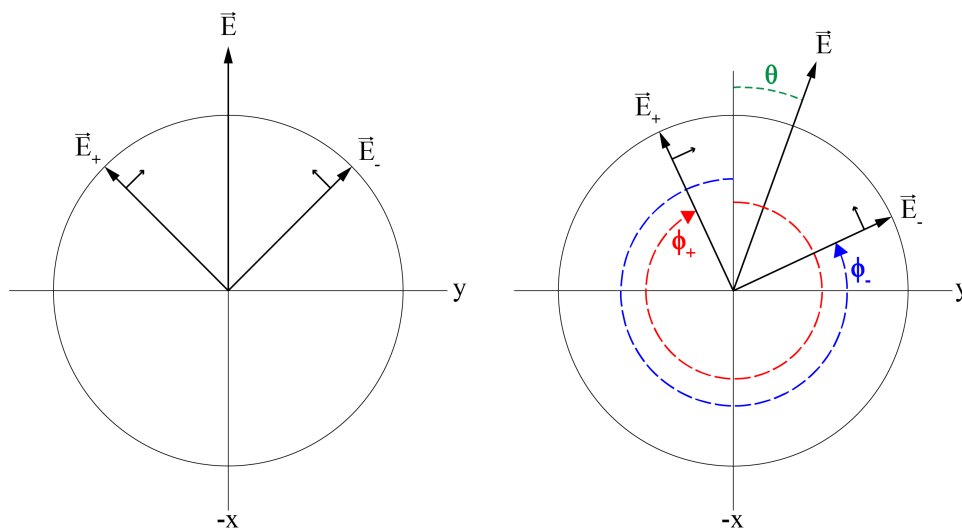
Figure 2.3: Linearly polarized light can be decomposed into two circular polarized components. A phase shift between the components will cause the plane of polarization of the light to be rotated by an angle θ.

7

$$\vec{\mathbf{E}} = E_0 \cos\left(\frac{\omega d}{c}\frac{(n_- + n_+)}{2} - \omega t\right)\left[\cos\left(\frac{\omega d}{c}\frac{(n_- - n_+)}{2}\right)\hat{\mathbf{x}} + \sin\left(\frac{\omega d}{c}\frac{(n_- - n_+)}{2}\right)\hat{\mathbf{y}}\right].$$

(2.5)

Equation(2.5) shows that the light is still linearly polarized, the electric field has equal amplitude in both $\hat{x}$ and $\hat{y}$ directions, but the plane of polarization has been rotated Fig.(2.3) by an angle

$$\theta = \frac{\omega d}{c}\frac{(n_- - n_+)}{2}.$$

(2.6)

This effect, where a material has different indices of refraction for right and left circularly polarized light, is called circular birefringence. When it occurs naturally the rotation of linearly polarized light is referred to as optical activity. Chiral molecules, which have non-superposable mirror images of themselves, produce natural optical activity due to a lack of mirror symmetry. Simple sugars such dextrose and fructose are examples of this. These molecules have mirror image counter parts and each of the distinct molecular orientations will respond to right and left circularly polarized light in a different way, resulting in different indices of refraction. An important note about optical activity is that if light passing through a medium is rotated by an angle θ by passing through the medium in the opposite direction it will be rotated by the exact opposite $-\theta$ and the effect will cancel.

In addition to the polarization ellipse, the state of light polarization can further be parameterized through the Jones calculus or with Stokes parameters. The Jones calculus uses a two element vector to represent the state of light polarization where the elements are the relative amplitude and phase of the two orthogonal components E_x and E_y. Anything the light interacts with can then be written as a 4x4 matrix that acts on the two dimensional vector, optical components such as polarizers and wave plates have well defined matrices, and the final state of polarization is extracted from the product of these matrices and the initial vector. Stokes vectors are very similar except they us a 4 vector to describe the polarization state where the 4

8

elements are defined as follows [15]

$$\begin{pmatrix} S_0 \\ S_1 \\ S_2 \\ S_3 \end{pmatrix} = \begin{pmatrix} E_x^2 + E_y^2 \\ E_x^2 - E_y^2 \\ 2E_xE_y\cos(\delta_x - \delta_y) \\ 2E_xE_y\sin(\delta_x - \delta_y) \end{pmatrix} = \begin{pmatrix} I \\ Ip\cos(2\theta)\cos(2\chi) \\ Ip\sin(2\theta)\cos(2\chi) \\ Ip\sin(2\chi) \end{pmatrix}. \tag{2.7}$$

The first parameter S_0 is the total intensity of the light, the second S_1 is the difference between the squares of s and p linear polarizations, S_3 is the difference between linear polarizations at $\pm 45^o$, and S_4 the difference between intensity of right and left circular polarizations. The angles θ and χ are definded in Fig.2.2. The main advantage of Stokes vectors is describing partial or un-polarized light, with the degree of polarization $p = \frac{\sqrt{S_1^2 + S_2^2 + S_3^2}}{S_0}$. They have the same function as Jones matrices as the final state of polarization is calculated by multiplying the initial state with matrices of all the optical components.

2.2 Faraday Effect

Magneto optic effects arise when light interacts with a medium that is inside a magnetic field. These effects have been studied for nearly 200 years and have had a profound impact on the development of modern physics. The most prominent of these is the Faraday effect. It was discovered by Michael Faraday in 1845 as the first evidence that light and magnetism are related by showing that a magnetic field affects light polarization. In his experiment a beam of linearly polarized light was incident on a linear polarizer, which he then rotated until the light was extinguished. He placed a piece of glass in the path of the light and observed no change in intensity after the polarizer. When he placed the glass between the poles of a magnet however, suddenly the light was no longer extinguished indicating that the plane of polarization had changed. He further showed that the intensity of light varied with the strength of the magnetic field [16]. Thus, the Faraday effect is when a material placed inside a magnetic field becomes optically active, inducing a rotation of the plane of polarization of linearly polarized light, along the direction of the magnetic

field. Fig.(2.4) is a graphical representation. In its most simple, classic form the angle of rotation is proportional to the strength of the magnetic field B and the length of the optical path in the medium d
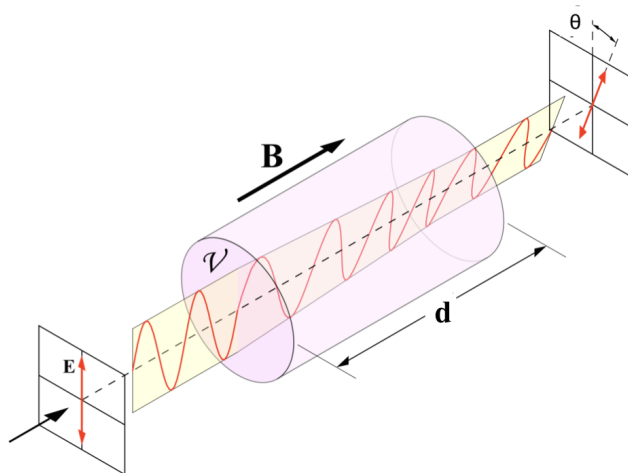
Figure 2.4: The Faraday effect. Linearly polarized light passing through a medium in a magnetic field along the direction of light travel will acquire a rotation of the plane of polarization. Figure adapted from Wikipedia.

$$\theta = VBd. \tag{2.8}$$

The rotation angle is also proportional to V, called the *Verdet Constant*, which is a material dependent constant that depends on the properties of the material as well as temperature and wavelength [17]. By convention, a positive Verdet constant corresponds to counterclockwise rotation when the direction of propagation is parallel to the applied magnetic field and clockwise when antiparallel [18]. This leads to the important result, in contrast to natural optical activity, that if a beam of light passes through and acquires a rotation θ, upon being reflected and passing through in the opposite direction that rotation will double 2θ rather than cancel. The Faraday effect, like natural optical activity, is a result of circular birefringence. The classical physical interpretation is the electrons in a material are modeled as tiny oscillators

circling an external magnetic field. From these electron oscillations the left and right handed circular components of a linearly polarized wave accumulate a phase difference and thus a rotation as in Eq.(2.6). The picture is too simple however, as the complicated electronic structures of practical materials do not allow a quantitative analysis. A more robust classical and quantum description of the Faraday effect involving the calculation of the different refractive indices (n_+ and n_-) will be discussed. An electromagnetic wave propagating through a medium inside an external magnetic field $\vec{H}$, absent macroscopic charges and currents, will induce electric and magnetic moments $\vec{m}$ and $\vec{\mu}$. To first order in the electromagnetic field of the light the components of these moments are given in Ref.[7]

$$
\begin{aligned}
m_x &= \alpha_{xy}E'_y + \beta_{xy}H'_y \\
\mu_x &= \gamma_{xy}E'_y + \chi_{xy}H'_y.
\end{aligned}
\tag{2.9}
$$

Where α and χ are the electric and magnetic polarizability tensors and β and γ are tensors related to natural optical activity. The electric displacement and magnetic induction are

$$
\begin{aligned}
\vec{D} &= \vec{E}' + 4\pi \sum_a N_a \vec{m}^a \\
\vec{B} &= \vec{H}' + 4\pi \sum_a N_a \vec{\mu}^a,
\end{aligned}
\tag{2.10}
$$

N_a is the number of molecules per unit volume in state a. The polarizability tensors are functions of the static external magnetic field $\vec{H}$, therefore $\alpha_{xy} = \alpha^0_{xy} + \alpha^1_{xyz}H_z...$ and in an isotropic medium ($\alpha^0_{xy} = \alpha_0 \delta_{xy}$ and $\alpha^1_{xyz} = \alpha_1 \varepsilon_{xyz}$) the induced moments can be written as

$$
\begin{aligned}
\vec{m} &= \alpha_0 \vec{E}' + \beta_0 \vec{H}' + \alpha_1(\vec{E}' \times \vec{H}) + \beta_1(\vec{H}' \times \vec{H}) \\
\vec{\mu} &= \gamma_0 \vec{E}' + \chi_0 \vec{H}' + \gamma_1(\vec{E}' \times \vec{H}) + \chi_1(\vec{H}' \times \vec{H}).
\end{aligned}
\tag{2.11}
$$

From Eq.(2.11) it can be seen that $\vec{m}$ and $\vec{E}'$ are vectors while $\vec{\mu}$ and $\vec{H}$ and $\vec{H}'$ are axial-vectors. This means $\beta_0, \beta_1, \gamma_0$ and γ_1 are only nonzero if the medium is different in two different frames, or it is optically active. If the light is reflected back through, right circular polarization becomes left and left becomes right therefore

natural optical rotation cancels and Faraday rotation doubles since the sign of $\vec{H}$ is different for the opposite direction [7]. Because optical rotation comes from the difference in refractive indices for circularly polarized light we want to write the equation for the electric field of circularly polarized light as

$$\vec{E}_{\pm} = E_0 e^{i\omega(t - \tilde{n}_{\pm} \frac{z}{c})} (\hat{x} \pm i\hat{y}). \tag{2.12}$$

The complex index of refraction is $\tilde{n} = n - ik$, where n and k are the real refractive index and absorption coefficient, respectively. This complex index of refection can then be solved for using Eq.(2.9-2.12) and Maxwell's equations. The result is [7]

$$\tilde{n}_{\pm} = 1 + 2\pi \sum_a N_a \{\alpha_0^a + \chi_0^a \mp i\beta_0^a \pm i\gamma_0^a + [\pm\alpha_1^a \pm \chi_1^a + \beta_1^a - \gamma_1^a]H_z\}. \tag{2.13}$$

The complex rotation Φ is

$$\begin{aligned} \Phi = \theta - i\phi &= \frac{\omega}{2c}(\tilde{n}_- - \tilde{n}_+) \\ \theta = \frac{\omega}{2c}(n_- - n_+) &\qquad \phi = \frac{\omega}{2c}(k_- - k_+). \end{aligned} \tag{2.14}$$

Where θ is the rotation of the plane of polarization and ϕ is the ellipticity usually referred to as circular dichroism. Combining Eq.(2.13) and Eq.(2.14) yields

$$\Phi = -\frac{2i\pi\omega}{c} \sum_a N_a \{-\beta_0^a + \gamma_0^a + [\alpha_1^a \pm \chi_1^a]H_z\}. \tag{2.15}$$

The total complex rotation is thus a combination of natural optical activity and the magnetic optical activity. The electric polarizability α_1 and the magnetic polarizability χ_1 are responsible for the Faraday effect, when there is no external field ($H_z = 0$) they disappear. The other terms in Eq.(2.15) are responsible for natural optical activity. In this classical description these effects arise from the components of the induced moments perpendicular to the electric and magnetic fields of the light. The scale of the polarizability is $\alpha_1 \gg \chi_1, \beta_1, \gamma_1$, for reasonable magnetic fields the Faraday rotation and optical activity rotation are of the same magnitude so the dominate contribution to the Faraday effect comes from the electric polarizability.

It is also useful to describe the Faraday effect from a quantum mechanical viewpoint. The effect is still due to circular birefringence; however, the difference in the index of refraction for the two circular polarizations comes from the Zeeman splitting of the atomic or molecular states in the presence of a magnetic field. The Zeeman effect splits the degenerate energy levels by a small amount resulting in different indices as the various energy sublevels only respond to left or right circular polarization shown in Fig.(2.5). Consider an atom inside a magnetic field, the Hamiltonian of the atom will be

$$\mathcal{H} = \mathcal{H}_0 - \vec{\mu} \cdot \vec{B}, \tag{2.16}$$

with the magnetic moment $\vec{\mu} = \mu_B(g_l \vec{L} + g_s \vec{S})$, $\vec{L}$ and $\vec{S}$ are the orbital and spin angular momentum with the nuclear spin being ignored for simplicity, coupling to the external magnetic field and producing a perturbation with energy splitting

$$\Delta E_{m_j} = \mu_B g_j B m_j, \tag{2.17}$$
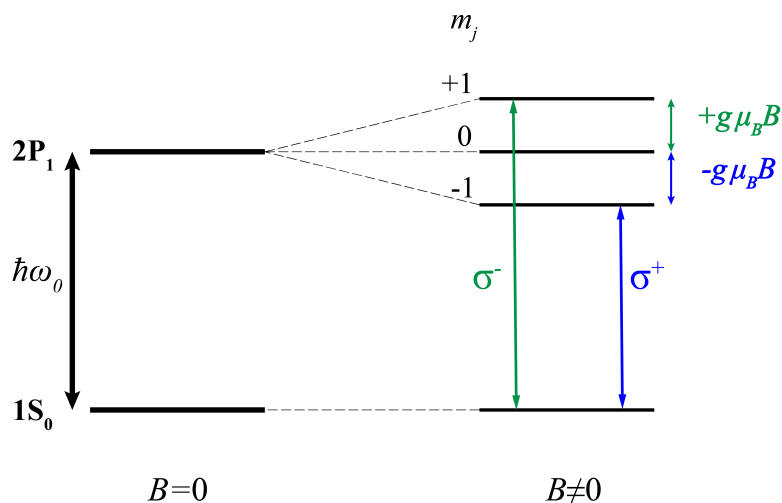
Figure 2.5: Splitting of energy levels due to Zeeman effect for a $S_0 \rightarrow P_1$ transition. Due to conservation of angular momentum only right circular polarized light (σ^+) will excite to the $m_j = -1$ state and left circular polarized (σ^-) will excite to the $m_j = +1$ state.

where g_j is Landé g factor, μ_B is the Bohr magneton, B is the external magnetic field amplitude, and m_j is the z component of the total angular momentum with a (2j+1) degeneracy ($j = l + s$). For a hypothetical resonance between a non-degenerate ground state S_0 and a triple degenerate excited state P_1, in an external magnetic field the excited state will be split into three states with energy difference between them given by Eq.(2.17). When light is incident upon this medium, the electric dipole selection rules state that only transitions involving $m_j \pm 1$ are allowed. Right circular polarized light (σ^+) carries angular momentum of $-1\hbar$ and left circular polarized (σ^-) light has angular momentum of $+1\hbar$ and in order to conserve angular momentum the three transitions of the simple $S_0 \rightarrow P_1$ resonance become circular polarization selective. The ground state to $m_j = -1$ absorbs only σ^+ photons, while $m_j = +1$ absorbs only σ^- photons, see Fig.(2.5). In addition, the energy shift from the Zeeman effect means these two states will have different resonance frequencies. A simple dispersive model of the index of refraction near a resonant transition can be found in Ref.[19]

$$n^2(\omega) \approx 1 + \left(\frac{Nq_e^2}{4\pi\epsilon_0 m_e}\right)\frac{1}{\omega_0^2 - \omega^2 + i\gamma\omega}. \tag{2.18}$$

N is the number of atoms or molecules, ω_0 is the resonance frequency, and γ is the resonance linewidth. For linearly polarized light of a single frequency that can be written as the superposition of left and right circularly polarized light the refractive index will be shifted due to the Zeeman effect by

$$n^2(\omega) \approx 1 + \left(\frac{Nq_e^2}{4\pi\epsilon_0 m_e}\right)\frac{1}{(\omega_0 \pm g\mu_B B)^2 - \omega^2 + i\gamma\omega}. \tag{2.19}$$

The result of this shift is shown in Fig.(2.6) where the refractive index is plotted as a function of wavelength and there is an example resonance at 400 nm. Only the real part of the refractive index is shown as the imaginary part leads to absorption and is related to the ellipticity of the light.

Thus applying an external magnetic field to a medium splits the degenerate energy states due to the Zeeman effect, this energy splitting, along with the conservation of angular momentum, results separate shifts of the frequency of a atomic or molecular
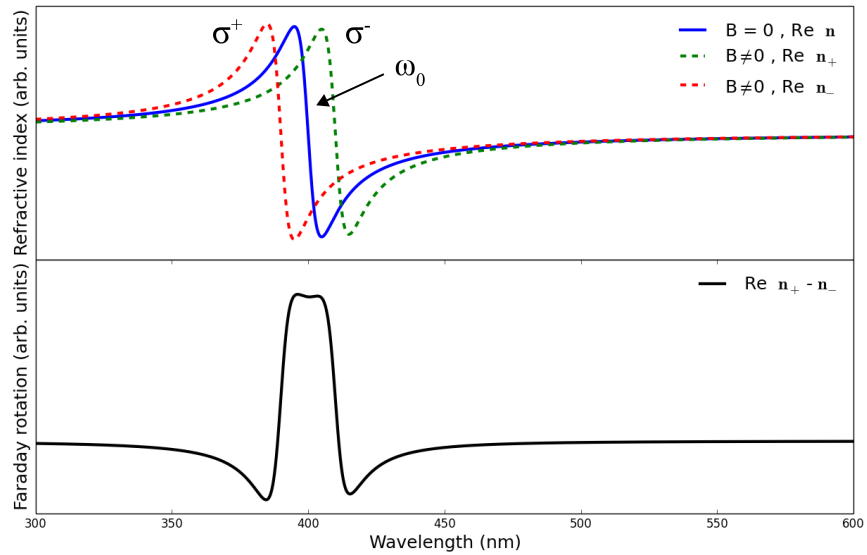
Figure 2.6: The shift in refractive index for right and left circularly polarized light due to the shift in resonance frequency from the Zeeman effect. The shift is exaggerated with a large B field and line width to show the qualitative features of the graph. The bottom plot shows the difference between the two refraction indices and is proportional to the Faraday rotation.

resonance for right and left circularly polarized light. The shifted frequencies means there will be a different index of refraction for each state of light and the medium will be circularly birefringent. The birfringence is the cause of the Faraday effect from Eq.(2.14). Near the transition frequency, as seen in Fig.(2.6), the Faraday rotation becomes exceptionally large and is usually referred to as the resonant Faraday effect or the Macaluso-Corbino effect [20]. This analysis is based only on a single transition; however, when the wavelength of the light is near the resonance the two states form the majority contribution to the optical rotation. In practice, all of the atomic or molecular states should be considered especially when the wavelength of the probe light is far from any resonance. Following the work in Ref.[7, 21, 22] Eq.(2.13) can

be written as

$$n_\pm \approx 1 + \frac{1}{4}\mu_0 c^2 N[(\alpha_{xx} + \alpha_{yy}) \pm i(\alpha_{xy} - \alpha_{yx})]. \tag{2.20}$$

Dropping the terms for natural optical activity and the magnetic polarizability tensor as the electric part usually dominates. The rotation can be written as

$$\theta = \frac{1}{2}\mu_0 c\omega L N \alpha'_{xy}. \tag{2.21}$$

where L is the path length, ω the frequency, and $\alpha'_{xy} = (\alpha_{xy} - \alpha_{yx})/2$. Using perturbative analysis and staying away from regions of absorption (e.g resonances)

$$\alpha'_{xy} = -\frac{2}{\hbar}\sum_{j=1}^{d_q} p_{q_j} \sum_{p \neq q_j} \frac{\omega}{\omega_{pq}^2 - \omega^2} Im(\langle q|\mu_x|p\rangle \langle p|\mu_y|q\rangle), \tag{2.22}$$

p_{q_j} is the relative population distribution of the Zeeman sublevel q. When there is no external magnetic field the sum in Eq.(2.22) is zero as the contribution from a state p and the complementary states q of degenerate states will have opposite signs. An external magnetic field along the direction of light propagation breaks this energy level symmetry. According to first order perturbation theory the populations and transition frequencies are shifted leading to a new expression for α'_{xy} [21]

$$\alpha''_{xy} = \alpha'_{xy} + \alpha'^{(P)}_{xy} B_z, \tag{2.23}$$

$$\alpha'^{(P)}_{xy} = -\frac{2\omega}{\hbar^2}\sum_j p_{q_j} \sum_{p \neq q_j} \left\{ \frac{2\omega_{pq}}{\omega_{pq}^2 - \omega^2}(\langle p|m_z|p\rangle - \langle q|m_z|q\rangle)Im(\langle q|\mu_x|p\rangle \langle p|\mu_y|q\rangle) \right.$$

$$+ \frac{1}{\omega_{pq}^2 - \omega^2}\left[\sum_{u \neq q}\frac{1}{\omega_{uq}}Im(\langle u|m_z|q\rangle (\langle q|\mu_x|p\rangle \langle p|\mu_y|u\rangle - \langle q|\mu_y|p\rangle \langle p|\mu_x|u\rangle))\right.$$

$$\left.\left.+ \sum_{u \neq p}\frac{1}{\omega_{up}}Im(\langle p|m_z|u\rangle (\langle q|\mu_x|p\rangle \langle u|\mu_y|q\rangle - \langle q|\mu_y|p\rangle \langle u|\mu_x|q\rangle))\right]\right\}. \tag{2.24}$$

The u states are the shifts due to the external magnetic field. Therefore, the general form of the Faraday rotation angle is

$$\theta = \frac{1}{2}\mu_0 c\omega L N \alpha'^{(P)}_{xy} B_z. \tag{2.25}$$

The caveat to this formula is when the population levels are distributed through other means than thermal Boltzmann distributions such as through optical pumping. Faraday rotations from such mechanisms require a different analysis. Even when the light wavelength is far away from any resonance the collective Zeeman shift of all the states due to an external magnetic field is responsible for the Faraday effect.

The quantum mechanical description of the Faraday effect relies upon the fact that the interaction of the electromagnetic wave and the medium is controlled almost entirely by the electric polarizability tensor. The classical description as well can be approximated assuming the magnetic contribution of the Faraday effect from the magnetic polarizability is much smaller than the electric part. These theoretical approximations usually agree with experimental data very well and formulas such as Eq.(2.26) and Eq.(2.14) are sufficient to describe the Faraday rotation from a material. However, there are some experiments that suggest that the magnetic part of the Faraday rotation is measurable. J.T. Hougen shows in Ref.[18] that the Verdet constant calculated in Ref[7] can be written as the sum of two terms

$$V = V_e + V_m. \tag{2.26}$$

V_e is the from the interaction of the electric field of the light with the medium in an external magnetic field and V_m is the interaction of the magnetic field of the light with the medium. Both terms share a quadratic dependence on the frequency of the light but for the O_2 molecule there is an extra term in V_m that arises from the coupling of the magnetic moment m of the molecule with the various spin-rotational states of the $^3\Sigma$ ground state that is frequency independent. This term could be separated from the other Verdet constant constituents by changing the frequency of the probe light, where it would be measured as an offset. Such experimental data exist for O_2 and exhibit the expected offset (see Fig.(2.7)), suggesting that this purely magnetic contribution to the Faraday effect can be measured. This leads to other considerations of magnetic Faraday interactions to be discussed in the next section.
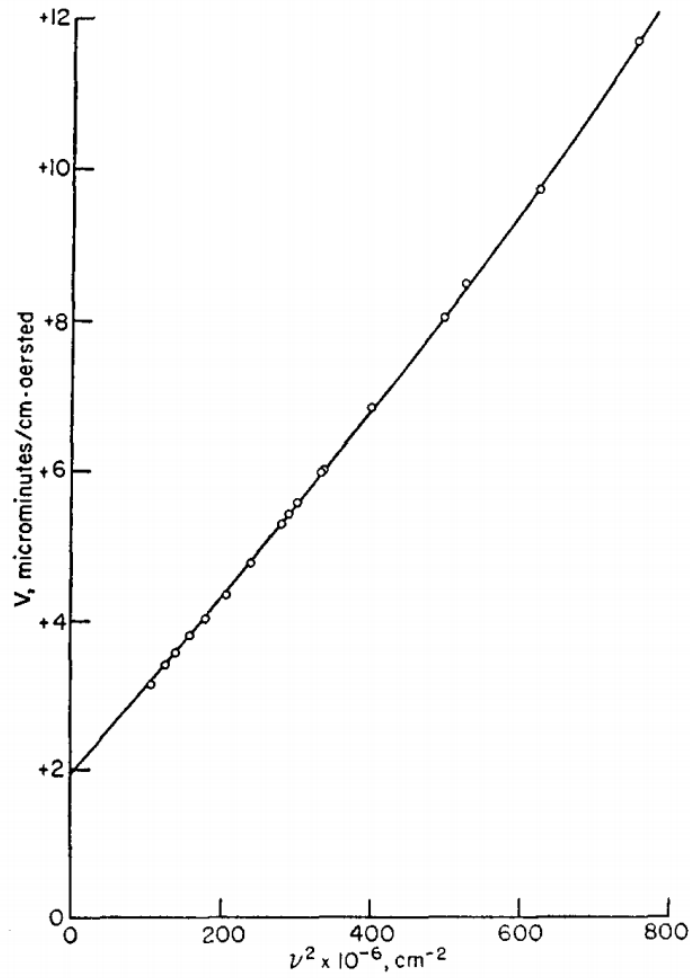
Figure 2.7: The Verdet constant for O_2 as a function of probe light wavelength. The curve shows the expected $1/\lambda^2$ dependence with an offset that may be caused by a purely magnetic contribution to the Faraday effect.[18]

2.3 Gyromagnetic Faraday Effect

Aside from the experimental data for the Verdet constant of O_2, other early work that leads to a theory of a magnetic Faraday effect involves the theoretical calculation of permeabilities in ferromagnetic wave guides [23, 24]. They showed the medium was effectively circularly birefringent and the Faraday rotation was proportional to the

18

magnetization generated by the material. Thus a Faraday effect can occur inside a magnetizable medium that is electrically neutral. More recent work [1, 25] suggests such an effect could have implications on the polarization of the cosmic microwave background and as a possible measurement tool to directly detect dark matter in a terrestrial experiment if it has a magnetic moment. These works, along with Ref.[17, 26, 27], derive an expression for the rotation angle due to the magnetization of magnetic moments of electrically neutral particles, the following derivation summarizes this result from the references. Consider a magnetizable medium that sits in a static magnetic field, an electromagnetic wave propagating along the direction of this field will induce a magnetization that changes according to the Larmor precession formula

$$\frac{d\vec{M}_{total}}{dt} = \frac{g\mu}{\hbar}\vec{M}_{total} \times \vec{B}_{total}.$$ (2.27)

The total quantities $\vec{M}_{total} = \vec{M} + \vec{M}_0, \vec{B}_{total} = \vec{B} + \vec{B}_0$ are the from the external magnetic field ($\vec{B}_0$) and the magnetic field of the light ($\vec{B}$). $g\mu/\hbar$ is the gyromagnetic ratio of the particles in the medium and the magnetic moment is $\vec{\mu} = g\vec{S}\mu$ where $\vec{S}$ is the spin of the particles. Eq.(2.27) is valid for rest frame, it can be extended to the lab frame through the Bargmann-Michel-Talegdi (BMT) equation because the magnetization is given by the expectation value of the spin for single particle multiplied by the number density. The BMT equation is

$$\frac{dS^\alpha}{d\tau} = \frac{ge}{2mc}[F^{\alpha\beta}S_\beta + \frac{1}{c^2}U^\alpha(S_\lambda F^{\lambda\mu}U_\mu)] - \frac{1}{c^2}U^\alpha(S_\lambda\frac{dU^\lambda}{d\tau}),$$ (2.28)

with $S = (S^0, \vec{S})$ the spin 4 vector, $U = c\gamma(1, \vec{\beta})$ the 4-velocity of the particle, and $F^{\alpha\beta}$ the field strength tensor. The equation describes the motion of a particle's spin inside external electromagnetic fields. The final term in Eq.(2.28) is the Thomas precession term and for neutral particles is not needed. Requiring $dU^\lambda/d\tau = 0$, the time evolution of the magnetization in the lab frame is [1]

$$\gamma\frac{d\vec{M}_{total}}{dt} = \frac{g\mu}{\hbar}\left\{\left[(\vec{M} + \vec{M}_0) \times \left((\vec{B} + \vec{B}_0) - \vec{\beta} \times \frac{(\vec{E} + \vec{E}_0)}{c}\right)\right]\right.$$
$$\left. + \left[\gamma^2\vec{\beta}\left(\vec{\beta} \times (\vec{M} + \vec{M}_0)\right) \cdot (\vec{B} + \vec{B}_0) - \vec{\beta} \times \frac{(\vec{E} + \vec{E}_0)}{c}\right]\right\}.$$ (2.29)

Several approximations can be made to simplify, there is no external electric field so $\vec{E}_0 = 0$, assume the external magnetic field is along the $\hat{z}$ axis and choose $\vec{\beta}$ to be in the $\pm\hat{z}$ direction as well, and assume the $\vec{M}_0$ is directed along the $\hat{z}$ axis too, finally we only want to work with the leading order of small quantities $(\vec{M}, \vec{E}, \vec{B})$. This yields

$$\gamma \frac{d\vec{M}}{dt} = \frac{g\mu}{\hbar}\left(\vec{M} \times \vec{B}_0 + \vec{M}_0 \times (\vec{B} - \vec{\beta} \times \frac{\vec{E}}{c})\right). \tag{2.30}$$

Writing the fields of right and left circularly polarized light as

$$\vec{B}_\pm = B_\pm e^{ik_\pm z - i\omega t}(\hat{x} \pm i\hat{y})$$
$$\vec{E}_\pm = -cB_\pm e^{ik_\pm z - i\omega t}(\hat{y} \pm i\hat{x}) \tag{2.31}$$
$$\vec{M}_\pm = M_\pm(\hat{x} \pm i\hat{y}).$$

Inserting Eq.(2.31) into Eq.(2.30)

$$\gamma \frac{dM_\pm}{dt} = \left(\frac{g\mu M_0}{\hbar} M_\pm e^{ik_\pm z - i\omega t}\right) \mp \left(\frac{g\mu B_0}{\hbar} B_\pm (1+\beta) e^{ik_\pm z - i\omega t}\right). \tag{2.32}$$

In the steady state solution $\gamma \frac{dM_\pm}{dt} = 0$ and defining the frequencies $\omega_M = \frac{g\mu M_0}{\hbar}$ and $\omega_B = \frac{g\mu B_0}{\hbar}$ the solution is

$$M_\pm = \pm \frac{\omega_M (1+\beta)}{\gamma\omega \pm \omega_B} B_\pm = \chi_\pm B_\pm. \tag{2.33}$$

Where χ is the magnetic susceptibility which is related to the index of refraction for right and left circularly polarized light by $n_\pm = \sqrt{1 + \chi_\pm}$. Going back to Eq.(2.6) the angle of rotation due to this induced circular birefringence is

$$\theta = \frac{\omega_M d}{2\gamma c}\left(1 + \mathcal{O}\left(\frac{\omega_B^2}{\gamma^2\omega^2}\right)\right). \tag{2.34}$$

Using the reasonable assumption that the frequency of the electromagnetic wave is much larger than the frequency terms ω_B, ω_M. Finally, assuming the net magnetization is due to a collection of spin-1/2 particles it can be written as $M_0 = \mu N P$, where N is the number density and P is the polarization of the spins, and working in the non-relativistic limit the final rotation angle is given by

$$\theta = \frac{\mu_0 \mu^2}{\hbar c} N P d. \tag{2.35}$$

Thus, an electromagnetic wave passing through a magnetizable medium inside a static magnetic field will experience circular birefringence due to the magnetization of the medium. Physically, the magnetic field of the light tilts the spins of the medium away from magnetization axis where they will emit radiation that interferes with the light causing the birefringence. This is a Faraday effect that arises from purely magnetic interactions as opposed to Faraday effects from electric interactions. One noticeable difference that separates it is the lack of frequency dependence. The Verdet constant has a $1/\omega$ dependence on the electromagnetic wave leading to rotation angles that scale with the frequency. This magnetic Faraday effect should have the same value for all frequencies of light. It is also separate from nuclear spin optical rotation which comes from the hyperfine interaction of the nuclear spin with an electron and is related to electric polarizability tensor. This effect presents a unique opportunity to probe systems with similar conditions to conditions of the derivation. To provide an additional confirmation of the formula for the rotation angle a derivation of this effect using relativistic quantum mechanics can also be calculated. The effect is essentially forward Compton scattering of a photon from a spin $1/2$ particle. Ref[28] relates the index of refraction of a medium to the coherent quantum mechanical forward scattering amplitude $f_{\lambda\lambda}(0)$ which itself is related to the amplitude $M_{\lambda\lambda}(k, p \to k, p)$ [29] where k, p are the momentum vectors of the photon and scatterer [30].

$$n(\omega) = 1 + \frac{2\pi N}{\omega^2} f_{\lambda\lambda}(0) = 1 + \frac{\pi N}{4\omega^2 m} M_{\lambda\lambda}(k, p \to k, p). \qquad (2.36)$$

Several papers have calculated and used the amplitude for forward Compton scattering of low energy photons from a spin-$1/2$ particle [31–33]

$$M_{\lambda\lambda}(k, p \to k, p) = f_1(0)(\vec{\epsilon}'^* \cdot \vec{\epsilon}) + f_2(0)i\vec{S} \cdot (\vec{\epsilon}'^* \times \vec{\epsilon}), \qquad (2.37)$$

$\vec{\epsilon}, \vec{\epsilon}'$ are the initial and final polarization state of the photon, $\vec{S}$ the scatterer spin, and the functions $f_1(0) = -2Z^2 e^2$ and $f_2(0) = -2m\kappa^2\omega$ with $\kappa = \left(\frac{\mu}{S} - \frac{Ze}{2m}\right)$ the anomalous magnetic moment of the scatterer [33]. To derive an expression for the Faraday rotation the initial polarization states for the photon are set to be right and

left circularly polarized and the final states are rotated by a small angle θ

$$\epsilon_\pm = \frac{1}{\sqrt{2}} \begin{pmatrix} 1 \\ \pm i \\ 0 \end{pmatrix} \qquad \epsilon'_\pm = \frac{1}{\sqrt{2}} \begin{pmatrix} 1 \mp i\theta \\ \theta \pm i \\ 0 \end{pmatrix}. \tag{2.38}$$

The expressions for the polarization state become $\vec{\epsilon}'^* \cdot \vec{\epsilon} = (1 \pm i\theta)$ and $\vec{\epsilon}'^* \times \vec{\epsilon} = (-\theta \pm i)\hat{z}$. Plugging these into Eq.(2.37) and taking the real part

$$\begin{aligned} M_{\lambda\lambda}(k, p \to k, p) &= -2Z^2 e^2 (1 \pm i\theta) + -2m\kappa^2\omega i(-\theta \pm i)\vec{S} \cdot \hat{z} \\ Re[M_{\lambda\lambda}(k, p \to k, p)] &= -2Z^2 e^2 \pm 2m\kappa^2\omega\vec{S} \cdot \hat{z}. \end{aligned} \tag{2.39}$$

Combining Eq.(2.39) and Eq.(2.36) with the familiar equation Eq.(2.6) gives the angle of rotation

$$\theta = \frac{\omega d}{2c} \frac{N\kappa^2}{2\omega} \sigma_z. \tag{2.40}$$

Adding back factors to take care of dimensions yields

$$\theta = \frac{\mu_0}{4\hbar c} \kappa^2 N P d. \tag{2.41}$$

For an electrically neutral spin-1/2 particle the quantum derivation of the rotation angle yields the exact same result as the classical.

2.3.1 System to measure gyromagnetic Faraday rotation

The gyromagnetic Faraday effect offers a chance to measure a purely magnetic Faraday effect. The effect has possible implications for the polarization of the cosmic microwave background [25], and for an experiment to directly detect dark matter, if it has a magnetic moment, through a cavity enhanced Faraday rotation measurement with a large magnetic field [1]. Similar to vacuum birefringence measurements as shown in Ref.[34]. It would be ideal, however, to test the effect on a simpler system first. The derived rotation angle depends on the magnetic moment of the particles, their polarization, their density, and the path length of the probe light

Table 2.1: Parameters for rotation angle calculation

Parameter	Value
c	$3 \times 10^8 \frac{m}{s}$
$\hbar$	$1.055 \times 10^{-34} Js$
μ_0	$4\pi \times 10^{-7} \frac{N}{A}$
μ_{He}	$-1.071 \times 10^{-26} \frac{J}{T}$
N	$2.699 \times 10^{26} \frac{1}{m^3}$
P	1
d	$0.4m$

used. Therefore, a target that meets all these criteria would be optimal. Hyper-polarized noble gas targets appear to be ideal for this purpose. High density targets, which are transparent and have resonance transitions far away from common wavelengths, can be nuclear spin polarized to very high percentages inside glass cells of moderate length. The two main noble gases that can be polarized in a such a manner are ^{3}He and ^{129}Xe,^{131}Xe. Of the two ^{3}He is the perfect choice to try to measure the gyromagnetic Faraday effect, its magnetic moment is roughly three times as large as the magnetic moment of Xe and it has a much simpler electronic structure. Using a common density and length for a polarized ^{3}He target the rotation angle can be estimated with Eq.(2.35)

The result, using the parameters in Table.2.1, is 491 nano-radians for a target which is 100% polarized. This rotation is very small and near the limit of current technology to measure rotation angles of linearly polarized light. The rotation angle should be the same for all frequencies of probe light, offering a method to isolate it from other background Faraday rotations. The main topic of this work is concerned with the measurement of the gyromagnetic Faraday effect from polarized ^{3}He. The following chapter will delve into the specifics of the polarized target.

Chapter 3 Measuring Faraday Rotation

The measurement of light polarization is referred to as polarimetry. There are several techniques for determining the polarization state of light, for measuring the optical rotation of linearly polarized light the most common techniques involve combinations of polarizers and wave plates to detect changes in intensity. This chapter will describe the methods used in this work to measure Faraday rotation. The majority of the topic will be on a triple modulation technique for precision measurements of Faraday rotation angles and various calibrations with the system.

3.1 Balanced polarimeter

When Faraday discovered his effect he used two polarizers to measure a change in intensity of his light source. Two linear polarizers with their transmission axis perpendicular to each extinguished the light source, a sample in between them induced a small rotation of the plane of polarization so that it was no longer perpendicular to the last polarizer and some intensity of light was able to get through. Modern techniques are similar, but to measure rotation angles that are small additional elements have to be incorporated. A balanced polarimeter is shown in Fig.(3.1). Light from a source, lasers are used almost exclusively, passes through a linear polarizer and then a half-wave plate that rotates the polarization 45° with respect to the final element a polarizing beam splitter (PBS). The polarizing beam splitter divides the beam into the two orthogonal linear components, s and p polarization, and reflects one while transmitting the other. If the incoming light is polarized at 45° with respect to the PBS the measured intensity of the outgoing beams will be the same.

$$I_1 = I_0 \sin^2 \frac{\pi}{4} = I_2 = I_0 \cos^2 \frac{\pi}{4} = \frac{I_0}{2}. \tag{3.1}$$

I_0 is the initial intensity of the light and I_1, I_2 are the intensities coming out of the PBS. The polarimeter is then in the balanced condition, this is the initial state

24
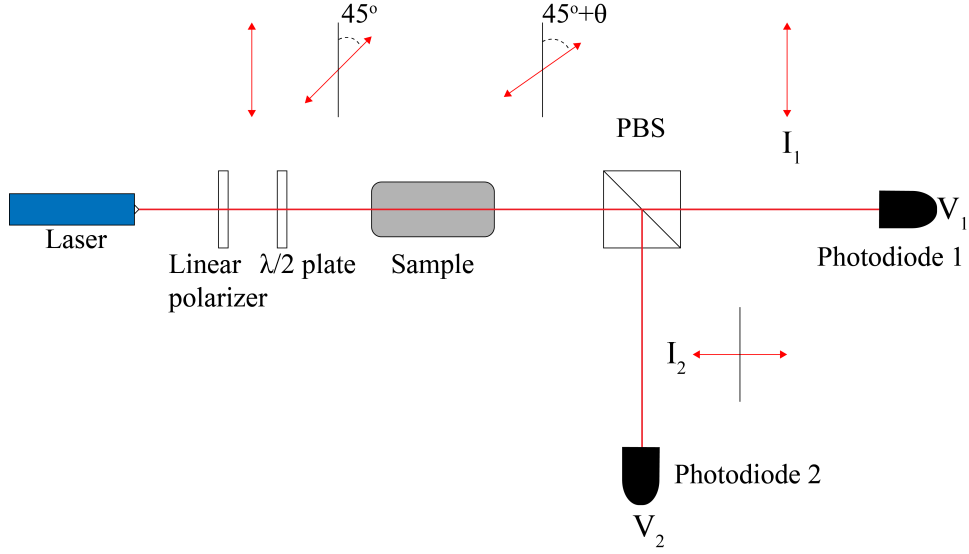
Figure 3.1: Schematic setup for a balanced polarimeter

before a sample is added. The introduction of a sample that rotates the polarization by some angle θ changes the intensity of these two beams.

$$
\begin{aligned}
I_1 &= I_0 \sin^2 \left(\frac{\pi}{4} - \theta\right) \approx I_0(1 + 2\theta)/2 \\
I_2 &= I_0 \cos^2 \left(\frac{\pi}{4} - \theta\right) \approx I_0(1 - 2\theta)/2.
\end{aligned}
\tag{3.2}
$$

For small angles, θ can then be given by

$$
\theta \approx \frac{I_1 - I_2}{2(I_1 + I_2)} \approx \frac{V_1 - V_2}{2(V_1 + V_2)}.
\tag{3.3}
$$

The intensities are measured with photodiodes, hence in a real experiment the signals will be voltages. With well matched photodiodes and low noise differential circuitry for the voltage signals, balanced polarimeters are capable of very small rotation measurements [13].

3.2 Faraday rotation with triple modulation

For this dissertation, the method used to measure Faraday rotations is similar to the crossed linear polarizers. However, the addition of three different modulations

allow for extracting extremely small rotations from a noisy environment and isolating them from large background rotations [35, 36]. A schematic of the setup is shown in Fig.(3.2). Light from the laser first passes through a Glan-Thompson prism, which is a linear polarizer with a wide angle of incidence with a high extinction ratio. The prism is in a precision rotation mount to allow fine control of the polarizing axis, it's axis is orientated such that the outgoing light is s polarized. It then passes through the sample material being investigated which sits in the center of a pair of Helmholtz coils used to generate the magnetic field for the Faraday effect. Following the sample, the light goes through a photoelastic modulator (PEM) and then a second Glan-Thompson prism, also in a precision rotation mount, oriented at a 45° angle with respect to the PEM. The combination of the PEM and second GTP provide an intensity which is proportional to the rotation angle. The last component is the optical chopper and a HINDS DET-200 silicon photo-detector which has a high enough frequency response for the PEM frequency.
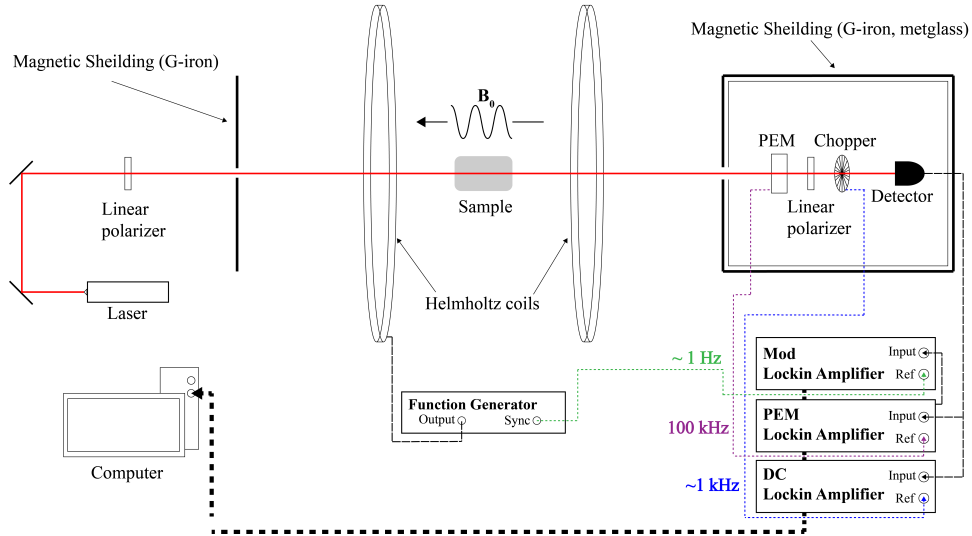
Figure 3.2: Schematic diagram of the triple modulation setup. Magnetic shielding prevents the field from affecting the polarizing optics or the analyzing optics. The analyzing optical elements consist of the PEM, analyzer(final linear polarizer), optical chopper, and the photo-detector.

As the name suggest there are three modulations occurring during a measure-

26

ment. One is the optical chopper which periodically blocks the beam with a duty cycle of 50%. It is usually run at a frequency of 1-3 kHz. The second is the current supply for the Helmholtz coils via function generator. It modulates the magnetic field sinusoidally with a low frequency of about 1 Hz. The low frequency is chosen due to the fact that a higher frequency distorts the magnetic field. Both the polarizing optical elements and the analyzing optical elements are protected by layers of magnetic shielding (G-iron, metglass) to prevent the errors associated with fringe field effects. The final modulation is the PEM which is a birefringent fused silica crystal oscillating at 50 kHz to alter the polarization of the probe beam, the final light intensity in the detector is a function of the PEM frequency and its harmonics.

The photoelastic modulator is a fused silica crystal attached to a piezoelectric transducer that is used to oscillate the crystal in one direction. This stretching and contracting along one axis changes the index of refraction for polarization components perpendicular or parallel to the axis [37]. This dynamically shifts the polarization of the light through all of the polarization states at the frequency of the applied voltage Fig.(3.3). Thus the PEM provides a modulation of the polarization of the probe light. The high resonant frequencies these crystals need to be driven at to operate means that a lock-in amplifier can be used to detect the signal and significantly reduce noise from other sources. For this work, the optical head of the PEM has a resonant frequency of 50 kHz.

In order to calculate the effect the PEM has on a polarized beam and derive a useful expression for the light intensity in the detector the time dependent phase difference between the two components is written as

$$\delta_{PEM}(\lambda, t) = \frac{2\pi d}{\lambda} A(\lambda) \sin(\omega t), \tag{3.4}$$

d is the thickness of the optical path in the bar, λ the wavelength, A is the peak strain amplitude, and ω the modulation frequency of the voltage. For harmonic strain this can be reduced to

$$\delta_{PEM}(\lambda, t) = A \sin(\omega t) + \delta_0(\lambda), \tag{3.5}$$

δ_0 is a small correction due to the residual static strain of the PEM, it is typically very small and corrected for by the manufacturer. The Mueller matrix for a phase
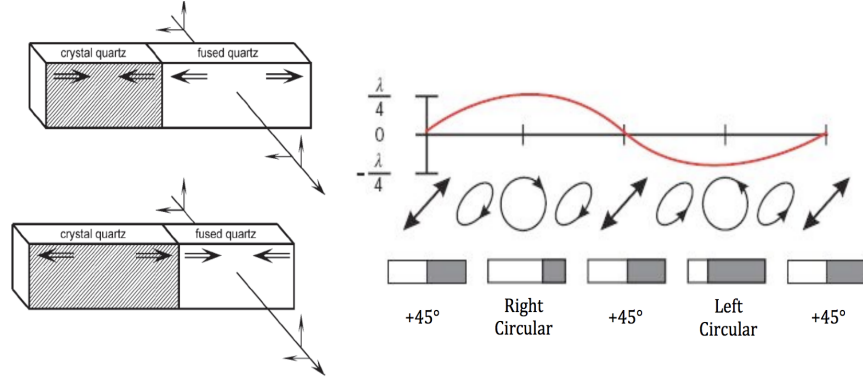
Figure 3.3: Diagram of the crystal in the PEM and the polarization state of the light after the initial polarizer and PEM. The light polarization oscillates from linear to elliptical to circular and back and the driving frequency of the transducer. [38]

retarder like a PEM contains terms such as $\cos(\delta_{PEM})$ and $\sin(\delta_{PEM})$ therefore we wish to expand these as

$$\cos(\delta_{PEM}) = \cos[A\sin(\omega t) + \delta_0] = \cos[A\sin\omega t]\cos\delta_0 - \sin[A\sin\omega t]\sin\delta_0$$
$$\sin(\delta_{PEM}) = \sin[A\sin(\omega t) + \delta_0] = \sin[A\sin\omega t]\cos\delta_0 + \cos[A\sin\omega t]\sin\delta_0,$$
(3.6)

With δ_0 taken to be very small these expressions can be reduced and then expanded with a Bessel function series where they are functions of the harmonics of the PEM resonant frequency

$$\cos[A\sin(\omega t)] = J_0(A) + 2\sum_{j=1}^{\infty} J_{2j}(A)\cos[2j\omega t]$$
$$\sin[A\sin(\omega t)] = 2\sum_{j=1}^{\infty} J_{2j-1}(A)\sin[(2j-1)\omega t],$$
(3.7)

$J_j(A)$ are Bessel functions of the first kind and the peak amplitude of the modulation, A, is set so that $J_0(A) = 0$, $J_1(A) = 0.519$ and $J_2(A) = 0.432$. This gets rid of the J_0 term and ensures that the J_1, J_2 terms dominate the expansion. The result is then

$$\cos(\delta_{PEM}) = 2J_2\cos 2\omega t + \textit{higher order terms...}$$
$$\sin(\delta_{PEM}) = 2J_1\sin \omega t + \textit{higher order terms....}$$
(3.8)

28

Finally, using Stokes vectors and Mueller matrices the intensity in the detector for a sample that induces a Faraday rotation is

$$S_{final} = M_{polarizer45^o} \cdot M_{PEM} \cdot M_{Sample} \cdot M_{polarizer90^o} \cdot S_{initial}, \quad (3.9)$$

$$
\begin{pmatrix} 1 & 0 & 1 & 0 \\ 0 & 0 & 0 & 0 \\ 1 & 0 & 1 & 0 \\ 0 & 0 & 0 & 0 \end{pmatrix} \cdot \begin{pmatrix} 1 & 0 & 0 & 0 \\ 0 & 1 & 0 & 0 \\ 0 & 0 & \cos(\delta_{PEM}) & -\sin(\delta_{PEM}) \\ 0 & 0 & -\sin(\delta_{PEM}) & \cos(\delta_{PEM}) \end{pmatrix} \cdot \begin{pmatrix} 1 & 0 & 0 & 0 \\ 0 & \cos 2\theta & -\sin 2\theta & 0 \\ 0 & -\sin 2\theta & \cos 2\theta & 0 \\ 0 & 0 & 0 & 1 \end{pmatrix}
$$

$$
\cdot \begin{pmatrix} 1 & -1 & 0 & 0 \\ -1 & 1 & 0 & 0 \\ 0 & 0 & 0 & 0 \\ 0 & 0 & 0 & 0 \end{pmatrix} \cdot \begin{pmatrix} I_0 \\ 0 \\ 0 \\ 0 \end{pmatrix} = \begin{pmatrix} \frac{I_0}{2}(1 + \cos \delta_{PEM} \sin 2\theta) \\ 0 \\ I_0 2(1 + \cos \delta_{PEM} \sin 2\theta) \\ 0 \end{pmatrix},
$$

$$(3.10)$$

$$I(t) = I_0[1 + 2J_2 \cos(2\omega t) \sin(2\theta) + higher\ order\ terms...]. \quad (3.11)$$

The intensity of light going into the photodiode is therefore a sum of terms which are functions of the harmonic frequencies of the PEM resonant frequency at 50 kHz. The Faraday rotation angle is proportional to the even terms (J_2, J_4...) of the series. If the sample generated an elliptical polarization, or an ellipticity, the odd terms in the series (J_1, J_3...) would be proportional to it. By using lock-in amplifier techniques the signal at the second harmonic of 100 kHz can be isolated and then taking the ratio of the AC term to a DC term measuring I_0 the rotation angle can be extracted.

For the triple modulation technique, the photo-detector is connected to three lock-in amplifiers as shown in Fig.(3.2), each referenced to one of the three modulation frequencies. The DC lock-in amplifier is referenced to the optical chopper and provides a measure of the overall intensity of the beam. A lock-in amplifier measures the V_{rms} value of the input signal so the lock-in amplifier voltage must be multiplied by a factor of $\sqrt{2}$. Additionally, because the chopper creates a square wave from zero to full intensity more pre-factors must be added to account for the fact that the

lock-in amplifier essentially performs a Fourier transform on a square wave function [35] and the peak to peak value is needed. The real DC voltage is

$$V_{DC} = \sqrt{2} \cdot 2 \cdot \frac{\pi}{4} \cdot V_{DC}^{LI}. \tag{3.12}$$

The next lock-in amplifier is the PEM, it is referenced to the second harmonic of the PEM frequency at 100 kHz. The voltage is proportional to the rotation angle, however, because the the magnetic field is driven with a sinusoidal current the rotation angle has its own time dependence. This modulation is still encompassed in the PEM signal, meaning the demodulated voltage the PEM lock-in amplifier displays will have a component oscillating at the frequency of the magnetic field modulation. As long as this frequency is below the frequency of the PEM the signal will pass through without further processing. Hence, an analog output of the PEM lock-in amplifier that is proportional to the voltage it detects is used as an input for the third Mod lock-in amplifier. The Mod lock-in amplifier is referenced to the frequency of the magnetic field modulation. The rear output of the PEM lock-in amplifier is scaled as a percentage of 10 V based upon the ratio of the front panel voltage to the sensitivity setting. The final voltage can be calculated by

$$V_{Mod} = \frac{2 \cdot \sqrt{2} \cdot \sqrt{2}}{10V/sens} \cdot V_{Mod}^{LI}. \tag{3.13}$$

Where $sens$ is the voltage sensitivity setting of the PEM lock-in amplifier. Hence, the Mod lock-in amplifier is connected to the detector only through the PEM lock-in amplifier. The lock-in amplifiers are connected via GPIB cable to a computer which collects the voltage data from each. Combining the expressions for the voltages and Eq.(3.11) the Faraday rotation angle as measured with the triple modulation setup is given by

$$
\begin{aligned}
2J_2 \sin{(2\theta)} &= \frac{4\sqrt{2}sens}{10\pi} \frac{V_{Mod}}{V_{DC}} \\
\theta &= \frac{1}{2} \arcsin{\left[\frac{2\sqrt{2}sens}{10\pi J_2} \frac{V_{Mod}}{V_{DC}} \right]} \\
\theta &= \frac{\sqrt{2}sens}{10\pi J_2} \frac{V_{Mod}}{V_{DC}} = V dB_0.
\end{aligned} \tag{3.14}
$$

For small angles less than 100 mrad the small angle approximation can be used and the arcsin can be ignored. The percent difference between the two formulas is less than 0.2%. With this setup the angle of rotation from the sample due to the Faraday effect is a ratio of two of the lock-in amplifier voltages and a pre-factor.

3.2.1 Calibration of the triple modulation setup

The first calibration that is important for the setup is the alignment of the linear polarizers and the PEM axis. The goal is to ensure the rotation measurement is as close to zero as possible with no sample and the correct alignment of the optics. Both polarizers are in precision rotation stages that can be used to accomplish this. The setup relies on s polarized light as the initial polarization, so a beam splitting cube is used and the polarizer is rotated until it is solely s polarized. Then, with no magnetic field or sample, the second linear polarizer (analyzer) is rotated until the PEM lock-in amplifier reads a null signal. This corresponds to the transmission axis of the analyzer being at 0° or 90° with respect to the PEM axis. The proper alignment for the analyzer is then at a 45° offset from this setting. This can be checked by rotating the anaylzer axis by 90° observing whether the DC signal remains the same.

The next calibration is to insert a sample that will give a well known rotation and confirm the setup measures it as expected. Flint glasses usually have large Verdet constants that can generate sizable rotations at modest magnetic fields. The large rotation angle makes the measurement easy and keeps possible errors to a minimum. A sample 1.27 cm cube of SF57 glass was used for this calibration. SF57 flint glass has a known Verdet constant of 2.01×10^{-5} rad/(G cm) at 300 K for 632.8 nm wavelength of probe light [39]. The rotation for the SF57 sample is shown in Fig.(3.4), the extracted Verdet constant is V = $(1.999 \pm 0.003) \times 10^{-5}$ rad/(G cm) which agrees within errors.

Some common lock-in amplifier settings used in Faraday rotation measurements are listed in the appendices.

An important point to note is that the magnetic field extends much further than the sample of SF57 used and while all components in the optics train are well shielded

31
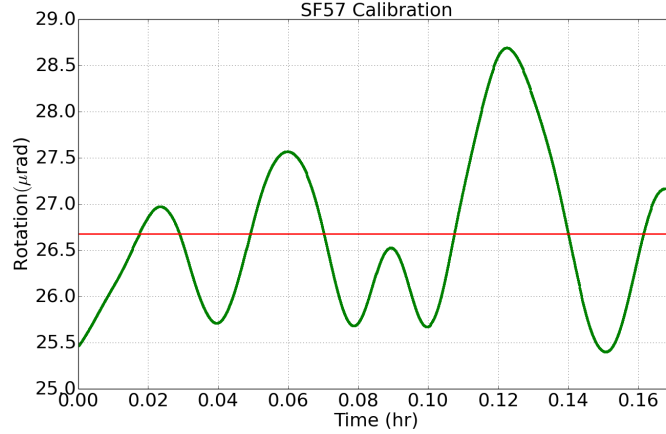
Figure 3.4: Rotation angle measurement of SF57 flint glass for the triple modulation setup calibration. The magnetic field amplitude is 1.05 G.

with G-iron and metglass there is still a systematic offset due to the Faraday rotation of air. The Verdet constant for air is not agreed upon as it is very small and difficult to measure. Usually a large magnetic field or cavity enhancement is needed to measure the Faraday rotations from air [40]. Since the triple modulation setup is used for precision measurement of small rotation angles the contribution from air becomes a factor that needs to be accounted for. Recent experiments quote values around 1.4×10^{-9} rad/(G cm) [41]. Earlier work with the triple modulation setup yielded a Verdet constant of 1.5×10^{-9} rad/(G cm) [35], this value remains consistent for this work and is the value used to make corrections due to the contribution from air. Furthermore, the wavelengths vs Verdet constant curve can be expanded with new wavelengths Fig.(3.5).

3.2.2 Verdet constants for aluminosilicate glass

The experimental setup is eventually used with a polarized ^{3}He target described in the following chapter, the helium is contained inside a glass cell that is made of special, dense aluminosilicate glass whose Verdet constants are not very well known. It is important to understand the contribution to the Faraday rotation from these glasses to discuss possible systematic errors associated with the measurements on

32
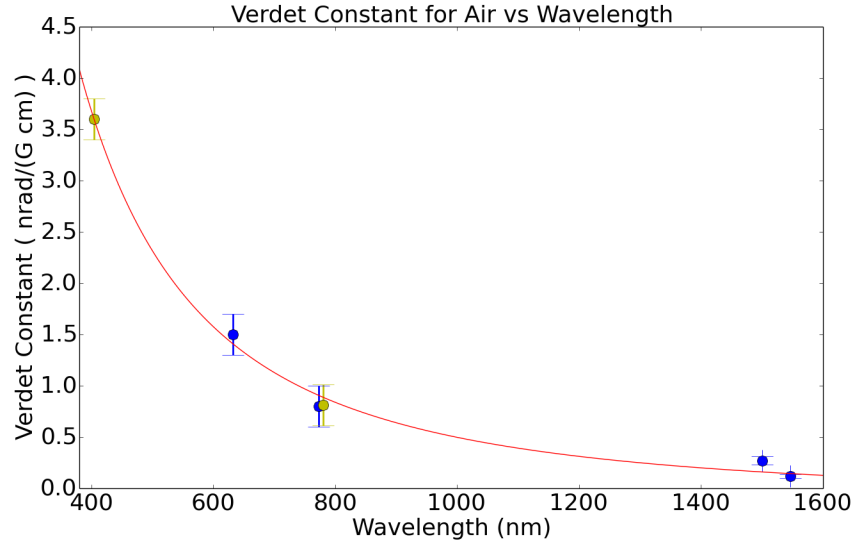
Figure 3.5: Verdet constant for air as a function of wavelength to show the $1/\lambda^2$ dependence. New data points shown in green.

the polarized ^{3}He target, therefore the Verdet constants were measured precisely for the wavelengths of interest. The two glasses important for these measurements are GE-180 and Corning 1723, in order to get accurate Verdet constant measurements the thickness of the samples needs to measured. For GE-180, a sample was provided by NIST and its thickness was measured using interferometry techniques and found to be (4.003 ± 0.002) mm. For Corning 1723, samples were acquired from the manufacturer and measured with calipers, the glass section used for the Verdet constant measurement had a thickness of (3.18 ± 0.02) mm. The results for the various wavelengths are summarized in Table.(3.1)

Both glasses are of similar composition so the Verdet constants do not differ by large amounts. With the calibrations from these samples, the Faraday effect may then be used to measure the unknown thickness of the glass walls of the helium cells. Such measurements could be useful in determining the internal volume of the cell which is difficult to measure once it has been sealed.

Table 3.1: Measured Verdet constants for the aluminosilicate glasses

Wavelength (nm)	V_{GE-180} (μrad/(G cm))	$V_{Corning1723}$ (μrad/(G cm))
405	9.20 ± 0.1	7.70 ± 0.06
632.8	3.80 ± 0.02	3.15 ± 0.02
780	2.5 ± 0.1	2.1 ± 0.1

3.2.3 Small angle rotation measurements

The expected rotation angle from the magnetic Faraday effect for ^{3}He is predicted to be on the order of nanoradians (10^{-9} rad). Most modern experiments that measure small optical rotations as a detection device report angular sensitivities in the range of 10^{-6}rad/$\sqrt{\text{Hz}}$ to 10^{-10}rad/$\sqrt{\text{Hz}}$ ([4, 10, 11, 13, 34, 40–43]). While comparisons can be difficult due to factors such as increased path length through cavity enhancement, non-linear resonant Faraday rotation, high magnetic fields, and varying definitions of the noise limit, it is safe to say the scale of the expected rotation from ^{3}He is near the current limit of angular sensitivity. The experiments with this kind of sensitivity tend to use some form of the balanced polarimeter, therefore it is necessary to prove that the triple modulation setup is capable of measuring such small angles of linear polarization in pursuance of the magnetic Faraday effect.

In addition to the magnetic shielding around the polarizer and analyzer optics both sit on tables with vibration damping to reduce errors from micro-movements. The large distance between the laser and the detector (~ 5 m) required for keeping everything out of the magnetic field means such small movements become important. Careful calibration of the optical components in the setup is crucial, while the angle for the initial polarizer and the angle between the analyzer and PEM can both be tuned well enough with the method described previously, the incident angle of the probe laser and the PEM surface becomes just as relevant for this scale measurement. Where the beam passes through the optical head of the PEM, as well as the horizontal and vertical angles the beam makes with the surface normal are all adjusted to minimize the noise. With the setup adjusted to the right conditions a sample with a

well known Verdet constant can be placed in the magnetic field and the amplitude of the field can be lowered to produce smaller and smaller rotations. Ideally, something with a small Verdet constant, like air, would be used but in the laboratory conditions air is too volatile over long periods for such measurements. Hence, samples of GE-180 glass and SF57 glass are separately tested and the results are shown in Fig.(3.6).
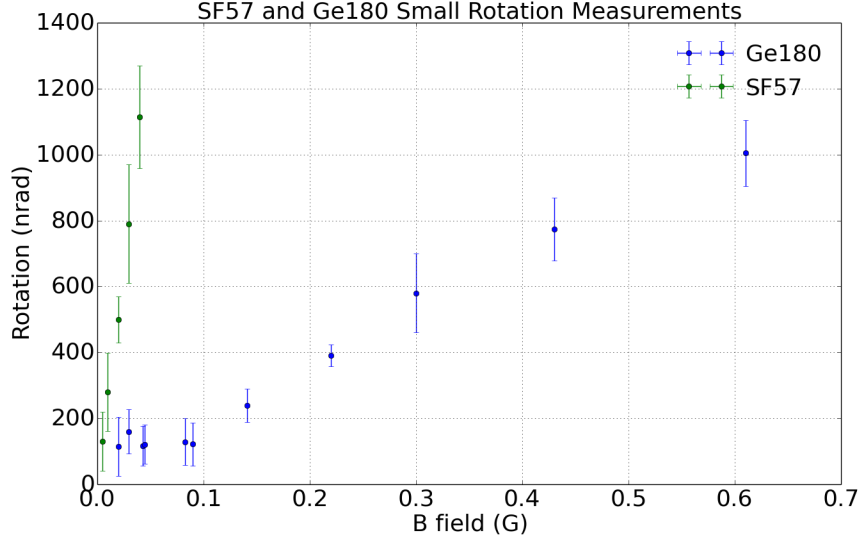
Figure 3.6: Test with GE-180 and SF57 glass samples in small magnetic fields to determine the smallest rotations that the triple modulation system can resolve. The level of ∼100 nrad is the limit for this test.

As the field amplitude was lowered the rotation angle was also lowered. The rotations from SF57 scale faster with larger fields because the Verdet constant is much larger than GE-180's, so in order to reach the same scale much smaller magnetic fields had to be used. The smallest field amplitude that could be reliably produced was 5 mG, this is the limit that the gaussmeter hall probe could resolve. Though, as can be seen in the figure, smaller fields would not be useful as the limit for measured rotations is reached below 100 mG. At this range, the triple modulation system measures around 100 nrad even if the expected rotation from the sample is lower. At the lowest field settings for GE-180 the expected rotations are 30 nrad and 46 nrad while the measured values are 115±90 nrad and 160±67 nrad, respectively. While for

the lowest field setting for SF57 the expected rotation is 127 nrad and the measured is 130±90 nrad. At this level the error of the rotation angle is about the same size as the mean value measured resulting in an effective "noise floor" below which angles cannot be resolved. From the graph the limit of the system is ∼100 nrad. Although in practice, even though the experimental setup is stabilized, significant fluctuations in lab conditions such as temperature, vibrations, or shifting electrical grounds can lead to small fluctuations in this number. The predicted signal size from the magnetic Faraday effect of ^{3}He, given common parameters for ^{3}He targets that are available to the lab, is 412 nrad. Meaning the triple modulation system has enough sensitivity to detect the effect.

There are additional settings that need to be accounted for, settings that are important for the experiment with helium and in general to determine the versatility of the setup. The data in Fig.(3.6) is taken with sinusoidal modulation of the magnetic field at frequencies between 0.770 Hz and 1.03 Hz. In principle, different field modulation types (e.g square wave, triangle wave...) or different frequencies could have different errors associated with them. Because the Helmholtz coils that generate the magnetic field do not work well at frequencies higher than 1 Hz only frequencies below that are considered. In that range $1/f$ noise can become a significant contributor to the errors. Further data was taken with the same glass samples as before with square wave field modulations at frequencies down to 2.5 mHz. When the modulation signal is a square wave similar to the DC lock-in amplifier signal an additional factor of $\pi/4$ appears in Eq.(3.14) and needs to be accounted for. With the proper formula, the sine wave modulation and square wave modulation yield the exact same rotation for the same frequency as shown in Fig.(3.7)

The same is true for larger magnetic fields used to create larger rotations. There do not appear to be appreciable errors from a square wave modulated signal. To compare the different frequencies, a large rotation angle was measured for the GE-180 sample and the field modulation frequency was lowered down to the mHz range. Every frequency measured yielded similar results for the measured rotation. Furthermore, for smaller field amplitudes and rotations the different frequencies approached the same low value. Another check can be performed on the setup to confirm these

36
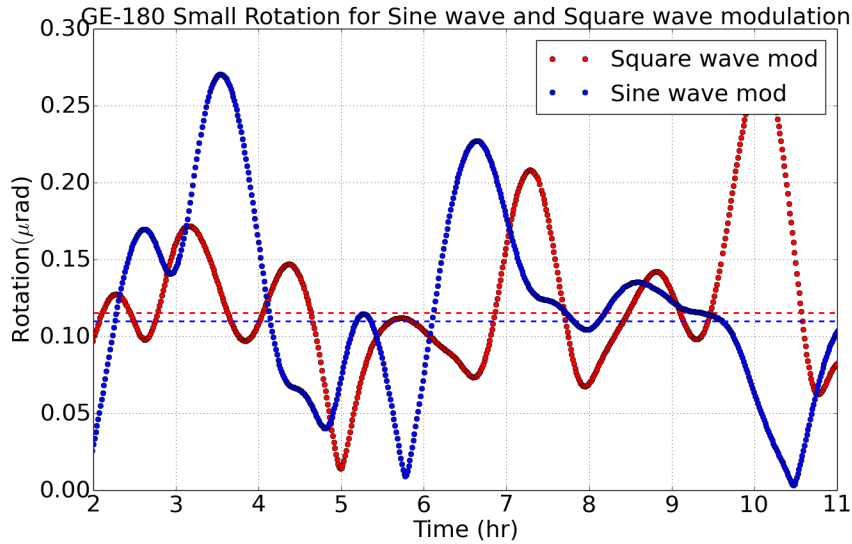
Figure 3.7: Measured Faraday rotation for GE-180 glass sample for a square wave magnetic field modulation and a sine wave magnetic field modulation of the same frequency. The values are the same within errors.

results by taking the output voltage of the PEM lock-in amplifier and performing a Fourier transform (FT) on it as opposed to reading the signal from the Mod lock-in amplifier. The FFT should display a peak at the modulation frequency. An example plot for several low frequencies is shown in Fig.(3.8). The plot contains data for three different measurements of small rotation, square wave modulation at frequencies of 2.5, 4, and 11 mHz. The peaks give the correct rotation amplitude for all three data runs and as an additional confirmation the higher harmonics for a square wave are in the correct locations at $3f$ and $5f$.

In combination with the other calibration measurements this shows that the triple modulation system is able to measure nano-radian scale rotation angles. The setup is capable of making these measurements even at very low frequencies and with different modulation forms.
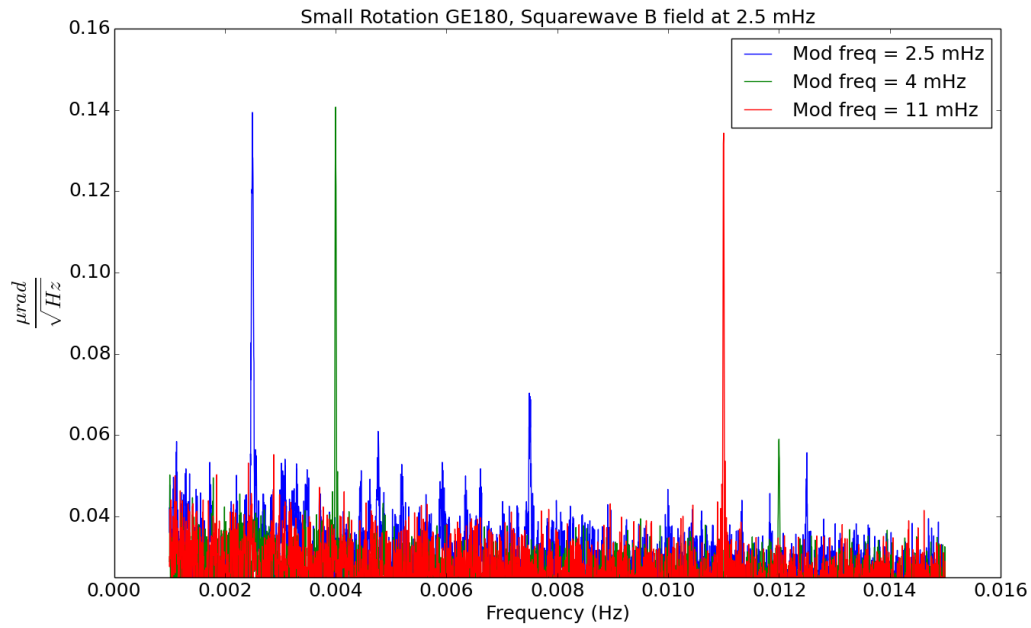
Figure 3.8: Lomb-Scargle periodogram of the PEM lock-in amplifier output for the GE180 sample inside square wave modulated fields of the same amplitude but different frequencies. The rotation amplitude is roughly the same for each measurement. The higher harmonics for a square wave occur at the correct frequencies showing that the modulation works.

Chapter 4 The Polarized ^{3}He Target

Helium gas that is nuclear spin polarized to a high degree, often called "hyper"-polarized gas, has extensive scientific applications. Due to the fact that the ^{3}He nucleus has two protons and one neutron, and in the ground state the spin of the two protons cancel most of the time ($\sim 90\%$), it provides a reasonable approximation to a polarized neutron [44]. This fact is why it is used in many nuclear and particle physics experiments as a target for charged particle and photon beams [45–47]. ^{3}He provides an excellent neutron spin filter due to the large spin dependence of the cross section for absorption of a neutron by the ^{3}He nucleus. This allows for highly polarized neutron beams [48, 49]. The chemical inertness of He, as well as the lack of an electric quadrupole moment, lead to long relaxation times inside the human body. Combined with with a large magnetic moment this allows for inhaled, polarized ^{3}He gas to yield very high resolution images lungs through MRI [50, 51]. As for the subject of this thesis, polarized ^{3}He provides a simple and extremely stable system useful for precision measurements. There are several ways to polarize the ^{3}He nucleus, the most inefficient method is to brute force the polarization by applying a large magnetic field with low temperatures to alter Boltzmann distributions. The magnitude of field needed to achieve a high polarization (~ 100T at 4 K), even just a few percent, makes the idea infeasible. Another method is to directly pump the $1s^2 \longrightarrow 1s2p$ transition. However, small hyperfine splitting in the state as well as a lack of readily available 58 nm radiation source make polarizing to a useful polarization impractical. The next two methods therefore rely on indirect optical pumping methods and spin exchange. Metastability-Exchange Optical Pumping (MEOP) [52, 53] involves exciting the ^{3}He from the ground state to the 2^3S_1 metastable state via RF discharge. The excited atoms are then optically pumped to the 2^3P state with 1083 nm light. Due to efficient hyperfine coupling in this state the nucleus becomes polarized in addition, spin exchange collisions then transfer this nuclear polarization to atoms in the ground state. The final method is Spin Exchange Optical Pumping

(SEOP). In this method the helium gas will be contained inside a glass cell with a small amount of N_2 and alkali metal vapor. The valence electron in alkali atoms is polarized by optical pumping with laser light then this electronic polarization is transferred by spin exchange collision to the ^{3}He nucleus. This is the method used to produce nuclear spin polarized ^{3}He gas in this experiment.

In this chapter the polarized ^{3}He target used in the magnetic Faraday rotation experiment will be described. The basic principles of using Spin Exchange Optical Pumping (SEOP) to polarize the helium atoms, the experimental setup of the target system, the description of the two helium cells used, how to measure the helium polarization, and some polarization analysis will all be presented.

4.1   Spin Exchange Optical Pumping

The precursors to the development of Spin Exchange Optical Pumping were early work in optical pumping, which involves selectively altering the populations of Zeeman sublevels of an atom using polarized light [54, 55] and spin exchange collisions, which involve transfer of electronic spin via a hyperfine Fermi contact interaction [56, 57]. These lead to some intermediate work [58, 59] in polarizing the spins of nuclei but it was not until the work by Chupp *et al.* (1987) [60] polarizing small volumes of ^{3}He gas to large polarization ($\sim 40\%$) that SEOP really got started. Today a wide variety of cell designs for different applications and high power narrowband pumping lasers combined with hybrid spin exchange from multiple alkali species produce ^{3}He polarizations of near unity with lifetimes of hundreds of hours [61].

4.1.1   Basic Principle of ^{3}He Polarization

When ^{3}He atoms are placed inside an external magnetic field the nuclear spin of the atom will line up with the direction of the applied field. The spins can be aligned either parallel to the field or anti-parallel to the field where the number of spins in the parallel state is given by ($N^\uparrow$) and the anti-parallel state by ($N^\downarrow$). At relatively small magnetic fields and room temperature the distributions are roughly equal with

only a small number ($\sim 10^{-9}$) of spins found in the lower energy, parallel state. The polarization of ^{3}He is defined by the vector polarization

$$P = \frac{(N^\uparrow - N^\downarrow)}{(N^\uparrow + N^\downarrow)}. \tag{4.1}$$

4.1.2 Optical Pumping

The first step of SEOP is the optical pumping of the Rb atoms. The glass cell is illuminated with circularly polarized light at 795 nm corresponding to the electron $S_{1/2} \longrightarrow P_{1/2}$ D1 transition. For simplicity, ignoring the Rb nuclear spin, each state has Zeeman sublevels given by $m_j = \pm\frac{1}{2}$. Due to the conservation of energy and angular momentum only one of the Zeeman sublevels is excited depending which state (right/left, σ^+, σ^-) of circularly polarized light is used. Thus the Rb electrons will be polarized in one of the two states as shown in Fig.(4.1). Normally the excited Rb atoms would radiatively decay by emitting photons of the same wavelength as the transition. These photons, which would be radiated isotropically, would consequently scramble the electron polarization building up in the ground state because they do not have the same polarization and propogation of direction as the pumping light. In order to combat this a small amount of N$_2$ gas is added to cell, it has a large collisional cross section with Rb and de-excites the atoms non-radiatively. The natural lifetime of the excited Rb state is 27 ns [62] and the added nitrogen de-excites the atoms around 10 times faster. The collisions also mix the excited states (as well as the ground states) and insures the Rb atoms decay back to either ground state with equal probability.

Within a few milliseconds the Rb polarization reaches an equilibrium value. This value P_{Rb} is given by the ratio of the optical pumping rate R_{pump} and the spin relaxation rate Γ_{Rb}

$$P_{Rb} = \frac{R_{pump}}{R_{pump} + \Gamma_{Rb}}, \tag{4.2}$$

with the optical pumping rate defined as

$$R_{pump} = \int_0^\infty \Phi(\nu)\sigma(\nu)d\nu. \tag{4.3}$$

41
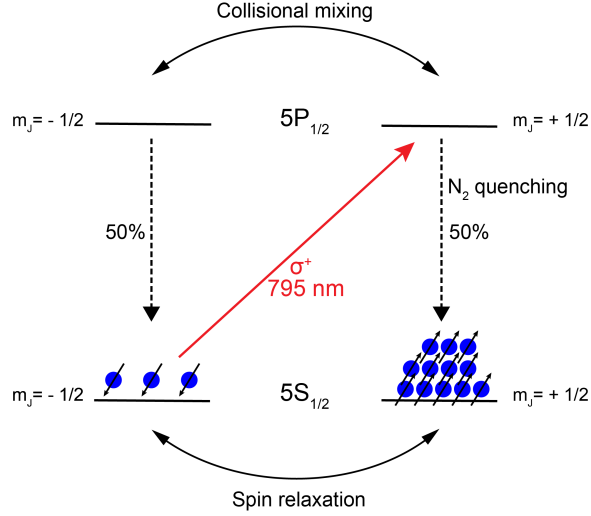
Figure 4.1: Simplified picture of optical pumping for the Rb $S_{1/2} \longrightarrow P_{1/2}$ transition at 795 nm

Where $\Phi(\nu)$ is the total photon flux and $\sigma(\nu)$ is the Rb photon absorption cross section. The main relaxation mechanism of the Rb spin is collisions with other Rb and ^{3}He atoms and N_2 molecules [63].

4.1.3 Spin Exchange

The second step of SEOP is the spin exchange collision. In traditional SEOP with only Rb, N_2, and ^{3}He the Rb transfers the electronic polarization to the helium nucleus through a weak hyperfine like Fermi contact interaction. In this way the polarization is gained by the ^{3}He nulcei through Rb-He collision and is lost through other ^{3}He relaxation mechanisms, mainly ^{3}He collisions with the cell wall, dipole interactions by He-He collisions, and passage through magnetic field gradients. The change in ^{3}He polarization is given by

$$\frac{dP_{He}}{dt} = \kappa_{Rb}[\text{Rb}](P_{Rb} - P_{He}) - \Gamma_{He}P_{He}, \tag{4.4}$$

κ_{Rb} is the Rb-He spin exchange rate coefficient, [Rb] is the Rb density, and Γ_{He} is the ^{3}He spin relaxation rate governed by the loss mechanisms mentioned. The steady state solution gives an equilibrium P_{He} of

$$P_{He} = P_{Rb} \frac{\kappa_{Rb}[\text{Rb}]}{\kappa_{Rb}[\text{Rb}] + \Gamma_{He}}, \tag{4.5}$$

Eq.(4.5) shows that if Γ_{He} is sufficiently small then it is possible for P_{He} to approach P_{Rb} though experimentally there are many factors that inhibit this. The spin exchange efficiency is the ratio of the rate at which ^{3}He gains angular momentum and the rate at which Rb loses angular momentum.

$$\eta_{Rb-He} = \frac{k_{Rb}[^3He]}{k_{Rb}[^3He] + \Gamma_{Rb}}. \tag{4.6}$$

This is the result for traditional SEOP, however improvements have been made by studying other alkali metal atoms. The Hamiltonian for the alkali metal- helium interaction is given by [64]

$$\begin{aligned}
\mathcal{H} =& \mathcal{A}_a I \cdot S + g_s \mu_B S \cdot B + \mu_A I \cdot B + \mu_{He} K \cdot B \\
& + \gamma N \cdot S + \mathcal{A}_b K \cdot S + \mathcal{B}_b K \cdot (3\hat{R}\hat{R} - 1) \cdot S.
\end{aligned} \tag{4.7}$$

Where I is the spin of the alkali-metal nucleus, S the spin of alkali-metal electron, and K the spin of the ^{3}He nucleus. N is the rotational angular momentum of the colliding alkali metal-^{3}He pair. B is the externallu applied magnetic field and $\hat{R}$ is the displacement vector between the alkali and helium atoms. The first term is the hyperfine coupling of the alkali atom, the second, third, and fourth are couplings to the external magnetic field. The γ term is the spin relaxation due to the alkali electron spin and the total rotational angular momentum of the pair. The size of γ depends on the alkali atom [65]. The $\mathcal{A}_b$ term is the Fermi contact hyperfine coupling term responsible for polarizing the ^{3}He nucleus. The ratio of the γ and $\mathcal{A}_b$ terms is important for the spin exchange efficiency of the alkali-helium pair. While $\mathcal{A}_b$ is nearly the same for all alkali atoms γ varies significantly. Several spin exchange and spin relaxation constants as well as spin efficincies are summarized in Table.(4.1). For Rb the spin exchange efficiency is around 3%, while for K it is at 24%, and Na goes as high as 90%. Thus, using another alkali species can greatly improve the spin exchange process for helium. Due to the difficulties in managing a Na-He glass cell and the need to keep using Rb because high power laser diodes for the D1 transition

are cheap and easy to use, hybrid cells using a mixture of Rb and K to polarize ^{3}He have become the norm for SEOP. In a Rb-K hybrid SEOP cell the Rb is still polarized using 795 nm at the D1 transition, the Rb then transfers this polarization to the K and ^{3}He, then the K transfer it's polarization much more efficiently to the ^{3}He nucleus as shown in Fig.(4.2). The resulting change in P_{He} is

$$\frac{dP_{He}}{dt} = \kappa_K[\text{K}](P_K - P_{He}) + \kappa_{Rb}[\text{Rb}](P_{Rb} - P_{He}) - \Gamma_{He}P_{He}. \tag{4.8}$$

Table 4.1: Relevant parameters for alkali metals for hybrid spin exchange. k_{se} and k_{sr} are the spin exchange and spin relaxation coefficients with Rb and η_{A-He} is the alkali spin exchange efficiency.

Alkali	D2 (nm)	D1 (nm)	T_{melt} (C)	k_{se}^{Rb-A} (10^{-10}cm^3/s)	k_{sr}^{Rb-A} (10^{-14}cm^3/s)	η_{A-He}
Na	588.99	589.59	97.81	7.9	17.5	0.88
K	766.49	769.896	63.25	10.1	21.8	0.24
Rb	780.03	794.76	38.89	8.4	48.1	0.026
Cs	852.11	894.35	28.40	9.8	199.5	0.008

The spin exchange cross section between Rb and K is also so large that spin exchange rate is on the order of 10^5 s^{-1} for typical densities while the spin relaxation rate is 500 s^{-1}. This means the alkali are in spin temperature equilibrium [62] and have equal electron spin polarization simplifying Eq.(4.8)

$$\frac{dP_{He}}{dt} = \gamma_{SE}(P_A - P_{He}) - \Gamma_{He}P_{He}. \tag{4.9}$$

Where $\Gamma_{SE} = \kappa_K[\text{K}] + \kappa_{Rb}[\text{Rb}]$, κ_K and κ_{Rb} are the spin exchange coefficients and [K] and [Rb] are the alkali densities and P_A is the volume averaged alkali polarization. Solving for the ^{3}He polarization [66]

$$P_{He}(t) = \frac{\gamma_{SE}}{\Gamma_r}P_A(1 - e^{\frac{-t}{\tau_u}}). \tag{4.10}$$

44
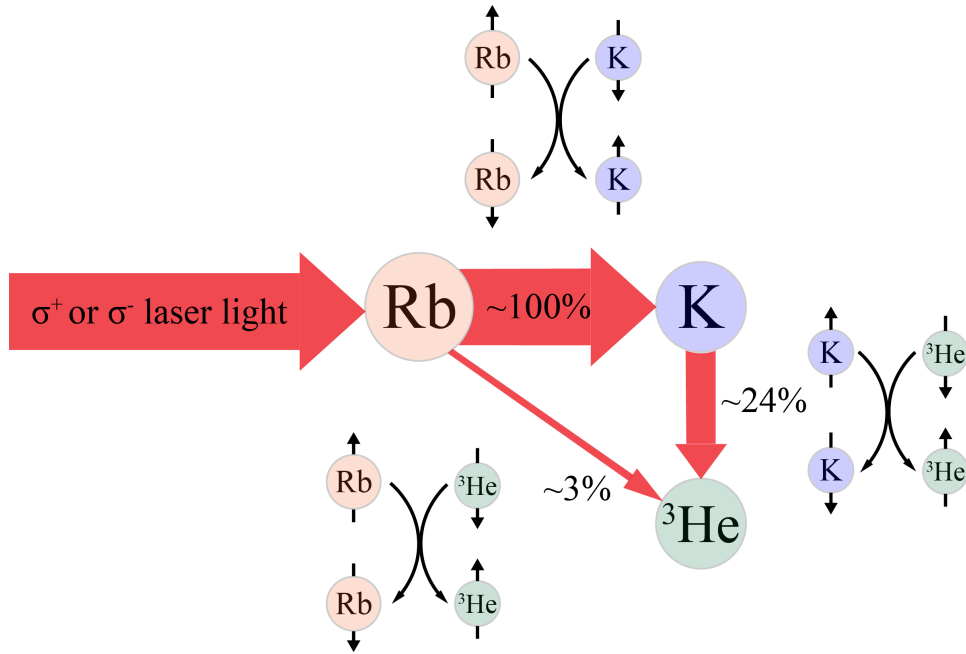
Figure 4.2: Flow of angular momentum from the pumping laser light into the ^{3}He nuclear spin. Both the Rb and K spin exchange with the ^{3}He atoms but the K does it much more efficiently.

With $\Gamma_r = \gamma_{SE} + \Gamma_{He}$, $\tau_u = \frac{1}{\Gamma_r}$ is a time constant that describes the rate at which the ^{3}He polarization increases. The result is an equation similar to Eq.(4.5) with the alkalis contributing a combined spin exchange coefficient. Overall the combined potassium and rubidium in a hybrid SEOP cell lose less angular momentum per atom due to spin relaxation than a traditional SEOP cell. This leads to more of the angular momentum of the pumping light being transferred to the ^{3}He nulcei which results in faster ^{3}He polarization gains and larger maximum polarization. The time for a cell to reach maximum polarization or the "pump up" time for pure Rb cells with a high ^{3}He density is on the order of 8 hours, while comparable hybrid cells will have a pump up time of 4 hours. Much work has also been done to determine the ideal ratio of alkali vapor densities to use as this has a large effect on the polarization dynamics of the cell. Numerical simulations [67] as well as experimental test [68] have shown that the optimal ratio $\mathcal{D} = [\text{K}]/[\text{Rb}]$ to be around 6 with a ratio of more than

10 being detrimental to the overall pumping rate.

4.1.4 ^{3}He Spin relaxation

The spin relaxation of the ^{3}He nuclear spins is the primary limit to the maximum polarization achievable through SEOP. There are three main factors that contribute to the spin relaxation Γ_{He} as mentioned in the previous section, the diffusion of the helium atoms through magnetic field gradients, dipole-dipole interactions when the helium atoms collide, and collisions of the helium atoms with the walls of the container.

$$\Gamma_{He} = \Gamma_{diff} + \Gamma_{dipole} + \Gamma_{wall}. \tag{4.11}$$

Magnetic field gradients

Gradients of the magnetic holding field will appear as a time varying field to the polarized ^{3}He nucleus and cause the spins to relax away from the holding field direction. The expression for the relaxation rate due to field gradients is derived in Ref.[69]

$$\Gamma_{diff} = D_{He}\frac{|\vec{\nabla}B_x|^2 + |\vec{\nabla}B_y|^2}{B_0^2}, \tag{4.12}$$

and D_{He} is the helium self diffusion constant given by

$$D_{He} = 0.235 \quad \text{cm}^2/\text{s}\Big(\frac{T}{400\text{K}}\Big)^{0.7}\Big(\frac{10\text{amg}}{[^3\text{He}]}\Big). \tag{4.13}$$

Magnetic field gradients of the directions perpendicular to the direction of the applied holding field thus contribute to a slower pumping rate and a smaller maximum polarization. These transverse gradients contribute to the T_1 lifetime of the cell, whereas the longitudinal gradients will contribute to the T_2 lifetime. Reducing these gradients as much as possible is beneficial to the polarization parameters of the cell.

Helium dipole-dipole interaction

During a collision between two helium atoms the nuclear polarization can be destroyed through the magnetic dipole interaction which couples the nuclear spin to the total angular momentum of the colliding atoms. The resulting relaxation rate due to this effect is dependent on the density of the ^{3}He gas. [70] calculates the relaxation rate as a function of density, the calculation is extended in Ref.[66] to typical temperatures used for hybrid SEOP cells.

$$\Gamma_{dipole} = \frac{[^3\text{He}]}{893 \ \text{amg} \cdot \text{hrs}}. \tag{4.14}$$

This represents the theoretical minimum of the relaxation rate for a ^{3}He cell though in practice other factors are always much larger.

Helium wall collisions

The relaxation rate due to the collision of the helium atoms with the wall of the cell is the least well known of these three relaxation rates. The effect has several possible origins: contaminants of the surface of the glass, micro-fissures in the glass that the helium atoms become trapped in bouncing back and forth, paramagnetic materials inside the glass, but it is not known which of these contribute. Despite the uncertain knowledge of its origin, an empirical method has been developed to make cells that reduce wall relaxation losses well below other loss factors.

4.2 The Target System

The target system consists of everything need to house and polarize the hybrid SEOP cells used in the magnetic Faraday rotation experiment. The helium cells are supported inside an oven to vaporize the alkali metals, the oven is suspended above a table mounted on a vibrational damping system in order to reduce movement of the cell. The oven is inside a shielding box that protects the other equipment in the lab should one of the cells explode due to the high pressures they are under. The box has
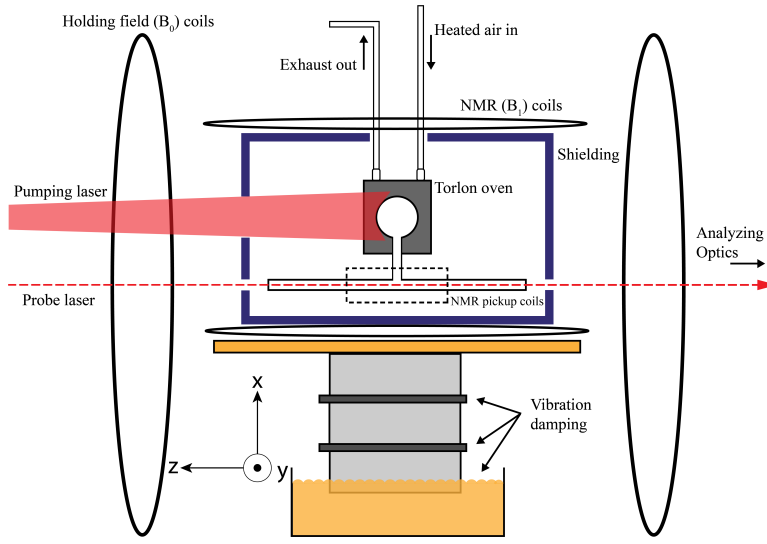
Figure 4.3: Setup of the polarized ^{3}He target system: side view

holes in the front and sides and top for the pumping and probe laser beams, EPR photodiode, and oven airflow system. The table and everything contained in the shielding box sits inside a large pair of helmholtz coils that generate the longitudinal holding field. Additionally, a pair of Helmholtz coils sit on the table and surround the cell to provide a transverse magnetic field for NMR. On the wall next to this setup is an airflow system for heating up the oven. In front of this setup is a table that contains the pumping laser and all the polarizing optics needed for it. This section will describe these systems in more detail.

4.2.1 The ^{3}He SEOP cells

The helium cells used in the experiment are both high pressure hybrid SEOP cells meaning both contain Rb and K in addition to the large amount of ^{3}He and nitrogen gasses. Both cells are Jefferson Lab style cells designed for use in an electron beam and were made by Mike Souza at Princeton and filled by Todd Averett at the College of William and Mary. They have a spherical pumping chamber (PC) on top connected by a cylindrical transfer tube (TT) to a cylindrical target chamber (TC) on the bottom. The pumping chamber contains the metallic alkali metals and
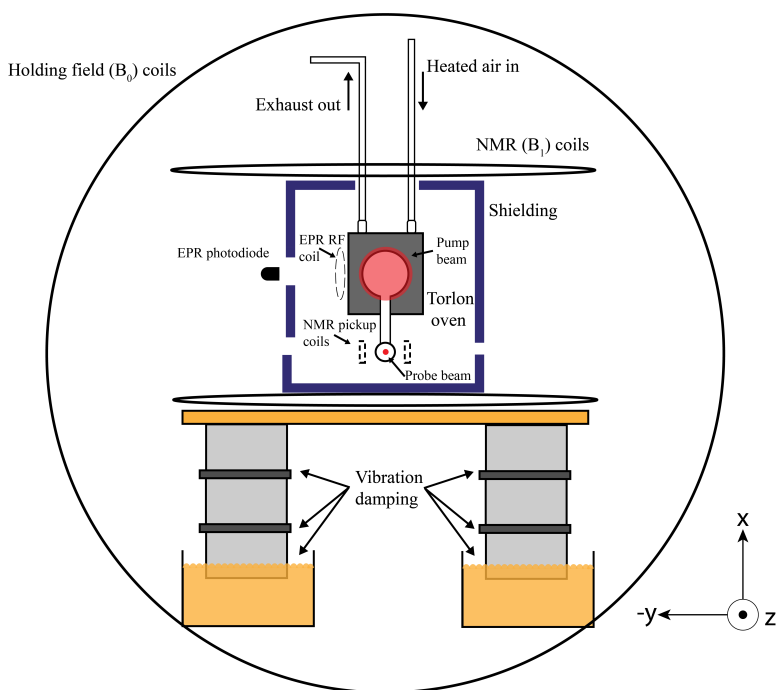
Figure 4.4: Setup of the polarized ^{3}He target system: front view

is usually heated to around 230° C in order to vaporize them. Consequently, the pumping chamber is also where the 795 nm light from the pumping laser is directed. The target chamber in this experiment is where the probe laser beam for measuring the Faraday rotation passes through.

Initial cell: Dale

The first cell used is labeled Dale, it is blown from GE180 aluminosilicate glass that has a high density so the gases do not escape. The cell measurements are shown in Fig.(4.5), the wall thickness of the glass is 1.8 mm. Dale was intended for use at Jefferson National Lab but was never used due to the comparatively low max polarization ($\sim$40%), it has hemispherical end windows designed to be much thinner ($\sim$100μm) than the average wall thickness to allow for minimal scattering of the electron beam. When used with a probe laser beam the windows, which have a non-

uniform thickness, act like lenses and cause divergence of the laser beam. This means that the probe laser can only be passed through the target chamber a single time even with additional lenses to compensate for the effect. Additional cell parameters are shown in Table.(4.2)
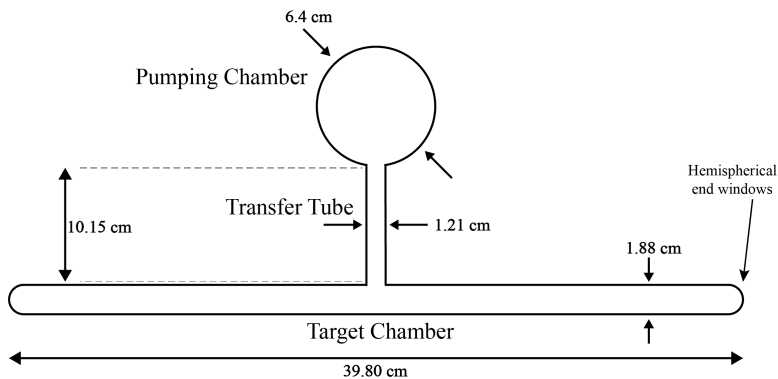
Figure 4.5: Dimensions of the hybrid cell Dale

Parameter	Value
$\mathcal{D}$	~25
Fill density	8.34 amg
PC density (at 240 C)	6.94 amg
TC density (at 240 C)	10.47 amg
PC volume	97.99 ml
TC volume	71.30 ml
TT volume	2.59 ml

Table 4.2: Dale cell parameters

Where the pumping chamber and target chamber densities are calculated from

$$n_{PC} = \left[\frac{1+\nu}{t+\nu}\right] \qquad n_{TC} = \left[\frac{1+\nu}{t+\nu}\right]t \qquad (4.15)$$

$$\nu = \frac{V_{PC}}{V_{TC}} \qquad t = \frac{T_{PC}}{T_{TC}}. \qquad (4.16)$$

With the temperatures of the pumping and target chamber given in Kelvin and the volume of the pumping chamber and target chamber are V_{PC} and V_{TC}.

Multipass cell: Vivian

In an effort to increase the size of the expected magnetic Faraday rotation from ^{3}He a new cell was built. Building a cell with a higher density was not possible as the setup was not designed to accommodate a cell with a higher pressure than Dale. In addition, higher densities usually involve lower polarization as the dipole-dipole and wall collisions increase. Hence, in order to increase the size of the rotation a new cell that could have multiple passes of the probe laser beam was built, it was named Vivian. Vivian is made from Corning 1720 glass, which is structurally very similar to GE180, and is close to the same dimensions as Dale. Corning 1720, like GE180, is very resistant to the alkali metals and has been shown to have long relaxation times [71]. Instead of thin, spherical end windows Vivian has flat end windows made from Corning 1723 glass and coated with an anti-reflective coating with a range of 600-800 nm. The flat end windows were attached with kovar seals to a cylindrical target chamber, because these do not handle pressure as well as spherical windows the fill density of Vivian had to be less than Dale. Table. (4.3) contains the cell parameters
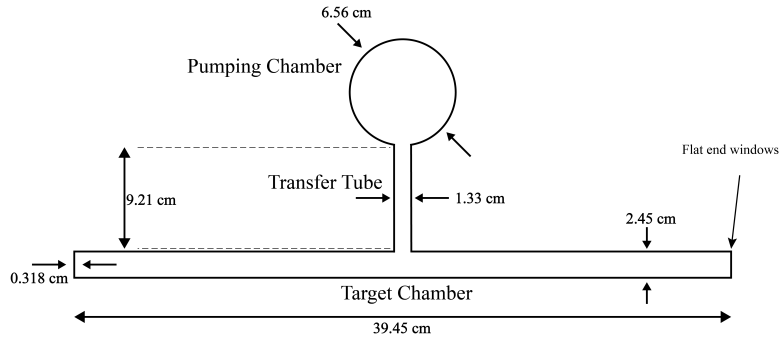
Figure 4.6: Dimensions of the hybrid cell Vivian

Parameter	Value
$\mathcal{D}$	~ 6
Fill density	3.6 amg
PC density (at 240 C)	2.81 amg
TC density (at 240 C)	4.40 amg
PC volume	124.72 ml
TC volume	127.89 ml
TT volume	3.56 ml

Table 4.3: Vivian cell parameters
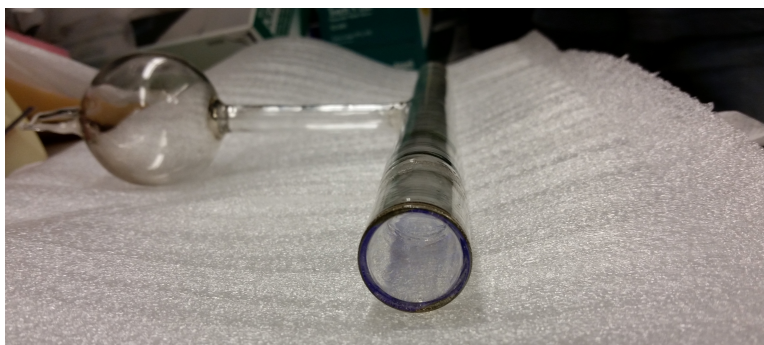
Figure 4.7: Vivian flat end window

4.2.2 Oven and airflow system

The pumping chamber of the helium cell is supported inside an oven during the experiment. Essentially, it is a box constructed of a plastic called Torlon that can withstand the high temperatures needed and remain nonmagnetic to reduce field gradients. It is supported on 4 wood rods, used for their small coefficient of thermal expansion, that connect to the table. The box has 7.6 cm diameter windows in the front and side and top for the pumping laser and EPR measurements, respectively. In order to vaporize the metallic alkali metals the oven has to be heated to $\sim 240°$ C to evaporate the potassium and ensure the proper density ratio. The oven has an inlet and outlet on top for the circulation of heated air. Compressed air is passed through two 1 kW heaters then through a few sections of stainless steel pipe wrapped

in insulation connected to the inlet of the oven. The air blown into the oven must be hot enough to maintain a stable temperature so the heaters are connected to a PID feedback system that adjust the current to change the temperature of the air. A resistive temperature device is placed inside the oven to measure the temperature and one is connected to the heater as part of the feedback loop. The stability of the temperature inside the oven varies with the stability of the temperature in the laboratory but usually maintains the set temperature to within 5° C. The oven also has arms that attach to the bottom and contain hooks to the support the target chamber of the cell as shown in Fig.(4.8).
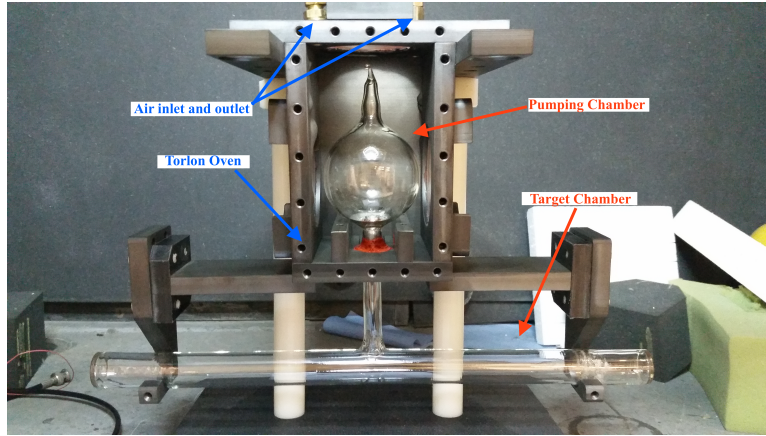
Figure 4.8: Oven with the side removed and the cell Vivian inside

4.2.3   Holding field coils

To generate the holding magnetic field $(\vec{B}_0)$ to which the nuclear spins will align themselves a large pair of helmholtz coils were used. The water cooled coils have a diameter of 172 cm and can produce fields up to 40 G. Typically the magnetic field is set to 21 G while running the magnetic Faraday rotation experiment. The coils are aligned so that the magnetic field is along the direction of the probe laser beam ($\hat{z}$ axis in the laboratory coordinates) that is used to measure Faraday rotation, the height of the beam is also adjusted so it passes through the center of the coils. According to the design, the magnetic field they produce is uniform in a 40 cm^2 square box

in the center, this is larger than the size of the helium cell. In practice the probe laser passes through the target chamber on the bottom of the helium cell, hence the SEOP cell is slightly outside the uniform region. In order to get a measure of the uniformity around the helium cell the transverse $(\hat{x}, \hat{y})$ gradients were measured at a few places around the cell. Fig.(4.9) summarizes the results at the front of the target chamber and the back. The field gradients were measured to less than 30 mG/cm across the cell dimensions. A more stable holding field was desired to aid in the overall precision of the experiment as ^{3}He polarization measurements are dependent on the magnetic field. Therefore, a feedback system was installed to stabilize the field. A three-axis fluxgate field sensor is placed inside the coils and connected to a PI circuit box initially designed for EPR measurements (see EPR section). The output of the box is connected to the power supply driving the coils and reduces fluctuations. In addition to the feedback system special care was taken to move all metallic and possibly magnetic materials as far away from the field as possible.
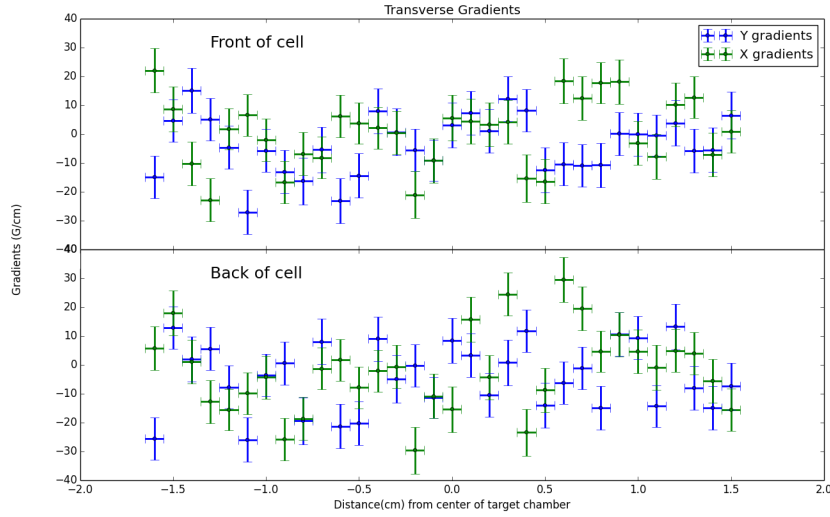
Figure 4.9: Transverse field gradients in the directions perpendicular to the holding field as measured at the front and back of the target chamber of the SEOP cell. Most measurements were smaller than 30 mG/cm.

4.2.4 Pumping laser and polarizing optics

Perhaps the most important piece involved in SEOP after the helium cell is the laser used to optically pump the Rb atoms. In order to polarize ^{3}He one must be able to polarize large volumes of gaseous Rb at high densities. It is ideal to have a large pumping rate as shown in Eq.(4.2) and to accomplish this a large amount of photon flux is needed. Specifically, a large amount of photons that have a wavelength inside the absorption linewidth of the Rb atoms. Originally, early SEOP experiments used dye or Ti:Sapphire lasers [72] but these often have less than 10 W of power which is not suitable for dense targets. Most spin exchange optical pumping today is done with diode array bars (DAB) which contain several emitters that can provide a few hundred watts of power inexpensively. The first lasers used in this experiment to polarize ^{3}He were three Coherent fiber array packages (FAP) that could ideally provide 30 W each. The fiber outputs of the lasers were combined in a 3-1 combiner that was directed onto the polarizing optics to produce the circular polarization. A diagram of the polarization optics is shown in Fig.(4.10). Light from the laser is passed through a series of lenses to increase the beam size enough to cover the pumping chamber (~ 3 in) of the helium cell. It is then directed into a polarizing beam splitting cube which separates the light into two components, s wave with linear polarization perpendicular to the plane of reflection and p wave with linear polarization parallel to the plane of reflection. One of these components passes straight through the cube and reflects off a mirror into a quarter-wave plate to become circularly polarized. The other component is reflected inside the cube, it passes through a quarter-wave plate obtains a circular polarization then reflects off a mirror which reverses the helicity of the circular polarization. Upon passing through the same quarter-wave plate as before the $s(p)$ component has now been converted into $p(s)$ and goes back through the cube and towards the cell via another quarter-wave plate. Thus, the polarizing setup converts all of the light from the laser into the same circular polarization incident upon the cell.
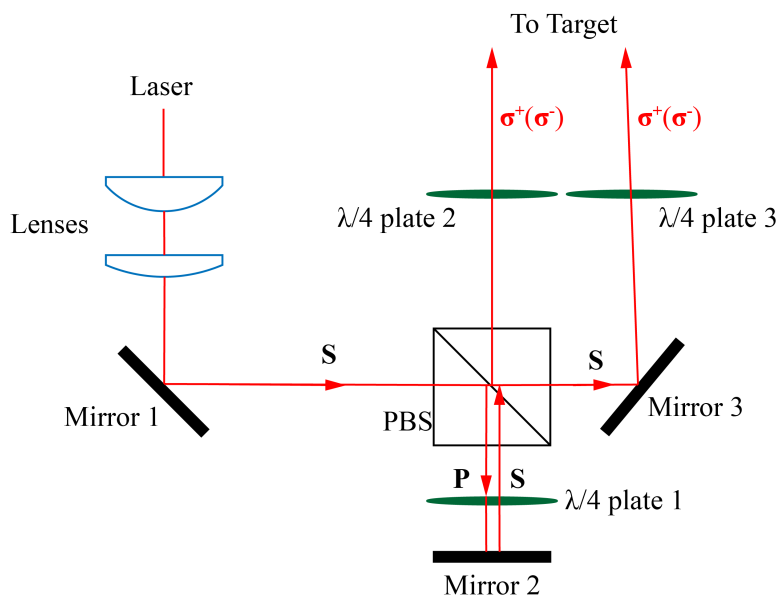
Figure 4.10: Polarizing optics for the 795 nm pumping laser. The light is split with a polarizing beam splitting cube that separates the light into two linear components that can both be turned into circular polarization so all of the light is used.

Narrowband pumping laser

The three Coherent FAPs did not provide the maximum 90 W possible, due to aging effects the total combined output from the lasers was 46 W. This, combined with the fact that these lasers have a broadband spectrum, means that they needed to be replaced to improve the polarization parameters of the helium cell. When viewed in a spectrometer, the width of the wavelength spectrum of the FAPs was 5 nm (2400 GHz). This is very poorly matched to the linewidth of the Rb D1 resonance as the natural linewidth is 5.7 MHz. However, due to the presence of the highly dense helium gas the resonance experiences significant broadening of 20 GHz/amg$_{He}$ [66, 73]. For a dense helium cell such as used in this experiment this increase the line width to ∼100 GHz. Even with the sizeable pressure broadening the spectral width of the FAPs is still broad enough that a large portion of the photon flux is not polarizing the Rb atoms. Therefore, a narrowband DAB laser that has a smaller

spectral width was constructed to improve the polarization of the alkali metals and consequently the ^{3}He gas. The diode array bars are from nLight and comprised of 63 individual broad area emitters sandwiched between two copper pieces with micro-channels inside that allow the DAB to be liquid cooled. The DAB has a fast axis collimation with a cylindrical microlens attached to the front, this narrows the wide divergence typical diodes lasers have. The diode is attached to a custom mount that has an inlet and outlet for the water flow from a Newport CES-05 Thermorack 401 chiller. The mount and the water chiller form a closed loop that has a bypass and an additional flow meter to measure the flow rate and keep it within the recommended 0.250 Lpm. The chiller can control the diode temperature to within 1° C to allow the central wavelength of the different diodes to be shifted to the Rb resonance. The full setup of the laser is shown in Fig.(4.12). The DAB typically have a a full power output of 100 W and a spectral width of 2 nm (1000 GHz), this is still relatively broad compared to the Rb resonance and can be narrowed further with the use of an external cavity [74]. The grating in this setup is a Volume Holographic Grating (VHG) which has a periodic phase or absorption perturbation inside the volume of the grating as opposed to on the surface. This changes the Bragg condition as shown below
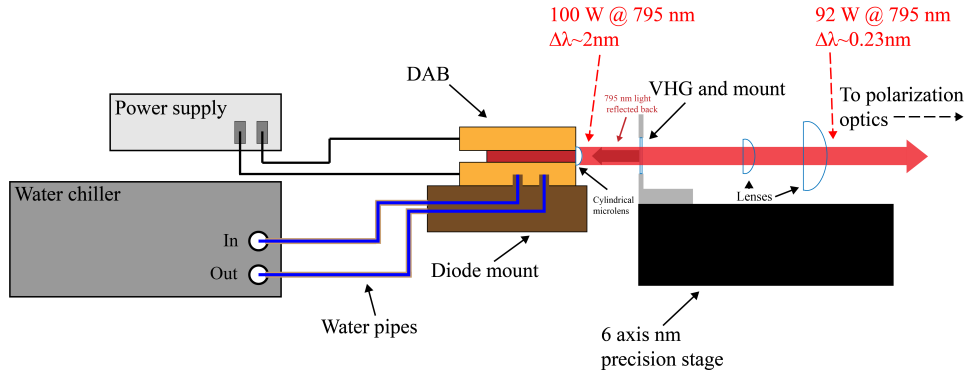
Figure 4.11: Schematic setup of the DAB external cavity. The grating sits on a mount attached to a 6 axis stage that allows for control of the angles of the grating to narrow the diode output.

$$k_i \sin \theta_i + k_d \sin \theta_d = mG \tag{4.17}$$

$$k_i \sin \theta_i + k_d \sin \theta_d = G_{\parallel}$$
$$k_i \cos \theta_i - k_d \cos \theta_d = G_{\perp}. \tag{4.18}$$

Where $|\vec{k}_i| = |\vec{k}_d| = \frac{2\pi}{\lambda}$, θ_i, θ_d are the angles of incidence and diffraction, and G is the grating spacing. The first equation can be satisfied for many different wavelengths and diffraction orders m, whereas the last two for the VHG have only one wavelength solution for given angles θ_i, θ_d. This means the diffraction from a VHG only occurs around a small selection of wavelengths leading to a narrower spectrum. The grating used for the narrowband laser is a 2 cm long VHG from Ondax with a diffraction wavelength centered on 794.4 nm. It is mounted in an aluminum mount attached to a 6 axis, nanometer precision stage that can translate along three axes and rotate along three axes. The stage enables the angle of the grating with respect to the DAB to set accurately enough to match the strict angular conditions needed for diffraction. Once aligned, light at 794.4 nm is diffracted back from the grating into the diode and forces the emitters to lase at that wavelength. This significantly narrows the wavelength spectrum as shown in Fig.(4.12)

The width of the spectrum goes from 2.8 nm (1300 GHz) to 0.23 nm (110 GHz) by using the VHG to form an external cavity laser. The efficiency of the grating is about 93%, after the losses from the lenses about 91% of the original laser power remains in the narrowed peak. The width of the narrowband pumping laser is almost the same width as the Rb D1 line inside the high pressure helium cell. Therefore most of the optical power from the laser is going towards the alkali polarization leading to faster ^{3}He polarization rates and higher maximum polarization.

4.3 ^{3}He Polarimetry

In order to measure the polarization of the ^{3}He atoms two separate techniques were utilized. The first is Nuclear Magnetic Resonance (NMR) using the Adiabatic Fast Passage (AFP) technique. This is the primary polarization monitor for the experiment and measurements were collected while the ^{3}He spins were modulated. How-
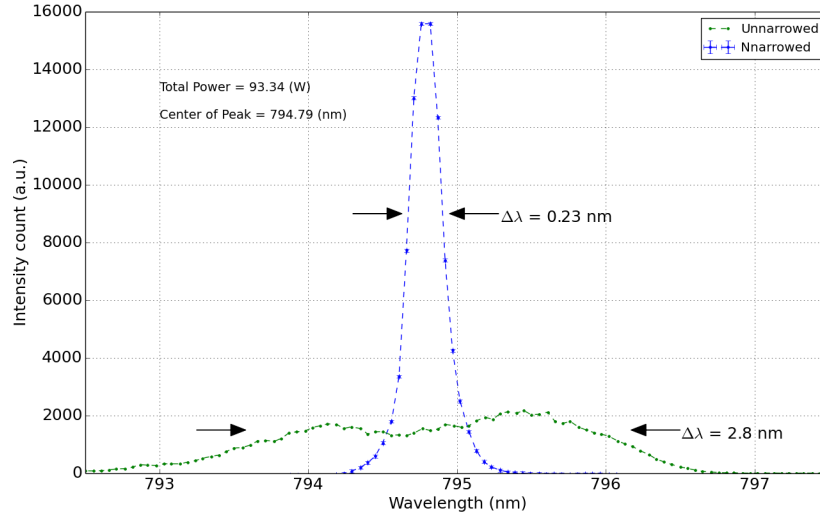
Figure 4.12: Wavelength spectrum of DAB in the narrowed versus un-narrowed alignment. In the narrowed alignment all of the power is contained inside the peak with full width half maximum of 0.23 nm. The width is roughly the same as the Rb D1 resonance.

ever, NMR only provides a relative measurement and thus must be calibrated with another, absolute measurement. The second technique is Electron Paramagnetic Resonance (EPR) frequency shift polarimetry and provides an absolute measurement for comparison with NMR. In the following sections both the methods and how to extract the ^{3}He polarization from them will be described.

4.4 Nuclear Magnetic Resonance

NMR is a technique to determine ^{3}He polarization based on the magnetic field produced by the nuclear spins. The B_{He} is small under typical conditions, usually a few mG, and is surrounded by much larger fields, consequently the AFP technique is used to isolate B_{He}. Normally, the spins are aligned with a static "holding" magnetic field $\vec{B}_0$. By exposing the spins to a separate, transverse oscillating $\vec{B}_1$ field AFP can be used to reverse their orientation (i.e."flip the spins") with respect to the

holding magnetic field. The change in $\vec{B}_{\text{He}}$ is then detected by the current induced in a pickup coil which will provide a voltage proportional to the ^{3}He polarization.

4.4.1 Adiabatic Fast Passage

According to the classical theory of electromagentism, a free particle with spin $\vec{I}$ and magnetic moment $\vec{M}$ in a magnetic field $\vec{B}_0$ will experience a torque given by

$$\vec{\tau} = \vec{M} \times \vec{B}_0. \tag{4.19}$$

Rewriting the torque as the rate of change of angular momentum $\vec{\tau} = \frac{d\vec{I}}{dt}$ and recognizing that $\vec{M} = \gamma \hbar \vec{I}$ where γ is the gyro-magnetic ratio yields

$$\frac{d\vec{M}}{dt} = \gamma \vec{M} \times \vec{B}_0. \tag{4.20}$$

The static magnetic field puts a torque on the magnetic moment of the particle and causes it to process about this holding field as shown in Fig.(4.13). The frequency the magnetic moment oscillates at is called the *Larmor frequency* and is related to the holding field and the gyro-magnetic ratio $\omega_{Larmor} = \gamma |B_0|$.
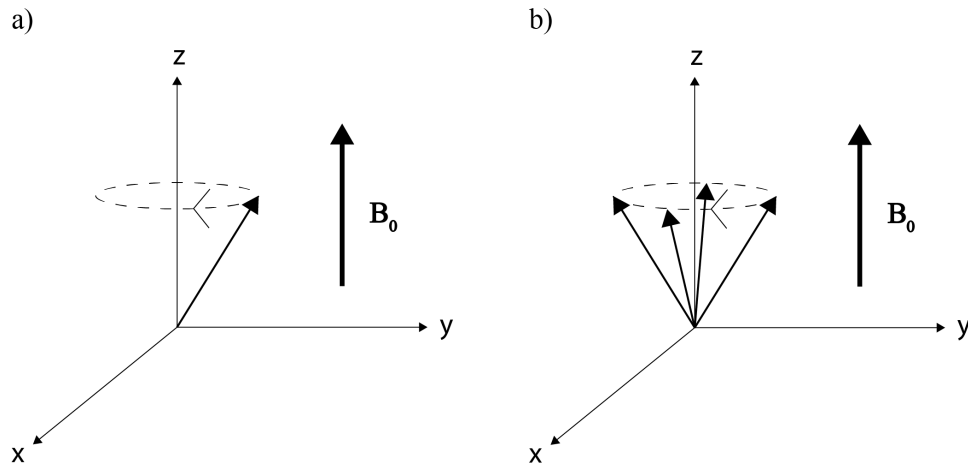
Figure 4.13: a) Magnetic moment oscillating about holding field b) Ensemble of magnetic moments oscillating about holding field

Equation(4.20) is valid in the laboratory frame of reference, by moving to a rotating reference frame that rotates about the axis of the holding field with angular

frequency $\vec{\omega}$ the system can be conceptually simplified, [75]. The relation between the change of magnetic moment between the two frames is

$$\left(\frac{d\vec{M}}{dt}\right)_{lab} = \left(\frac{\partial\vec{M}}{\partial t}\right)_{rotating} + \vec{\omega} \times \vec{M}. \tag{4.21}$$

Combining Eq.(4.20) and Eq.(4.21) we can write the equation for the motion of the magnetic moment in the rotating frame

$$\left(\frac{\partial\vec{M}}{\partial t}\right)_{rotating} = \gamma\vec{M} \times \vec{B}_0 - \vec{\omega} \times \vec{M} \tag{4.22}$$

$$\left(\frac{\partial\vec{M}}{\partial t}\right)_{rotating} = \gamma\vec{M} \times (\vec{B}_0 + \frac{\vec{\omega}}{\gamma}). \tag{4.23}$$

Comparing Eq.(4.23) with the equation for the laboratory frame shows that in the rotating frame the holding field $\vec{B}_0$ has been replaced by an effective field

$$\vec{B}_{eff} = \vec{B}_0 + \frac{\vec{\omega}}{\gamma}. \tag{4.24}$$

Thus, in the rotating frame the magnetic moment precesses around the effective field just as it precesses about the holding field in the laboratory frame. If we set the frequency of the rotating frame equal to the Larmor frequency $\omega = \omega_{Larmor} = -\gamma|B_0|$ then the magnetic moment becomes a constant of motion in the rotating frame, [76]. To manipulate the spins to perform a measurement an RF field is added to the transverse $\hat{x}$ direction. Denoting the RF field by $\vec{B}_1 = B_1 \cos(\omega t)\hat{x}$ and adding to Eq.(4.23) gives

$$\left(\frac{\partial\vec{M}}{\partial t}\right)_{rotating} = \gamma\vec{M} \times (\vec{B}_0 + \frac{\vec{\omega}}{\gamma} + \vec{B}_1). \tag{4.25}$$

If the transverse field is oscillating at the Larmor frequency then

$$\left(\frac{\partial\vec{M}}{\partial t}\right)_{rotating} = \gamma\vec{M} \times \vec{B}_1. \tag{4.26}$$

The magnetic moment is tilted away from the holding field on the $\hat{z}$ axis towards the $\hat{y}$ axis. In the lab frame the magnetic moment is rotating around the holding field as shown in Fig.(4.14).

$\omega \ll \omega_{Larmor}$

$\omega = \omega_{Larmor}$

$\omega \gg \omega_{Larmor}$

Rotating Frame   Laboratory Frame
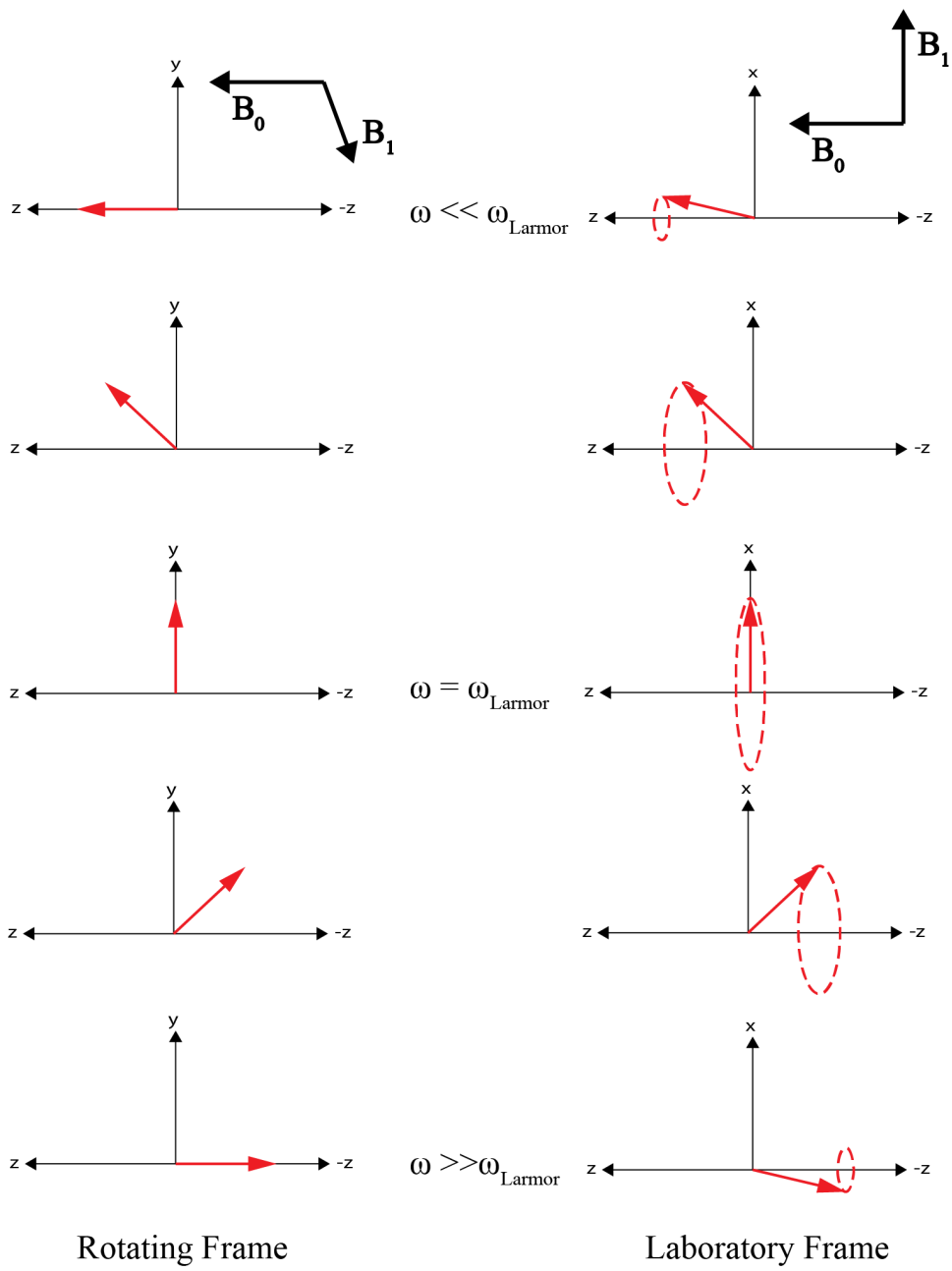
Figure 4.14: Motion of the magnetic moment in the laboratory frame and the rotating frame during a frequency sweep

Hence the addition of the transverse field allows the system of magnetic moments to be perturbed away from equilibrium. If the frequency of the transverse field is far below the Larmor resonance frequency the effective field is parallel to the holding field. Slowly changing ω results in the spins following the effective field as it tilts away from the holding field until they are perpendicular to it when $\omega = \omega_{Larmor}$ and then anti-parallel when $\omega > \omega_{Larmor}$. This allows the spins to be "flipped" and reverse their orientation with respect to the holding field. In order for the spins to follow the effective field the adiabatic fast passage conditions must be met [77]. The change in frequency must be fast enough that the spins do not have time to relax during the sweep by interaction with field gradients (*fast condition*). The change must also be slow enough that the spins have time to follow and not be left behind (*slow condition*). These conditions are derived for frequency sweep NMR in Ref.[78, 79] and are given by

$$\frac{|\gamma B_1|}{T_2} << |\dot{\omega}| << \gamma^2 B_1^2. \tag{4.27}$$

Where T_2 is the transverse ^{3}He relaxation time, the ^{3}He gyromagnetic ratio $\gamma = 3.24$ kHz/G, and B_1 is the transverse field amplitude. For typical values of B_1 used in the experiment ($B_1 \approx 200$mG) the adiabatic conditions are 0.082 kHz/s$\ll |\dot{\omega}| \ll 16.61$ kHz/s. Whereas the sweep rates used in the experiment were between 1 kHz/s and 10 kHz/s.

4.4.2   Measurement procedure and electronics setup

When the frequency of the $\vec{B}_1$ field reaches the resonance the nuclear spins are perpendicular to the holding field and oscillating at the frequency of the transverse field ω_1. This motion of the spins results in a changing magnetic field which is proportional to the polarization of the ^{3}He gas [80, 81]. A pair of "pickup" coils are placed on either side of the target chamber of the helium cell as shown in Fig.(4.15). The changing flux due to the oscillating magnetic field from the spins induces an oscillating voltage in the coils which is detected by a lock-in amplifier referenced to ω_1. While the spins are far away from resonance the induced voltage is small but
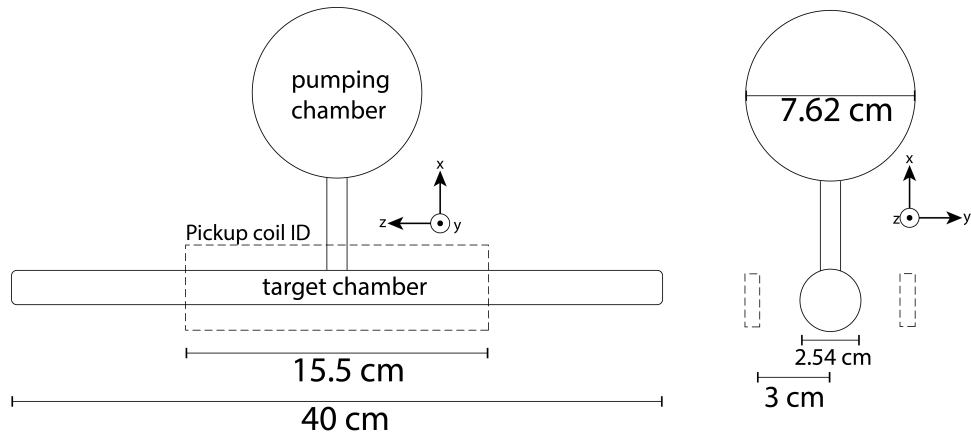
Figure 4.15: NMR pickup coils positions

when they reach resonance the voltage is much larger. The pickup coils are each a 15.5 x 2.2 cm^2 rectangle wound with 200 turns and oriented perpendicular to both the holding field and the transverse field. The coils sit on mounts so their angle with respect to these fields can be adjusted to reduce the background noise from these fields. The coils are wound in opposite directions and each is connected to one input (A and B input) of a low noise pre-amplifier (SR560). The signals are subtracted to get rid of common background noise and the output (A-B) of the pre-amplifier is then sent to a lock-in amplifier (DSP 7270) which is then read with a computer. Each time before the experiment is run the coils are adjusted so that the (A-B) voltage read in the lock-in amplifier is as small as possible. The full setup is shown in Fig.(4.16).

The coils for the $\vec{B}_1$ field are driven by a sweep function generator (Agilent 3324A) connected to an amplifier and controlled by the computer. Typically, for frequency sweep NMR, the frequency of the field is swept over a range of 10 kHz at a rate of 1.5 kHz/s to stay within the adiabatic fast passage conditions. For example, while the holding field is kept at a constant 21.5 G, corresponding to a Larmor frequency of 69.66 kHz, the transverse field is swept from 64 kHz to 74 kHz over 6.5 s. An example NMR signal is shown in Fig.(4.17).

The figure shows the voltage in the lock-in amplifier as the frequency is swept through

64
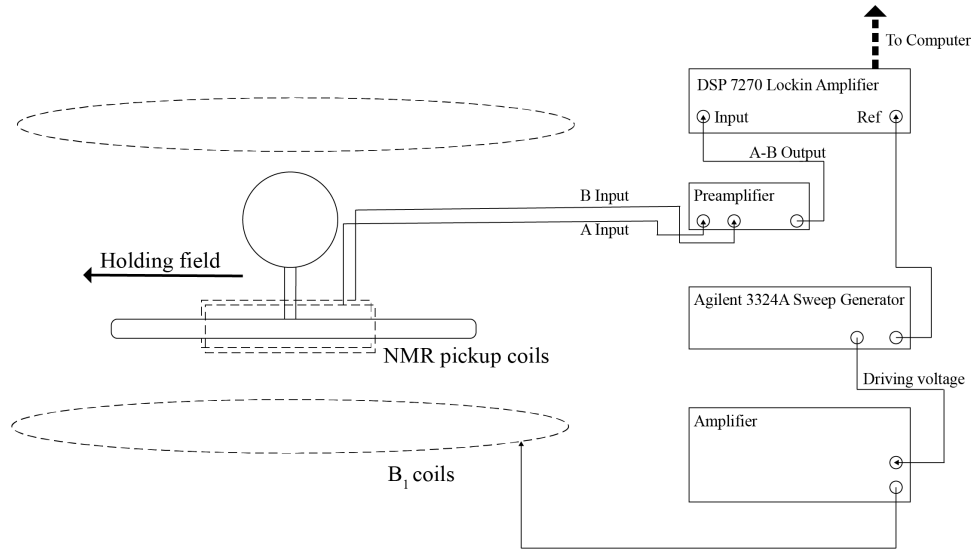
Figure 4.16: Electronics setup for NMR

the resonance. The voltages are stored in a curve buffer during the frequency sweep and then read by the computer once the sweep is finished. As the spins are tilted further and further away from the holding field axis, while following the frequency sweep, the voltage detected increases until it reaches a maximum when the spin are perpendicular. Then decreases as the spins flip over and become aligned in the opposite direction. The height of the peak is proportional to the transverse component of the ^{3}He magnetization and thus the polarization. The signal is fitted to the square root of a Lorentzian function in order to obtain the peak height.

$$F \propto \frac{\omega_c}{\sqrt{(\omega - \omega_0)^2 + \omega_c^2}}. \tag{4.28}$$

Where ω_0 is the Larmor frequency, ω is the frequency of the transverse field and ω_c is a factor related to the height and width of the peak which are given by $\frac{2}{\pi\omega_c}$ and ω_c respectively. With the extracted peak height comes a measure of the polarization, however it is only a relative measurement and must be calibrated with an absolute measure of the polarization.

65
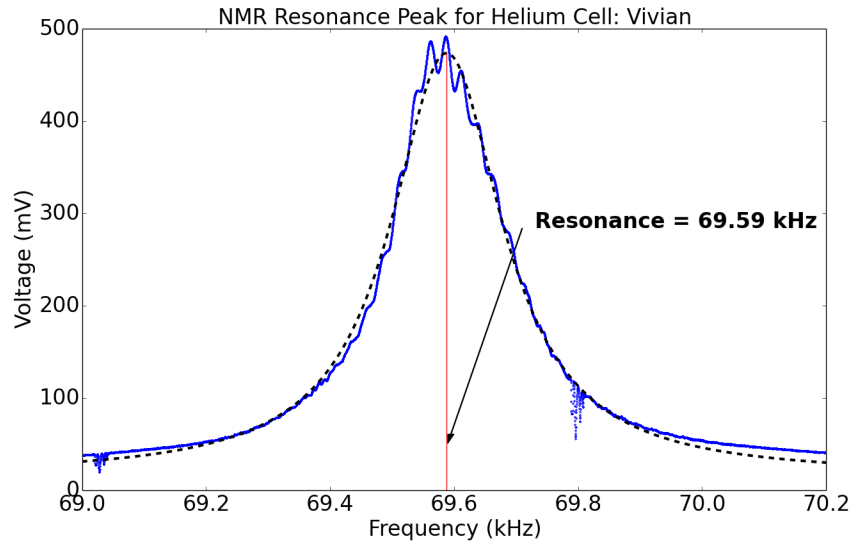
Figure 4.17: NMR frequency sweep with Lorentzian fit

4.4.3 NMR sweep parameters

During an NMR sweep there will always be a small amount of polarization losses. The losses can be caused by a number of effects: violating the AFP sweep conditions, having a B_1 amplitude that is too small, and exotic phenomena such as "masing" [78] where currents induced in the small ring of solid Rb in the pumping chamber or coupling of the ^{3}He magnetization to the NMR coils [78] reduce the polarization. For this experiment, because the overall signal is proportional to the ^{3}He polarization we want to achieve as high a polarization as possible. In addition, the spins are being constantly flipped with NMR so reducing the polarization loss per flip is a major factor in achieving a high polarization. This section describes various studies done on the NMR setup parameters to determine the optimum conditions to perform the experiment. The first that is evident in Fig.(4.17) is a 60 Hz oscillation on top of the NMR resonance peak that was detected because of the large number of data points in the curve buffer. This is due to some small 60 Hz leakage from the power supply for the static magnetic holding field. Redistributing the power plugs for the equipment to specific outlets in the lab eliminated ground loops though to contribute to the

66

effect. The feedback system to stabilize the magnetic field from the Helmholtz coils reduced the effect further till it is as small as possible in the lab environment.

4.4.4 Masing

Although masing is not very well understood it is easy to dispense with. Regardless of the physical origin of the effect, either coupling to the pick up coils or to a small ring of metal Rb or K in the pumping chamber, it seems to disappear by adding an additional gradient to the holding field [78]. Masing may have been observed a few times during NMR sweeps but only sporadically and was never repeatable. An additional loop of wire was added to one of the helmholtz coils for the holding field and a gradients between 10 mG/cm and 20 mG/cm were applied. Table(4.4) shows the polarization achieved in the cells Dale and Vivian for both high and low energy states and with the gradient coil on and off.

Cell	Spin Orientation	Gradient	^{3}He Pol
Dale	parallel	on	40.2%
	parallel	off	40.5%
	anti-parallel	on	39.7%
	anti-parallel	off	40.1%
Vivian	parallel	on	54.5%
	parallel	off	54.5%
	anti-parallel	on	55.3%
	anti-parallel	off	54.9%

Table 4.4: Maximum polarization for both cells in the high and low energy states with gradient coil

The result is masing was not observed during these measurements and did not seem to be a problem in that it did not occur very often. Further adjustments of the cell position and pickup coil positions inside the fields seemed to eliminate the effect altogether.

4.4.5 B_1 Field Amplitude

The amplitude of the transverse field is also an important factor that affects polarization losses. Not only is the amplitude part of the derivation for the AFP conditions but having an B_1 too small will result in an effective field not strong enough to tilt the spins away from the holding field and an B_1 too large will mean the AFP conditions are no longer true. The amplitude of the RF coils was varied over a small range while the holding field was kept constant and several NMR flips were performed at each value. The results are summarized in Table(4.5). Below 100 mG the field strength had a detrimental effect on the polarization losses whereas above it the losses were mostly the same. For most of the experiment and the systematic tests the B_1 amplitude was set at 200 mG as it no longer became the limiting factor for polarization loss.

Cell	B_1 (mG)	Loss per flip (%)
Dale	40	10.2%
	80	5.3%
	120	1.6%
	160	2.0%
	200	1.2%

Table 4.5: Polarization loss per NMR flip for different B_1

4.4.6 Frequency Sweep Rate

The frequency sweep rate for frequency sweep NMR is one of the largest sources of polarization loss in the experiment. From the derivation for the AFP conditions, if the change of frequency for the RF field is too slow the spins will spend longer inside field gradients of the holding field. This is worse at resonance when the spins are perpendicular to the holding field and more susceptible to gradients, they lose track of the effective magnetic field and depolarize. One method to improve this is too reduce the field gradients of the holding field, in this experiment the gradients were at the level of 20 mG/cm and were reduced as much as possible by removing

excess magnetic material from around the cell. For the other condition, if the change of frequency is too fast the spins cannot follow adiabatically. Thus, the derivation provides a theoretical range the $\dot{\omega}$ must stay between. The given range is very large, therefore several sweep rates were used and the loss per flip measured for each one to determine the rate that would give minimum polarization losses. For each cell, the helium was polarized close to the max value then a series of fast NMR flips was performed.
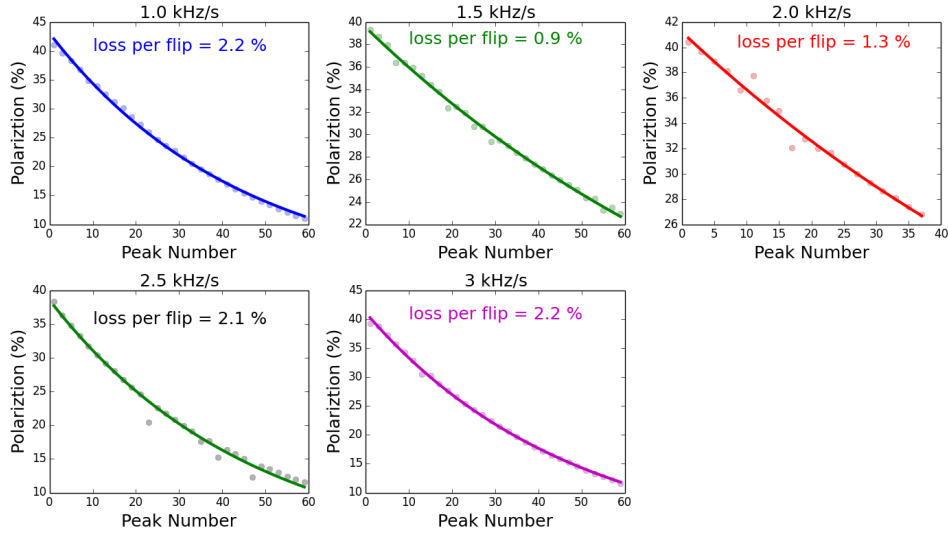
Figure 4.18: Percent polarization loss per flip for different sweep rates for Vivian

The peak heights were extracted then fit to $P_0(1 - \delta)^n$ where P_0 is the initial polarization, δ is the loss per flip and n is the number of flips. Several sweep rates and their corresponding loss per flip are shown in Fig.(4.18). From the figure it is clear that there is a minimum loss per flip of 0.9% at a sweep rate of 1.5 kHz/s for the cell Vivian. Contrary to the wide range calculated theoretically, for this setup there exists a specific minimum which when deviated from the losses increase sharply. A graph with all the sweep rates tested for both cells is shown in Fig.(4.19). Both cells show the same minimum, indicating that the minimum may be specific to the setup and not dependent on the specific cell. When running the experiment the sweep rates with the lowest losses were used.

69
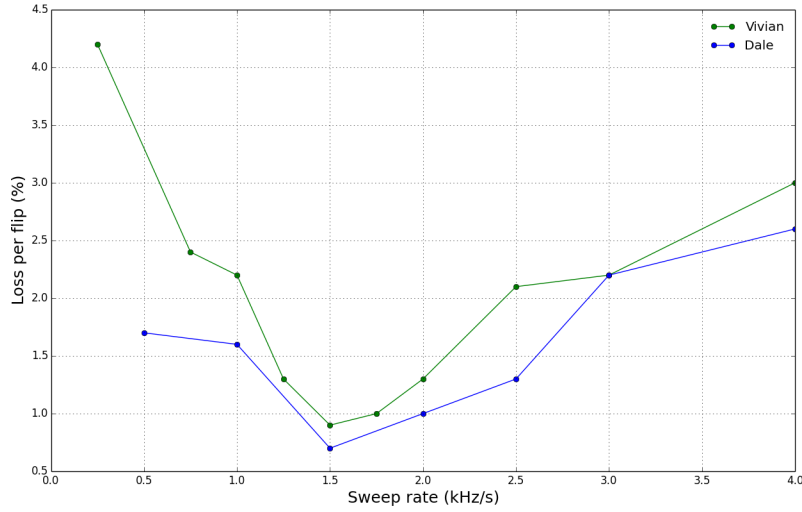
Figure 4.19: Percent polarization loss per flip for different sweep rates for both cells

4.5 Electron Paramagnetic Resonance

Electron Paramagnetic Resonance (EPR) is a form of spectroscopy used to study atoms with an unpaired electron as the energy levels split in an external magnetic field. In the early days of optical pumping, it was observed that the spectra of optically pumped alkali atoms are shifted due to spin exchange collisions [82]. The EPR method here [83–85]is a result of those early efforts, which use the fact that the hybrid ^{3}He cell has a small amount of vaporized rubidium and potassium inside. The alkali atoms see a small ($\sim$10mG) field due to the polarized ^{3}He atoms, this field produces a small Zeeman shift in the spectra of the alkali atoms that is proportional to the ^{3}He polarization and density. The EPR transition is excited with an RF field and then the change in intensity of D2 fluorescence from optical pumping is observed with a photodiode. The frequency of the RF coil is modulated so the signal from the photodiode can be used as an error signal, voltage linearly proportional to the detuning from the EPR transition, so that a proportional/integral feedback loop can be used to lock the frequency. With the frequency locked, the helium spins can be reversed via NMR and the subsequent frequency shift can be isolated from the

70

background. An absolute measure of the ^{3}He polarization can be extracted from the frequency shift and is used to calibrate the NMR peak measured at the same time.

4.5.1 EPR Theory

The high pressure ^{3}He cells used in the experiment have small amounts of Rb and K in the pumping chamber in addition to the large amount of helium gas. Both Rb and K are alkali atoms with their single, outermost electron in an S orbital. The eigenstates of total angular momentum of the atom can be written as $\vec{F} = \vec{I} + \vec{S}$ where $\vec{I}$ is the nuclear spin and $\vec{S}$ is the electron spin. In the presence of a strong external magnetic field $\vec{B}$, F is split into 2F+1 sub-states labeled by m_F. The states for Rb and K are summarized in Table(4.6).

Table 4.6: Common Isotopes of Rb and K with total angular momentum eigenvalues

Isotope	Relative abundance	I	S	F	m_F
^{85}Rb	72.17%	5/2	1/2	2,3	-3,-2,-1,0,1,2,3
^{87}Rb	27.83%	3/2	1/2	1,2	-2,-1,0,1,2
^{39}K	93.26%	3/2	1/2	1,2	−2,-1,0,1,2
^{41}K	6.74%	3/2	1/2	1,2	-2,-1,0,1,2

The 795 nm, circularly polarized light from the pumping laser corresponds to the Rb $S_{1/2} \longrightarrow P_{1/2}$ transition. Light from the laser is absorbed by all the $S_{1/2}$ sub-states of Rb and these get excited to the $P_{1/2}$ state. The process is governed by the selection rule $\Delta m_F = \pm 1$ for right $(+)$ and left $(-)$ circularly polarized light. For right circularly polarized light, an atom in the $m_F = -3$ sub-state of $S_{1/2}$ gets excited to the $m_F = -2$ sub-state of $P_{1/2}$. However, the selection rules for emission are $\Delta m_F = +1, -1, 0$, meaning the atom in the $m_F = -2$ sub-state of $P_{1/2}$ can decay into the $m_F = -3, -2, -1$ sub-states of $S_{1/2}$. There are now less atoms in the $m_F = -3$ sub-state of $S_{1/2}$ than before the light was absorbed. This continues for all of the m_F states until all of the atoms are polarized into the $m_F = +3$ sub-state where there is no where to go due to the selection rule for absorption. Likewise, for

71

left circularly polarized light all of the atoms will end up in the $m_F = -3$ state. This process is illustrated in Fig.(4.20). The Zeeman splitting between the $m_F = \pm 3$ and $m_F = \pm 2$ is then the EPR transition frequency for Rb that is excited with the RF coil. For K the EPR frequency would be between the $m_F = \pm 2$ and $m_F = \pm 1$ states. There are three main factors that contribute to the EPR frequency between these states, the first is the external (holding) magnetic field $\vec{B}_0$, the second is the spin exchange collision between Rb and ^{3}He (or K and ^{3}He), and the third is the small magnetic field from the polarized ^{3}He. The ^{3}He polarization can be extracted from this EPR frequency in the following way. If the variation of the EPR frequency, ν_{EPR} is small with respect to the holding field $\vec{B}_0$ the change in the frequency [85] can be written as
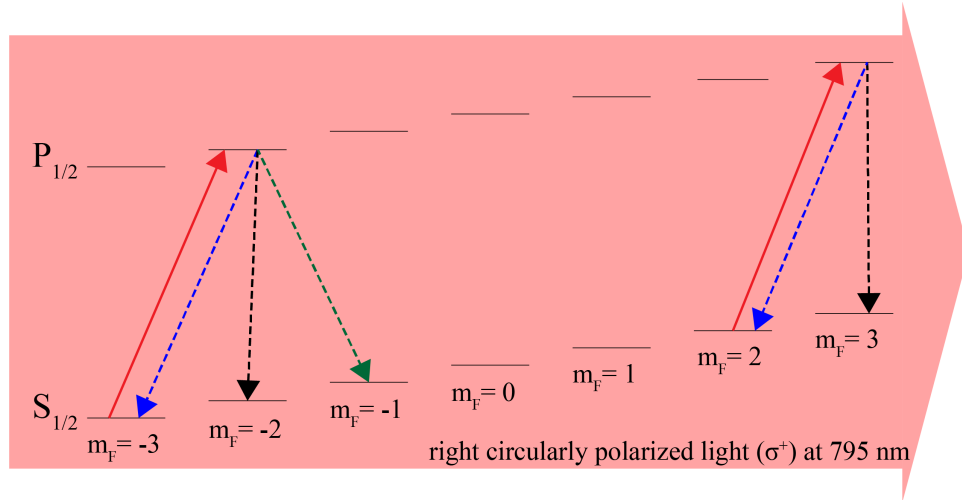
Figure 4.20: Zeeman splitting of energy states in Rb atom. Absorption and selection rules.

$$\Delta \nu_{EPR} = \frac{d\nu_{EPR}}{dB_0} \Delta B_0. \tag{4.29}$$

Where $\frac{d\nu_{EPR}}{dB_0}$ can be calculated from the well known Breit-Rabi formula as shown in Ref.[85]. ν_{EPR} is a combination of three terms as mentioned before

$$\Delta \nu_{EPR} = \Delta \nu_{B_0} + \Delta \nu_{SE} + \Delta \nu_{He}. \tag{4.30}$$

72

Where $\Delta\nu_{B_0}$ is due to the holding field, $\Delta\nu_{SE}$ is the frequency shift contribution from the alkali-^{3}He spin-exchange and $\Delta\nu_{He}$ is due to the magnetic field produced by the polarized ^{3}He. During an EPR measurement the ^{3}He spins are flipped via AFP to reverse their orientation with respect to the holding field. This cancels the effect due to the holding field because when the spins are parallel to $\vec{B}_0$ the small magnetic field they produce subtracts from the holding field yielding $\vec{B}_0 - \vec{B}_{He}$. When they are flipped to anti-parallel they add to the holding field $\vec{B}_0 + \vec{B}_{He}$. Therefore, once the difference between the two states is taken the effect from the holding field is cancelled. This assumes that the holding magnetic field is reasonably stabilized. Eq.(4.30) can then be written in terms of the magnetic field components.

$$\Delta\nu_{EPR} = \frac{d\nu_{EPR}}{dB_0}(\Delta B_{SE} + \Delta B_{He}). \tag{4.31}$$

ΔB_{SE} is the effective magnetic field from the frequent spin exchange collisions between alkali atoms and the ^{3}He atoms. It is given by

$$\Delta B_{SE} = \frac{2K_{He}\Gamma_{SE}\hbar}{g_e\mu_B}K_z. \tag{4.32}$$

K_{He} is the frequency shift parameter defined in Ref.[86], Γ_{SE} is the Rb-He spin exchange rate per Rb atom, g_e is the gyromagnetic ratio of the electron, μ_B is the Bohr magneton, and K_z is the z z component of the ^{3}He nuclear spin. The second term ΔB_{He} is the magnetic field due to the polarized ^{3}He. It is based on the geometry of the helium target cell and is shown as

$$\Delta B_{He} = C\eta_{He}\mu_{He}P_{He}, \tag{4.33}$$

C is a dimensionless number that characterizes the shape of the helium cell and can be calculated using the method of magnetic scalar potential [87] ($C = \frac{8\pi}{3}$ for a sphere), η_{He} is the helium number density, μ_{He} is the ^{3}He magnetic moment, and P_{He} is the ^{3}He polarization. Combining the two magnetic field terms ν_{EPR} can be rewritten as

$$\Delta\nu_{EPR} = \frac{8\pi}{3}\frac{d\nu_{EPR}}{dB_0}\kappa_0\eta_{He}\mu_{He}P_{He}. \tag{4.34}$$

Where κ_0 is a dimensionless constant whose value is proportional to the average alkali electron spin-density at the ^{3}He nucleus. It parameterizes the effective spin exchange field. κ_0 is a large source of error in the polarization measurement as it is not very well known and only more recent measurements [88] have provided its value at the high temperatures used in hybrid SEOP cells. The value of κ_0 still have relative large uncertainties dominated systematic effects. In order to calculate $\frac{d\nu_{EPR}}{dB_0}$ we start with the eigenvalues of the Hamiltonian of the alkali atom in a magnetic field given by the Breit-Rabi formula

$$E_{F=I\pm 1/2, M} = \frac{-A(I+1/2)}{2(2I+1)} - g_I \mu_N B_0 m_F \pm \frac{A(I+1/2)}{2}(1 + \frac{4m_F}{2I+1}x + x^2)^{1/2}.$$
(4.35)

With $x = \frac{\omega}{2\pi A(I+1/2)}$ and $\omega = \frac{2\mu B_0}{\hbar}$ and A is the alkali hyperfine splitting frequency. This can then be written as

$$\frac{d\nu_{EPR}}{dB_0} = \mp \frac{g_I \mu_N}{h} + \frac{g_I \mu_N - g_e \mu_B}{2h(2I+1)} \left[\frac{2m_F + (2I+1)x}{\sqrt{1 + \frac{4m_F}{(2I+1)}x + x^2}} - \frac{2m_F - 2 + (2I+1)x}{\sqrt{1 + \frac{4(m_F-1)}{(2I+1)}x + x^2}} \right].$$
(4.36)

Hence, by measuring the change in frequency ν_{EPR} that occurs when the ^{3}He spins are flipped the polarization can be extracted with

$$P_{He} = \frac{\Delta\nu_{EPR}}{\frac{8\pi}{3}\frac{d\nu_{EPR}}{dB_0}\kappa_0 \eta_{He}\mu_{He}}.$$
(4.37)

4.5.2   EPR measurement procedure and electronics

In order to measure the frequency difference the electronics are setup as shown in Fig(4.21)

An RF coil is placed next to the pumping chamber of the cell, its orientation is perpendicular to both the holding field coils and the transverse field coils. The coil is driven by a function generator (HP E4400B) set to the frequency of the EPR transition between the two states being probed. The sub-states are $m_F = \pm 2$ and $m_F = \pm 1$ or $m_F = \pm 3$ and $m_F = \pm 2$ depending on the isotope of Rb, again

74
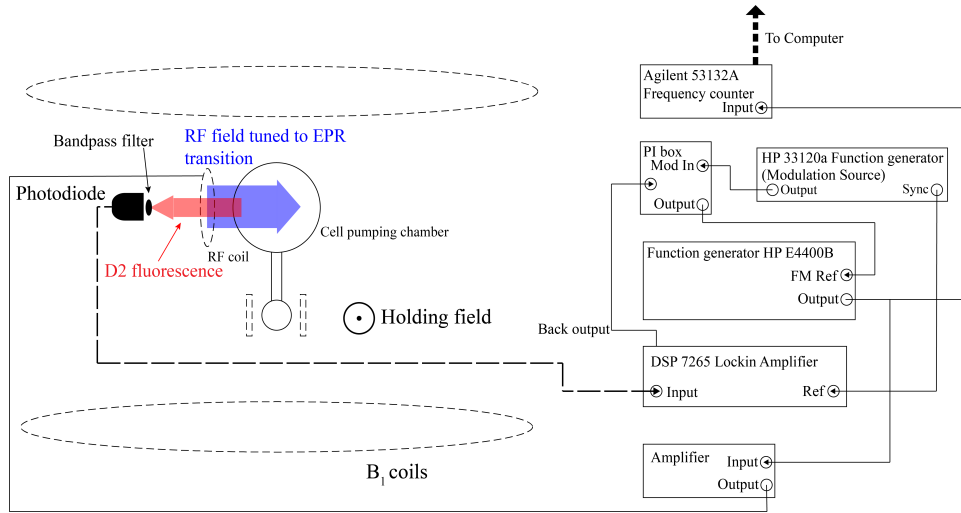
Figure 4.21: Diagram of the electronics setup for measuring EPR

taking Rb polarized by right circularly polarized light as an example the frequency corresponds to the $m_F = 3 \longrightarrow m_F = 2$ transition and is about 10 MHz for a holding field of 21 G. As explained in the theory section the Rb atoms are all polarized into the $m_F = 3$ sub-state of $S_{1/2}$, by applying the RF field the atoms are de-excited into the $m_F = 2$ state. These atoms again absorb the laser light and are excited to the $P_{1/2}$ state. Likewise, if the EPR measurement was performed on K the atoms would depolarize and then re-polarize via spin exchange collisions with Rb thus causing the Rb atoms to depolarize. During the re-polarization of Rb there is an increase in the emission of photons corresponding to the D1 $P_{1/2}$ to $S_{1/2}$ transition at 795 nm. However, due to the thermal mixing between the $P_{1/2}$ and $P_{3/2}$ there is also and increase in photons emitted at the D2 transition $P_{3/2}$ to $S_{1/2}$ at 780 nm. The amount of D1 and D2 fluorescence is almost the same but the D1 photons are in an overwhelming background of D1 laser light. Therefore only the D2 light is detected, this is achieved by placing a narrow bandpass filter in front of the photodiode. In order to modulate the signal, the frequency from the function generator (HP E4400B) is modulated with a separate function generator (HP 33120a). Normally, the voltage from the photodiode would take the form of a Lorentzian as the EPR frequency is scanned across the resonance. If the RF field frequency modulates the signal with

75

an amplitude A at frequency ν_m the resulting signal will be

$$V(\nu) = V(\nu + A\sin(\nu_m t)),\tag{4.38}$$

which can be expanded with a Taylor series

$$V(\nu) = \sin(\nu_m t)\left(A\frac{dV}{d\nu} + ...\right) + \cos(2\nu_m t)\left(-\frac{A^2}{4}\frac{dV^2}{d\nu^2} + ...\right) + ...\tag{4.39}$$

Hence, if the output of the photodiode is sent to a lock-in amplifier (DSP 7265) and measured at the frequency modulation ν_m the resulting signal will be the derivative of a Lorentzian or a dispersion like line shape. An example of the signal seen in the lock-in as the central frequency is scanned is shown in Fig.(4.22)
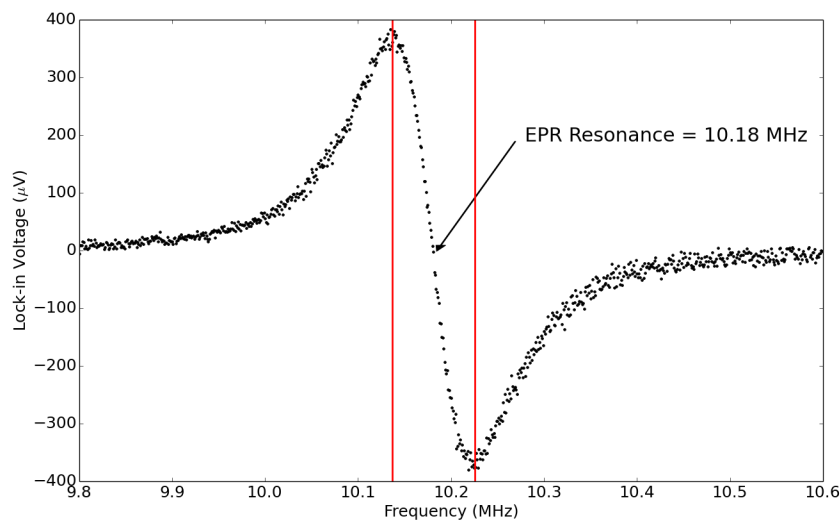
Figure 4.22: Dispersion curve from the lock-in amplifier as the central frequency is scanned across the EPR resonance for ^{85}Rb

It should be mentioned that the signal from the photodiode contains a DC component in addition to the AC component. The RF field does not permeate the entire pumping chamber but there is still D2 fluorescence radiating from other parts due to the optical pumping. However, since this light is not modulated the AC component due to the EPR coil is isolated in the photodiode. The dispersion curve in the lock-in

amplifier can then be used as an error signal to lock the central frequency of the function generator to the EPR transition. In order to do this, the error signal must have a usable shape, mainly the slope of the central region must be large enough so the correction happens quickly and the region must be wide enough that when the frequency is shifted the system does not lock to the other side of the maximum or minimum. Typical settings used to obtain a good line shape are listed in the appendices.

Once a good line shape is obtained the rear output of the lock-in amplifier is sent to a Proportional Integral (PI) feedback circuit which locks the EPR transition. The PI takes the analog signal from the back of the lock-in amplifier and converts it to a frequency correction which is sent back to the RF function generator to be applied to the central frequency. The PI circuit is described in Ref.[89]. The complete setup is the RF coil is powered by a function generator the output of which is also connected to a frequency counter that displays the frequency very accurately. The frequency from the RF function generator is modulated by another function generator, the sync out of the modulation source is the reference for the lock-in amplifier that is connected to the photodiode that measures the D2 light. The analog output of the lock-in amplifier is connected to the PI box which is connected to the RF generator. Once the central frequency is locked to the EPR resonance the output of the frequency counter is read with a computer and the ^{3}He spins are flipped with NMR AFP. Fig.4.21 shows a diagram of the setup. The effective field from the polarized ^{3}He is flipped and the frequency of the EPR transition is shifted by small amount ($\sim$10 kHz). The locked RF field then tracks the shift in frequency and the difference can be seen in the frequency counter. An example is shown in Fig.(4.23)

The difference between the two frequencies is directly proportional to the ^{3}He effective field from the polarization. The polarization can be measured very precisely by measuring this difference. Fig.(4.23) shows multiple spins flips in a row, looking at a single pair of flips in Fig.(4.25) shows that the while the frequency shift is on the order of kHz the frequency can be locked with errors on the level of Hz leading to very precise measurements.

To calculate the ^{3}He polarization the frequency difference obtained from the fre-
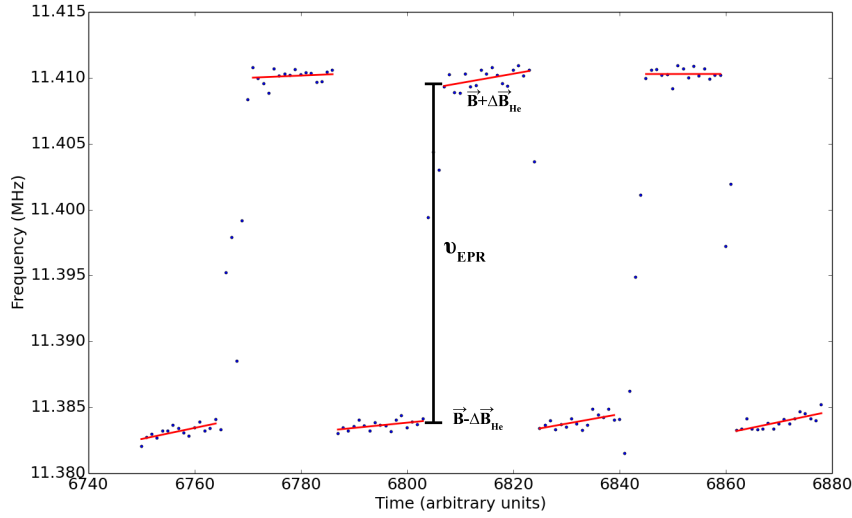
Figure 4.23: Frequency counter output over time as the ^{3}He spins are flipped. The frequency for the EPR transition is different for each orientation of the effective field of the polarized helium. In the figure the fitted lines for the states has a slope due to the optical pumping continuing while the measurement is in progress.
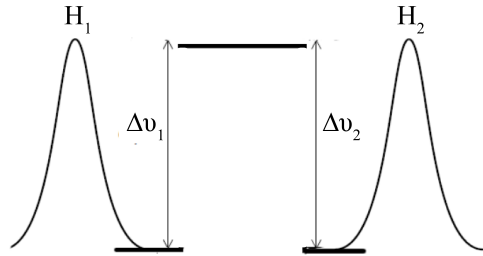
Figure 4.24: Example comparison of the separate peak heights and $\Delta\nu'_{EPR}s$

quency counter is inserted into Eq.(4.37). In practice, the frequency difference is measured for the initial "up" sweep and the following "down" sweep that returns the spins to the original orientation. For each flip an NMR peak is measured at the same time, the height of which is then equivalent to the polarization calculated. The average of the two ν_{EPR}'s and the two peak heights are taken as there is generally a small difference between the up and down sweeps, refer to Fig.4.24.

78
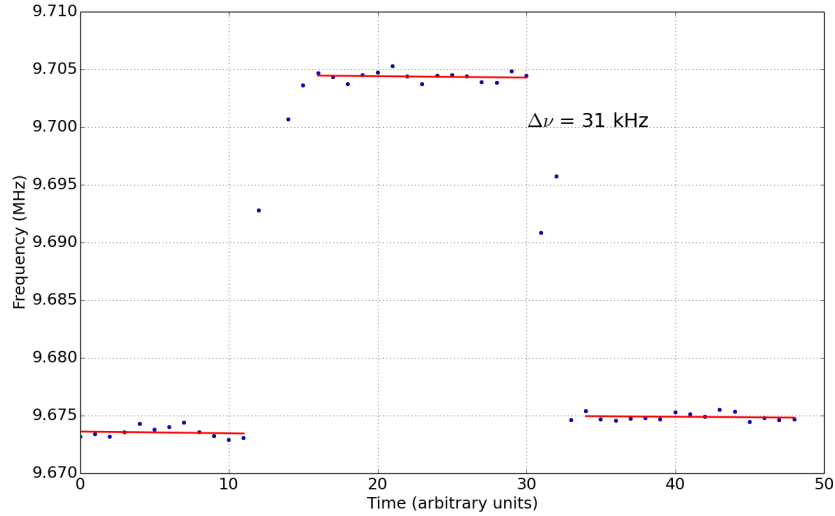
Figure 4.25: A single EPR measurement for the cell Vivian where the spins are flipped and then flipped back to the original orientation. The spread around the fitted line is on the order of 100 Hz.

4.5.3 EPR measurements from the experiment

Several EPR measurements were performed with the hybrid cell Dale in order to calibrate the electronics and test the system. When the cell Vivian was installed several calibration measurements were made again to check the electronics as the cell, although of a similar size and shape, has a different alkali metal ratio $\mathcal{D}$ and a different helium density. While the experiment was running, an EPR measurement was taken at the start of every running cycle to calibrate all of the NMR flips that would occur. After the initial measurement the EPR equipment was generally kept off to avoid the small polarization losses and possible noise while measuring the Faraday rotation. An example EPR spectrum from the frequency counter for Vivian is shown in Fig.(4.25) and the following parameters were used in the polarization calculation.

In addition, there were several sources of error involved in measuring the polarization. Drifts in the holding field account for the spread of the data points in the

Parameter	Value
ν_1	31.00(15) kHz
ν_2	29.04(15) kHz
$\Delta\nu_{EPR}$	30.02(15) kHz
κ_0	6.15(09)+0.00934(14)xT
Temperature	235(05) C
η_{He}	$9.67(27)\text{x}10^{19}cm^{-3}$
μ_{He}	$1.07\text{x}10^{-26}J/T$

Table 4.7: Example parameters for EPR calculation for Vivian

EPR measurement, to account for this the value for for the frequencies are taken from the end points of a fitted line. Where the line is fit to the exact point where the flip was initiated in order to provide an accurate frequency at the moment of the flip. Also, for every flip performed there were some small polarization losses that occurred when the spins transitioned from one state to the other. Usually several flips were performed in a row to measure these AFP losses and correct for them. Finally, there is a polarization gradient from the pumping chamber where the EPR measurement is performed to the target chamber where the NMR measurement is done. Meaning the two polarization measurements will be different be a small amount, the calculation for this correction is dependent on cell temperatures and densities and can be found in Ref.[78]. The typical scale is a 1% difference between the polarization of the two sections. The final polarization extraction from Fig.(4.25) is $54.5 \pm 1.5\%$ for the target chamber.

4.6 ^{3}He cell polarization analysis

With the combined techniques of NMR and EPR the ^{3}He polarization and polarizing rates for a given cell can be measured. Every cell has different polarization parameters due to variation in cell construction and design as well as differences in ^{3}He and alkali densities. The individual setup used to perform SEOP is important too, differences in magnetic fields and ovens and pumping lasers will all have an impact.

The gyromagnetic Faraday effect is directly proportional to the polarization of the medium and because the expected rotations from ^{3}He are so small it is important to understand exactly what the target polarization is and how it evolves under the conditions of the experiment. This section focuses on the polarization characteristics of the two SEOP cells used in the experiment and how they react to the spin modulation. Most of the measurements are NMR peaks calibrated with a single EPR measurement at the beginning to correlate the peak heights with ^{3}He polarization

4.6.1 Maximum polarization and lifetimes

The first cell used in the ^{3}He target setup was the hybrid SEOP cell Dale. The initial run of the magnetic Faraday experiment used this cell with a single pass of the probe laser beam [35]. The cell was polarized with the broadband Coherent lasers during this time and EPR measurements showed the maximum polarization to be $P_{max} = 39 \pm 2\%$. The spin-up time constant was estimated to be $\tau_{up} \sim 10$hrs. After the initial use the narrowband laser was constructed with the expectation these values would improve with the increased optical pumping efficiency. The pump-up curve is shown in Fig.(4.26).

With the new laser the spin-up time was decreased by a few hours but the overall max polarization was only improved by 2%. This is not unexpected however as the Dale has a very high ^{3}He density and a non-optimal alkali density ratio. Thus, the $P_{max} = 41.2\%$ is probably the maximum possible with the cell and limited by it's particular construction. To improve the expected Faraday rotation signal Dale was replaced with the hybrid SEOP cell Vivian which has a design for accommodating multiple probe laser passes. The cells were almost the same except for the flat end windows vs spherical end windows and the different gas densities. Fig.(4.27) is the pump-up curve for Vivian.

Vivian has a $P_{max} = 57.3\%$ and $\tau_{up} = 3.98$hrs. Both quantities are an improvement over Dale and are expected as in general lower helium density results in higher polarization in shorter time spans. The higher polarization is beneficial as it leads to a larger Faraday rotation but the density is less than half so the difference must be

81
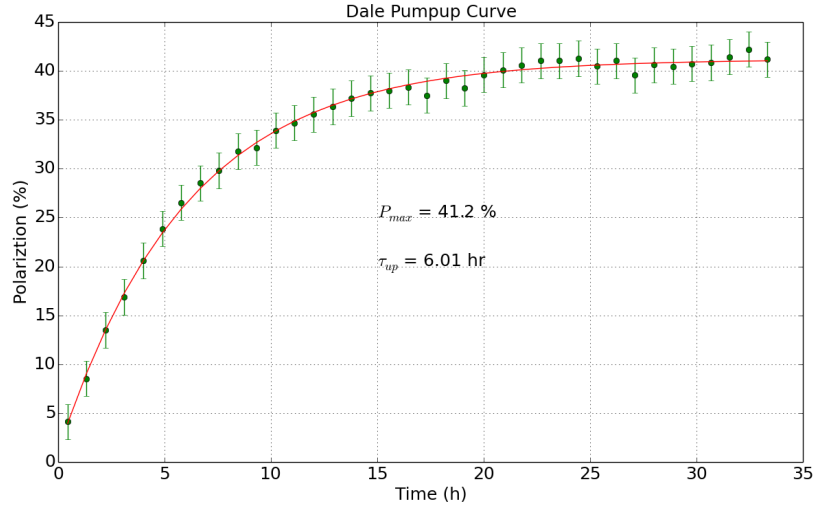
Figure 4.26: Pump-up curve for Dale with max polarization and τ_{up} time constant from an exponential fit

made up in the number of passes of the probe laser beam. Additional measurements of the cells cold (room temperature) spin-down lifetimes are shown in Fig.(4.28) and Fig.(4.29).

4.6.2 Polarization during spin modulation

While the maximum polarization is an important quantity to know about the cell, the more important value in the context of the magnetic Faraday rotation experiment is polarization during spin modulation. In order to modulate the Faraday rotation signal the helium nuclear spins are flipped via NMR. Since every flip incurs some polarization loss due to AFP the polarization will never be at P_{max} but will equilibrate at some value P_{eq} based on the balance of the SEOP pumping rate and the NMR losses. The rate of ^{3}He polarization gain does not change much as the pumping laser is usually run at the same output power and the temperature of the oven is stable, thus P_{eq} is more dependent on the NMR losses and the rate of the spin flipping. The NMR losses were reduced as much as possible so the dominant contribution to P_{eq} is determined by the spin flipping rate. Every time the spins are

82
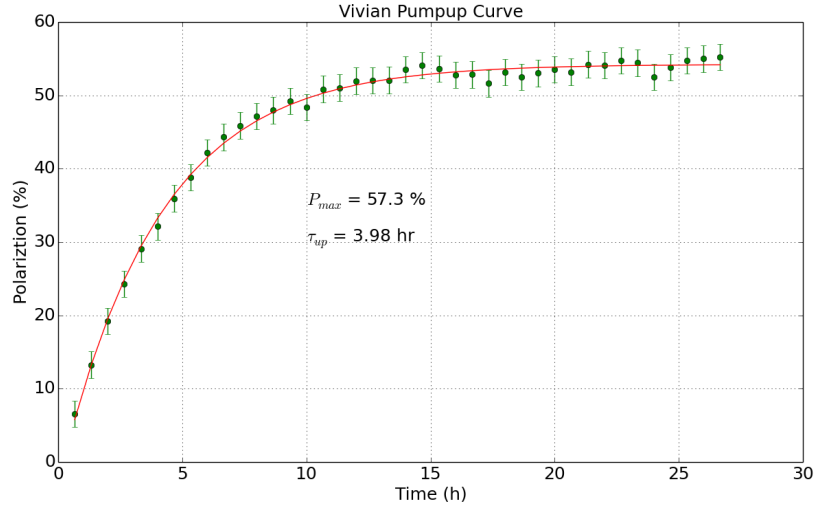
Figure 4.27: Pump-up curve for Vivian with max polarization and τ_{up} time constant from an exponential fit

flipped the quarter-wave plates for the pumping laser are also rotated so the laser is pumping with the correct circular polarization for the state and helium polarization is not lost during the period the spins remain in that state, therefore the ^{3}He are always being polarized for the correct state. The alkali polarization switches very fast compared to the time spent pumping in one state so the losses are minimal from the switch. Attempts were made in Ref.[35] to model the ^{3}He polarization using simple exponentials with the various time constants and loss factors to determine the ideal flipping rate. An example of the model is shown in Fig.(4.30).

Although it is better to go longer in between spin flips because the equilibrium polarization will be larger, the frequency of modulation has to be measured by a lock-in amplifier and this limits the spin flip rates to 1 mHz (1000 s). A flip rate of once every 200 s was chosen to balance measurement time with ^{3}He polarization. Fig.(4.31) shows the ^{3}He polarization of the cell Vivian with spin flips every 200 s after an initial pump-up time. Once the flipping is started the target losses polarization until it reaches a $P_{eq} = 16\%$ and maintains it over several hours. In the figure an NMR peak is measured at every flip to measure the polarization, the separation in
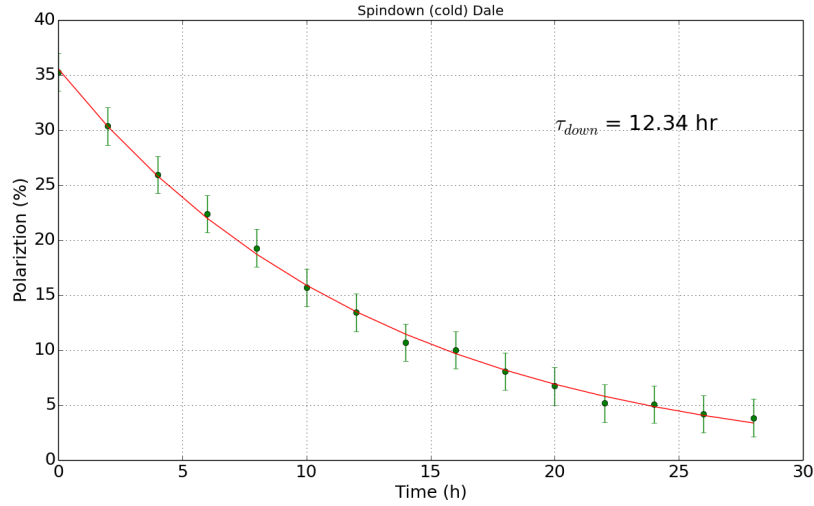
Figure 4.28: Spin-down for Dale

data points is the results of different peak heights for the high energy state and the low energy state. The small fluctuations around the equilibrium are thought to be the result of temperature changes in the pumping chamber of the oven which change the alkali densities. The results match the theory curve in general shape but the P_{eq} is lower than predicted.

Due to the impractical measurement time and increased noise at the lower frequency associated with spin modulation slower than 200 s only faster spin rates were tried. A comparison for two different rates is shown in Fig.(4.32). Flipping once every 50 s reduces the polarization to zero (within errors) so it is not shown or considered practical for the experiment. A flipping rate of once per 100 s produces less than half (7.7%) of the ^{3}He polarization than a flip rate of once per 200 s (17.2%) but still maintains that P_{eq} for long enough to perform a Faraday rotation measurement. These are the primary two flip rates used in the magnetic Faraday rotation experiment, both equilibrium polarizations are large enough to produce a measurable signal and remain stable long to take a measurement.

An example of how the ^{3}He polarization evolves during a typical experiment run measuring the magnetic Faraday rotation is given in Fig.(4.33). The cell is polarized
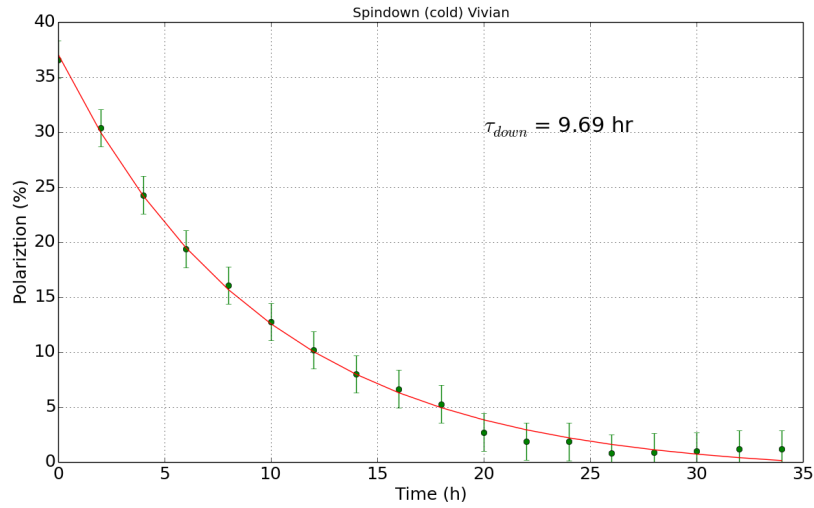
Figure 4.29: Spin-down for Vivian

to an amount larger than the P_{eq} value then the spin flipping is turned on. The Faraday rotation is measured while the polarization is at equilibrium and then the laser is turned off so that ^{3}He polarization drops to zero. A second Faraday rotation is measured here and then the laser is turned back on to re-polarize back to P_{eq} for another measurement. Thus the target can be polarized to a stable value while the helium spins are being modulated. The typical P_{eq} values vary between 15.5% and 17.9% at the extremes with the majority of runs having $P_{eq} = 16.5\%$.
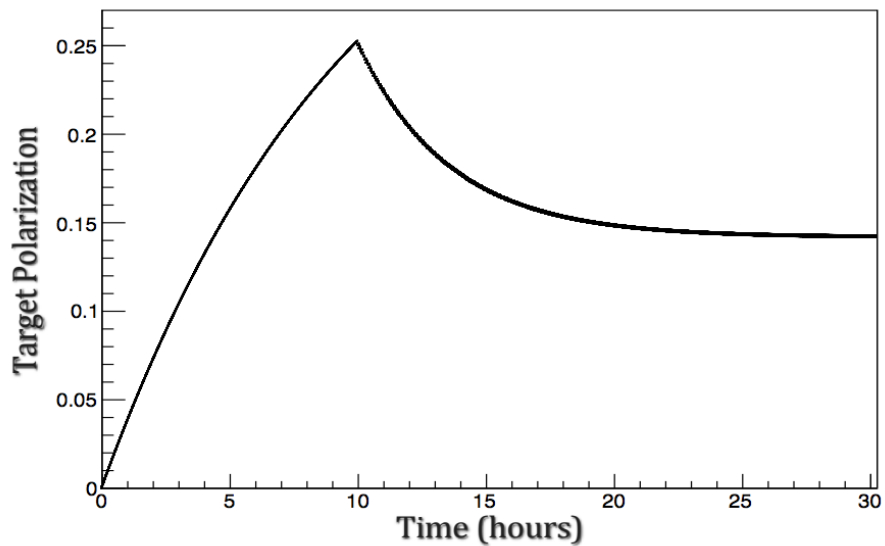
Figure 4.30: Graph of the ^{3}He polarization model with $\tau_{up} = 10hrs$ and AFP losses of 1%. Ref[35]
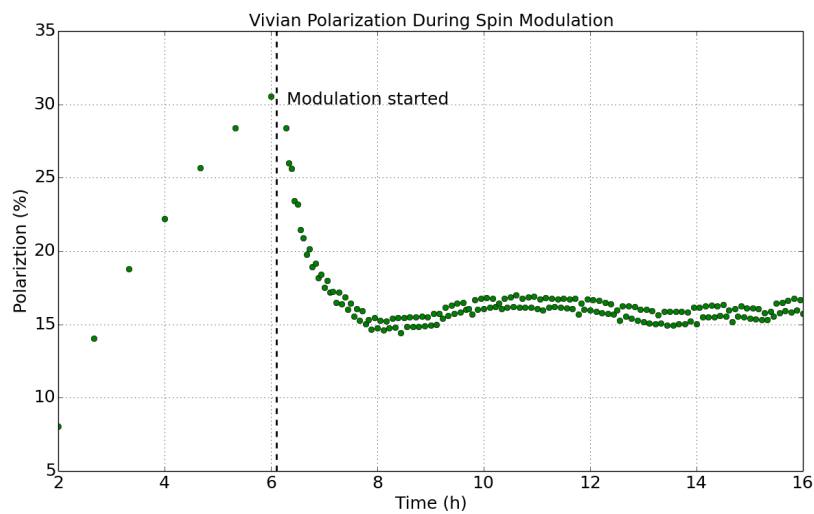
Figure 4.31: ^{3}He polarization of the cell Vivian while the spins are flipped from the low energy state to the high energy state every 200 s with NMR. The AFP losses are 0.9%. The errors (not shown) for the points are $\pm 1.5\%$.

86
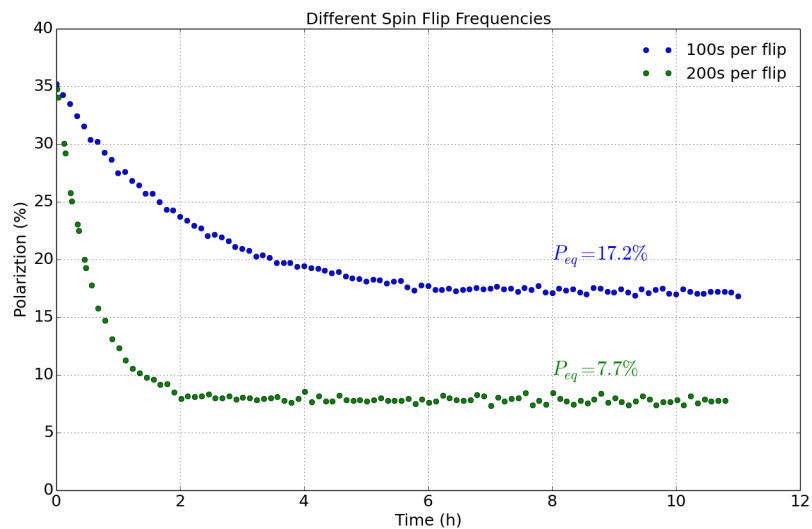
Figure 4.32: ^{3}He polarization of the cell Vivian for different spin flip rates. Only the NMR peaks for one state are shown.
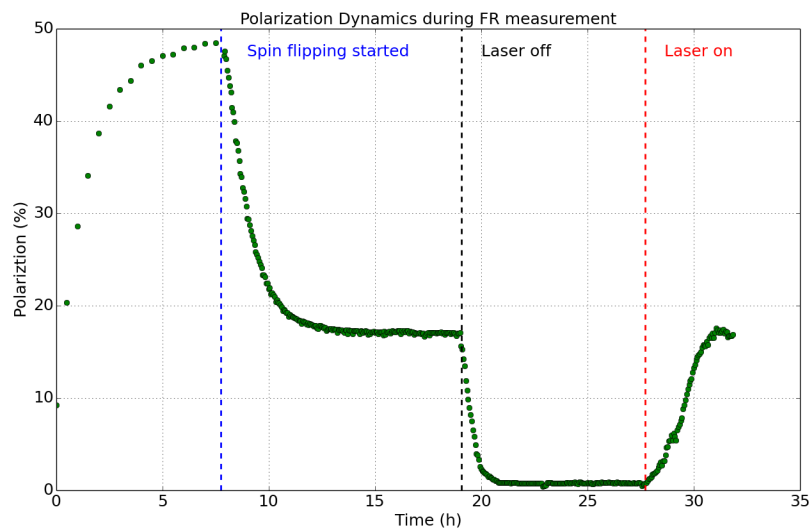
Figure 4.33: ^{3}He polarization of the cell Vivian during a single experimental run measuring the magnetic Faraday rotation.

Chapter 5 Magnetic Faraday Effect of ^{3}He Experiment

The gyromagnetic Faraday effect is a proposed purely magnetic Faraday rotation induced by the magnetization of a medium. It is separate from any electric contribution to the Faraday effect and as such is a unique probe of systems such as a collection of spin-polarized particles. In order to provide a confirmation of the theory, nuclear spin polarized ^{3}He presents a simple test system. ^{3}He has an effective spin 1/2 nucleus and a dense target can achieve high polarization via spin exchange optical pumping. In addition, ^{3}He has paired electrons and a very small Verdet constant so the electric Faraday effect is negligible. Moreover, because the magnetic Faraday effect is proportional to the polarization it can possibly be used to monitor the polarization of SEOP cells which would be useful for experiments at Jefferson Lab where the cells are used for electron scattering. The expected rotation angle, the quantity to be measured, is especially tiny on the order of 10^{-8} rad for an optimized SEOP helium cell used with a multipass cavity. Therefore, to detect such a small rotation a highly sensitive triple modulation polarimetry apparatus is employed that can measure at such a small scale. This chapter describes the measurements of the magnetic Faraday of ^{3}He using the triple modulation method. The changes to the setup, the multipass cavity, the measurement method, the systematics, and the results are all discussed.

5.1 Triple modulation with a ^{3}He target

In the experimental setup, there are three quantities that are normally modulated, the intensity of the probe laser light via optical chopper, the polarization of the light via photoelastic modulator, and the amplitude of the magnetic field. This will not work with ^{3}He as the magnetic Faraday effect is not proportional to the external magnetic field. Thus, the Helmholtz coils used for the field modulation are instead used as a static magnetic holding field to align the ^{3}He nuclear spins. This will line up the nuclear spins with the propagation axis for the probe laser,

Spin modulation freq	^{3}He polarization	Rotation angle
2.5 mHz	16%	35 nrad
5 mHz	7%	15 nrad

Table 5.1: Rotation values at the polarization equilibrium

the spins can then be flipped from parallel to anti-parallel to this axis as the third modulation, Fig.(5.1). The rotation angle will be different for each state and the third lock-in amplifier (Mod lock-in), which is referenced to the frequency of the spin flipping, measures the difference. Thus the third modulation of the method becomes the flipping of the ^{3}He spins. Modulating the spins, and measuring with a lock-in amplifier, isolates the magnetic Faraday effect they generate from other sources of optical rotation in the experiment. The spins are flipped via NMR AFP with an oscillating transverse magnetic field. With pickup coils on the side of the target chamber to detect the changing transverse magnetization components, every flip is also a measure of the ^{3}He polarization. Therefore, the polarization can be monitored during the entire measurement period and the expected rotation signal can be calculated. The magnetic Faraday effect is proportional to the ^{3}He polarization and to keep the the signal size in the measurable range the polarization needs be a large as possible. The maximum polarization for the cell Vivian is 57%, but with the spin modulation the value will be lower because losses occur with every flip. The final equilibrium is given by the rate at which ^{3}He gains polarization via the optical pumping and the rate at which it loses it through spin modulation. Section.(3.6.2) shows that for modulation frequencies of 2.5 mHz and 5 mHz the P_{eq} is either about 16% or 7%. The rates were chosen to maximize the ^{3}He polarization while minimizing measurement time. Table.(5.1) shows the expected rotation angles for the cell Vivian at these frequencies. These frequencies are very low compared to typical experiments and are even close to the operational limits of the lock-in amplifier (1mHz) but studies have shown the triple modulation method is capable of measuring small rotations in this range.

To perform the spin modulation, the function generator that drives the transverse
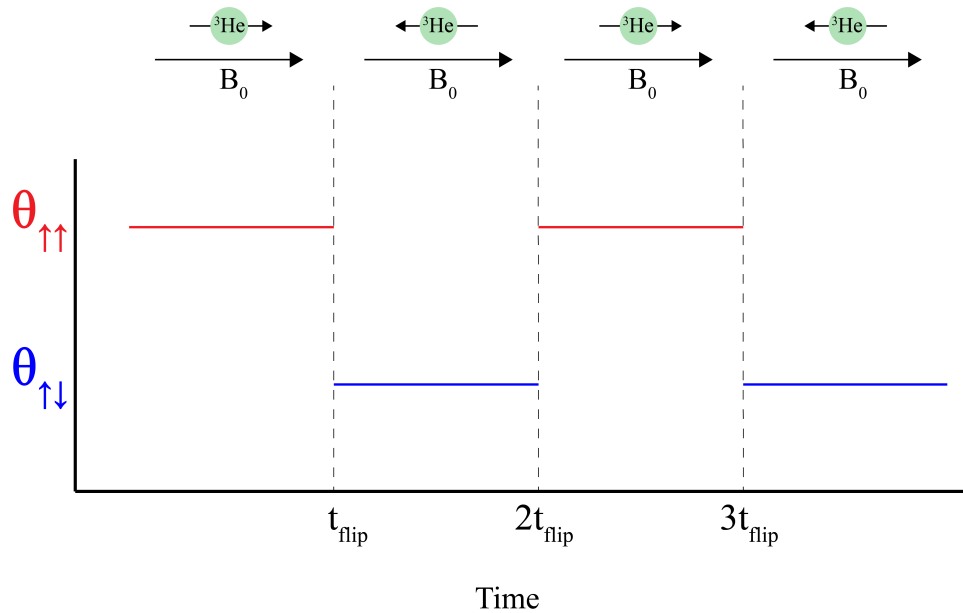
Figure 5.1: The helium spins are flipped from the high energy state to the low energy state as a modulation method. The rotation measured will be different for each state. The period of the modulation is $2t_{flip}$.

coils is controlled with a LabView program on the computer. Frequency sweep NMR flips the spins so the program turns on the coils at some initial frequency and power output, sets the rate at which the frequency sweeps through the ^{3}He resonance, and then initiates the sweep. At the same time the program turns on curve buffer for lock-in amplifier connected to the NMR pickup coils so the resonance peak can be measured. As the frequency of the B_1 field is swept across the resonance, the lock-in amplifier records the voltage in the pick up coils and immediately (0.5s) after the resonance is passed and the spins have be transferred to the opposite state the quarter wave plates that circularly polarize the pumping laser light are rotated. Switching the circular polarization of the pumping light allows continually pumping not matter which state the spins are in. After the sweep is done, the curve buffer is written to a file and the B_1 field is turned off to minimize losses while pumping. The program runs on a global timer, whatever the interval of t_{flip} is the timer makes sure that the flip occurs within 1 millisecond of that time. For example, if the modulation fre-

quency is 2.5 mHz the program makes sure the spins are flipped every (200±0.001) s. A separate program generates a reference frequency TTL at the same time and this is connected to the Mod lock-in amplifier as the reference. Some common equipment settings for the spin modulation are listed below:

Static B_0 magnetic field

- Amplitude: 21.5 G

- He resonance: 69.03 kHz

t_{flip} interval

- 2.5 mHz: 200 s

- 5 mHz: 100 s

Sweep Generator

- Start frequency: 64.00 kHz

- Stop frequency: 74.00 kHz

- Sweep time: 6.66 s

- Sweep rate: 1.5 kHz/s

- Retrace time: 0.02 s

- Amplitude: 300 mV

NMR Lock-in

- Sensitivity: 200 mV

- Time Constant: 80 μs

- AC gain: 10 dB

- Curve buffer length: 100,000 points

- Sampling Frequency: 0.00013 point/s

- Curve buffer mode: Fast

5.2 Lasers and optics

To show that the magnetic Faraday effect is frequency independent two wavelengths are used for the experiment. The first is a HeNe laser from Newport optics that has 35 mW of output power and a beam width of 1.22 mm with a divergence of 0.66 mrad. The wavelength is 632.8 nm and is used for the majority of the calibration measurements and magnetic Faraday effect measurements. The second laser is an external cavity diode laser from Moglabs centered on 405 nm with a nominal linewidth of 200 kHz. The output power is 60 mW with a beam width of 2.5 mm. All of the optics after the laser have an anti-reflective coating with a wavelength range that covers both wavelengths. The exceptions being the Faraday isolators after the lasers and the end windows of the helium cell Vivian which has a coating only for the HeNe laser. To aid with the long distances and multipass cavity the lasers need to traverse, two bi-convex lenses with a focal length of 2 meters and 4 meters are added to the optics train.

5.3 Multipass Cavity

The SEOP cell Vivian was designed with optically flat end windows on the target chamber with the goal that the cell could be used with an optical cavity to reflect the light back and forth through the cell multiple times. Due to the fact that Faraday rotation is cumulative every pass through the medium increases the size of the rotation angle to be measured. The gyromagnetic Faraday effect exhibits this property as well, so the effective rotation due to the ^{3}He in Vivian is enhanced by the number of bounces through the target chamber the probe laser beam can achieve. The expected rotation from a single pass at the maximum measured polarization for Vivian is 120 nrad compared to 201 nrad from the SEOP cell Dale. Therefore a single additional

laser pass through Vivian increases the signal above the maximum possible for Dale and justifies the building of the cell. To reflect the laser multiple times and increase the effective path length an optical cavity, which consist of two mirrors with the medium in between them, has to be implemented. In the ideal situation there would be as many passes as possible. Resonant cavities, such as a Fabry-Pérot, which only allow certain patterns and frequencies provide the highest number of bounces, sometimes up to several hundred thousand. However, such systems are difficult to align and stabilize and the large distance needed between the mirrors for this experiment as well as complications with the cell end windows not being optically flat mean such a cavity is impractical. The next best case is a multipass optical cavity which have far fewer reflections but are more robust against misalignment. Despite the reduction in passes, multipass cavities still provide long effective path lengths and have seen extensive use in spectroscopy and improving atomic magnetometery [90–93]. They have various configurations based on the type and placement of the mirrors used [94–97]. Each of the mirror arrangements have advantages and disadvantages based on their design, in addition to the possible number of laser passes they can have, so only three types of arrangements are considered for this work. The first is a Herriott style cavity with two spherical concave mirrors of equal focal length [95], they typically have the lowest number of reflections and the least dense optical pattern. Common setups have a hole in one of the mirrors to allow the laser beam to enter the cavity, be reflected between the mirrors, and exit through the same hole Fig.(5.2). The second type is similar to a Herriott style but with cylindrical concave mirrors instead of spherical. These cavities have the densest optical patterns and the most number of reflections, which can reach several hundred. The final type is with two mirrors of different focal lengths and possibly different curvatures (one spherical, one cylindrical) called astigmatic mirrors. These can match the number of passes cylindrical mirrors have but have very stringent conditions for getting the beam out of the cavity. For all three configurations the number of passes is determined by the distance between the mirrors, their curvature, and the angle of their curvature axis with respect to each other. The reflections from the laser beam form a spot pattern on the surface of the mirrors that can be used to determine the number of passes

93

and the density of the passes. A theoretical example of the beam spot patterns for the different cavity types is shown in Fig.(5.3). These examples from Ref[97] are calculated using ray tracing.
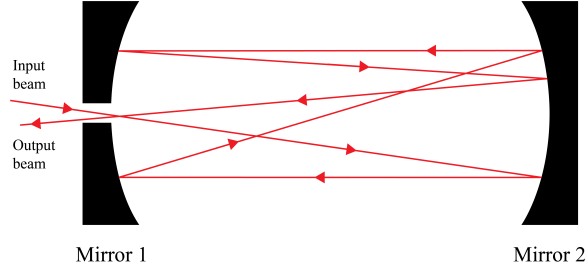
Figure 5.2: Multipass cavity with one aperture. The beam reflects a few times between the mirrors then exits through the same hole.

a) Spherical mirror   b) Cylindrical mirror   c) Astigmatic mirror
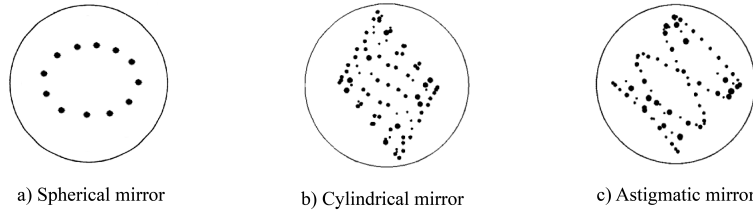
Figure 5.3: Beam spot pattern on the surface of one of the mirrors for a) spherical concave mirrors, b) cylindrical mirrors, c) astigmatic mirrors. Figure adapted from Ref[97].

For the magnetic Faraday experiment there are a few factors that need to be accounted for to pick the best combination of mirrors that can give the highest enhancement to the rotation. The cell end windows, which were originally optically flat, were distorted slightly after being attached to the cell and act like two lenses in between the mirrors. They cause the beam to diverge and reduce the overall number of passes. The mirrors need to be kept as far away from the cell as possible to reduce field gradients that could affect the ^{3}He polarization, thus they need to have a long focal length and form a long cavity. Finally, the laser beam needs to continue from the target region to the shielded analyzing optics so the standard multipass cavity where only one mirror has a hole in it will not work, both mirrors need to have holes

94

so the beam can continue on the same path. Simulations were done, modeling the system of mirrors and cell using the optics package of Geant4 to determine the best parameters for the mirror type, focal length, and positions.

5.3.1 Multipass cavity simulations

The main goal of the simulations was to provide an idea of the best distance to place the mirrors at for the optimum number of passes. A secondary goal was to study and try to find the best way to account for the lensing affects of the end windows. The simulations were done with the optics package of Geant4, a platform designed for the simulation of the passage of particles through matter for particle and nuclear physics applications [98]. In the model, two mirrors were defined and given a reflectivity of 1 for all wavelengths as absorption and transmission are assumed to be very small. Optical photons originate from an area the size of a common HeNe laser beam diameter (1.22 mm) with a Gaussian beam profile and are given a propagation axis towards the mirrors and a divergence of 0.66 mrad. The wavelength of the photons is set to be 632.8 nm. The central axis of this simulated laser beam coincides with the hole in the center of the first mirror so that the photons pass through it and into the cavity. As an initial test, a single photon is created and "fired" towards the cavity mirrors and is observed to reflect back and forth between them. With the appropriate pairs of mirrors the beam spot patterns shown in Fig.(5.3) can be recreated with a single photon. the results are shown in Fig.(5.4) and Fig.(5.5). The two white squares are the mirrors with a surface curvature given by one of the three options. For the two cylindrical mirrors, their axes of curvature are offset by 90° and an additional small angle to create the pattern. A single photon is generated just behind the hole in the first mirror and travels into the cavity and reflects back and forth. The gray lines trace the path of the photon and the green dots are where it hits the mirror surfaces. The photon exits through the same hole as it entered. The focal length for the mirrors is set to 2 m, theoretically the best distance for the mirror separation is the focal length, but the mirrors in the figure are separated by 2.4 m.

95
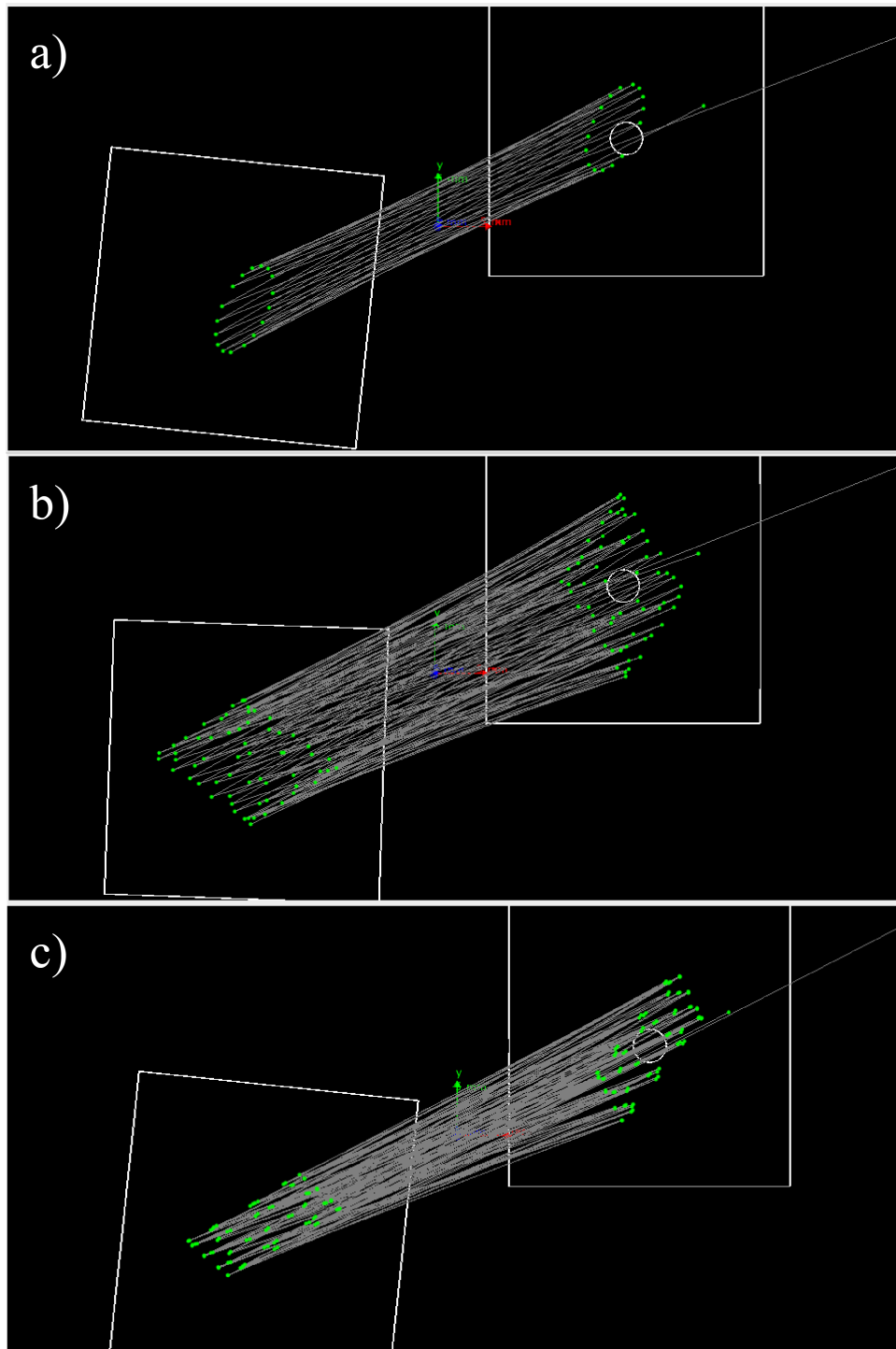
Figure 5.4: Beam spot pattern on the surface the mirrors for a single photon. The gray lines trace the path and the green dots indicate where it interacts with a surface. The photon enters and exits through the same hole in the first mirror. a) two spherical mirrors, b) two cylindrical mirrors, c) one cylindrical, one spherical mirror. All mirrors have a focal length of 2 m and are separated by 2.4 m.
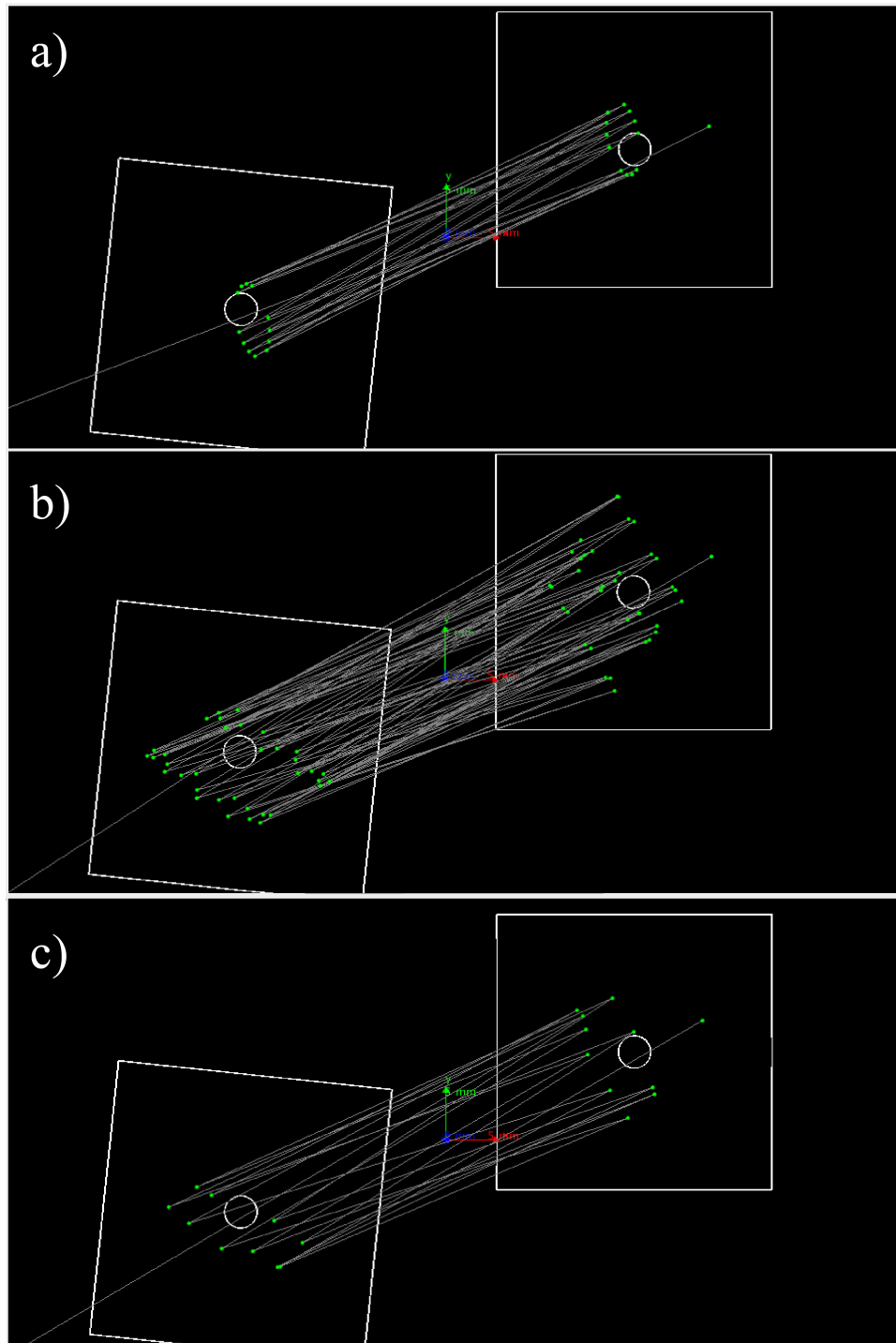
Figure 5.5: Beam spot pattern on the surface the mirrors for a single photon. The photon enters through the first mirror and exits through the second mirror. a) two spherical mirrors, b) two cylindrical mirrors, c) one cylindrical, one spherical mirror. All mirrors have a focal length of 2 m and are separated by 2.4 m.

The simulation works well for a single photon and reproduces real patterns, however the real experiment needs both mirrors to have a hole in them.. The exact same process is repeated for a straight through setup in Fig.(5.4). From the figure it is clear that the overall number of passes will be less for the straight through set up because the photon will exit before completing its pattern. To quantify this, 10,000 photons are generated and directed through the cavity. Because each photon has an individual starting location in the beam diameter and an individual divergence, not every photon path will be the same. Using the data for the interaction points with the mirror surface the number of bounces for a single photon can be counted and the average number for all the photons can be calculated. Due to the wide variety in parameters for astigmatic mirrors and their increased difficulty in combination with a divergent medium such as the helium cell they are not taken into further consideration. Fig.(5.6) is a plot of the average number of bounces for the photons vs the ratio of the mirror separation and the focal length of the mirrors. The focal length of the mirrors used for the data set is 2 m. In order to avoid the photon going through both mirrors without reflecting, the second mirror has a small offset so the center apertures are not on the same axis. The graph shows a peak in the number of bounces when the mirrors are separated by exactly the focal length which is expected from theory. When the second mirror has a hole so that the beam can continue along its original direction the number of bounces goes down, this affects cylindrical mirrors more than spherical mirrors which did not exhibit large losses. This is assumed to be because the spot patterns for spherical mirrors are not as dense and thus have less probability the photon will exit.

Cylindrical mirrors look like the better option from the graph as with the losses from the addition of a second hole they still provide a larger number of laser passes.

The next step is to add a volume of helium encased in glass in between the two mirrors. In the simulation, a cylinder made of glass with a refractive index equal to that of Corning 1723, the material the cell windows are constructed from, is added with a volume of He inside. The photons are very low energy ($\sim$2 eV) and do not interact with the He so the only affect it has is due to its tiny difference in index of refraction from air. To estimate the effect of the windows not being optically flat a
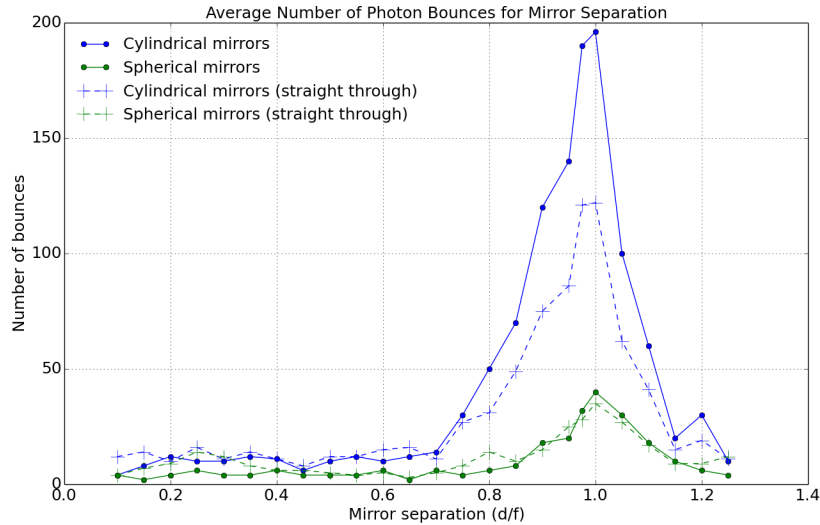
Figure 5.6: Plot of the average number of bounces for 10,000 photons vs. the ratio of the distance between the mirrors and their focal length. The focal length of the mirrors for the data set is 200 cm. The data is plotted for a cavity with one aperture where the beam reflects back towards the origin and for a cavity with two apertures where the beam continues along its original direction.

small curvature was added to each quadrant of the window to mimic the lensing. The main effect then is the photons will be refracted by cell windows and diverge from their original trajectories. Fig.(5.8) shows the path a single photon with the same initial conditions for windows that are flat and windows that are not. For the flat windows, the pattern is very similar to when there is nothing in between the mirrors. When the curvature is added the path of the photon is altered and it no longer makes it through the aperture of the second mirror. To extract useful information from this setup, a detector volume is added after the second mirror that can count the photon if it hits. With a large number of photons, statistics can then be recorded on how many photons make it to the detector, along with the number of bounces, for a given mirror focal length. Fig.(5.7) shows a plot for a few mirror focal lengths. For each mirror focal length, which is equal to the distance between the mirrors, and configuration 10,000 photons were again used for statistics. The trends in the data

show that mirrors that are further apart and have a greater distance from the cell windows will have less photons make it into the detector as more are lost outside the cavity. Cylindrical mirrors are worse in this regard as the volume the photon traverses in the cavity is usually larger compared to spherical mirrors and this leads to scattering at more severe angles from the windows, causing more losses. Spherical mirrors tend to keep the photons focused towards a single point which is beneficial to prevent scattering, and consequently the number of passes is not affected as much.
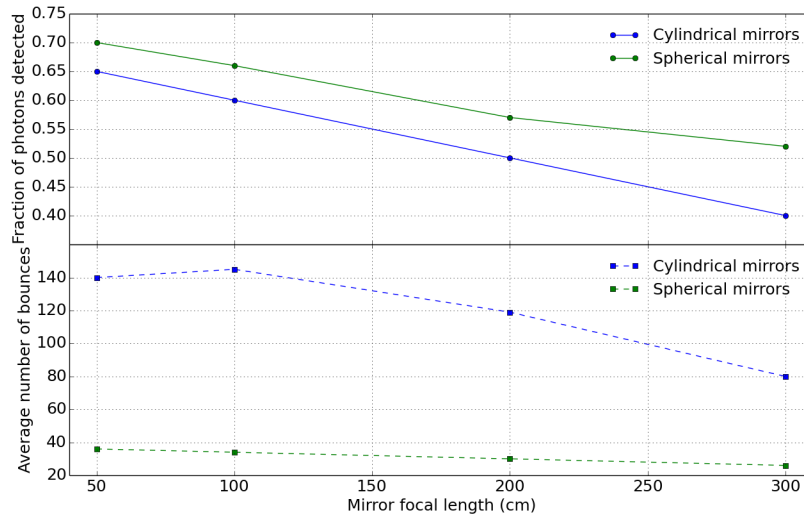
Figure 5.7: Fraction of the initial photons measured in the detector, and the average number of bounces for those photons, in a cavity setup with cylindrical and spherical mirrors of different focal lengths with a model of the ^{3}He target chamber in between. The separation of the mirrors is equal to their focal length.

For the real setup, a laser has to be used and this will behave differently from individual photons. Even large numbers of photons in the simulation cannot compare to what will happen with a real laser beam. Regardless, Geant4 has essentially been used as a ray tracing program and some useful results can be extracted from the simulations. Having the ^{3}He target chamber in between the cavity mirrors will influence how the cavity operates. Cylindrical mirrors, because they essentially only focus along one axis at a time, will not be able to achieve the high number of passes

they normally do and will be greatly affected the further they are placed from the cell. Therefore, this suggests spherical mirrors are the better option even with the smaller number of laser passes they will accumulate. They will focus the beam better and have the ability to be placed further from target chamber which is necessary for the real experiment.
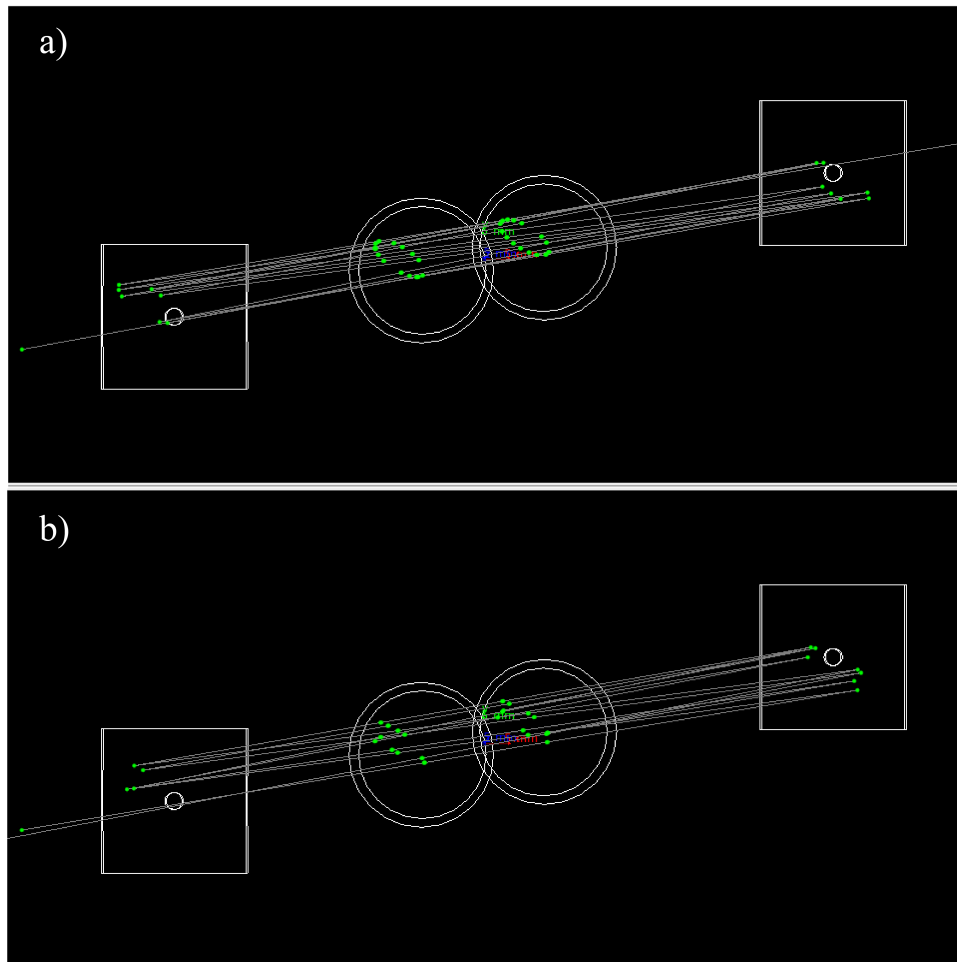
Figure 5.8: a) Path of photon with helium cell in-between the cavity mirrors where the end windows are optically flat. b) Path of photon with helium cell in-between the cavity mirrors where the end windows act like lenses. The mirrors have a spherical curvature and a focal length of 200 cm.

5.3.2 Cavity mirrors

To confirm the results of the simulations, a pair of cylindrical and spherical test mirrors were purchased from Thorlabs. The results were even more dramatic than the simulations as the cylindrical mirrors proved unusable with the SEOP cell target chamber. Spherical concave mirrors focus the laser beam in both directions and counteract the lensing effect of the cell end windows better. The number of laser passes they can achieve is not affected as much by the addition of a second hole in the other mirror or by the distance between the mirrors. Thus, for the experiment a Herriott style cavity with spherical concave mirrors is implemented. The mirrors are spherical concave with a radius of curvature of 3 m and a focal length of 1.5 m. They have a 1 inch diameter that matches the diameter of the cell windows so the laser is most likely to stay within the volume of the target chamber. The hole in the mirrors is off the center axis, this allows the mirrors to be rotated to select the final laser pass rather than adjusting the positions. The mirrors were made by Fivenine optics and have a special high reflectivity (99.9992%) coating. There are two sets of mirrors each with a coating for the two wavelengths (633 and 405 nm) used in the magnetic Faraday experiment. The high reflectivity is needed so that intensity losses can be minimized. The windows have an AR coating as well but only on one side as a coating on the inside could potentially affect the ^{3}He polarization. Hence, there will be intensity losses with every pass. Fig.(5.9) shows the beam spot pattern on the surface of one mirror for a HeNe laser that reflects through the first mirror.

The spots where the laser hits the mirror form a nice elliptical pattern identical to the theory and simulations. Counting the number of spots yields the number of passes as it is exactly half the number of passes for a back reflecting setup and half the number minus one for a straight through setup. The number of reflections increases until the mirrors are separated by the focal length and the maximum for the mirrors is 42 or 43 with nothing in between.

In the experimental setup the mirrors need to be placed as far away from the He target as possible to avoid field gradients and ideally as far out of the B_0 holding magnetic field as possible. Due to these constraints and the need to have as many

a) 14 passes	b) 18 passes	c) 26 passes	d) 42 passes
d = 1.20 m	d = 1.33 m	d = 1.40 m	d = 1.48 m
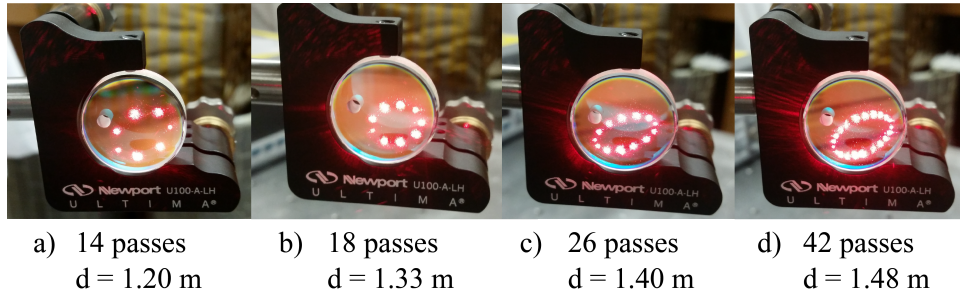
Figure 5.9: Beam spot pattern for the cavity mirrors for various distances with nothing in between them. The mirrors have a focal length of 1.5 m so the maximum number of passes for the mirror size and curvature is 42/43 passes.

laser passes as possible the separation for the mirrors is 2.2 m centered on the target chamber of the cell. Each mirror sits in a precision kinematic stage on a platform that is vibrationally damped with sand and other padding Fig.(5.10). The platforms are separate from the ^{3}He target platform but are still inside the magnetic field, therefore additional Helmholtz coils are placed around each mirror to cancel the effect of the holding magnetic field. The mirrors are centered on the target chamber which itself is centered near the axis of the B_0 coils, thus the compensation coils lie along this axis as well. Careful alignment can reduce the magnetic field at the surface of the mirrors to the 10-20 mG level where tests confirm any Faraday or optical rotation noise from the mirrors is below detection threshold.

The alignment of the cavity mirrors determines how many times the probe laser will pass through the cell and thus the increase in the rotation angle to be measured. On the platform, the mirrors are on translation stages for movement in the laboratory $\hat{y}$ direction and these sit on rails for translation along the axis ($\hat{z}$) of the probe laser. One of the parameters that determines the number of passes is the distance between the mirrors, in the ideal situation they are one focal length apart. Intensity losses and beam divergence caused by the helium cell prevent the maximum number of passes so they are moved further out. For 633 nm, approximately 20% of the laser power is lost per pass while for 405 nm it is 40%. The fact that the probe laser needs to continue along roughly the same axis after the cavity means the mirrors never have their center axes lined up with one another. Through significant trial and
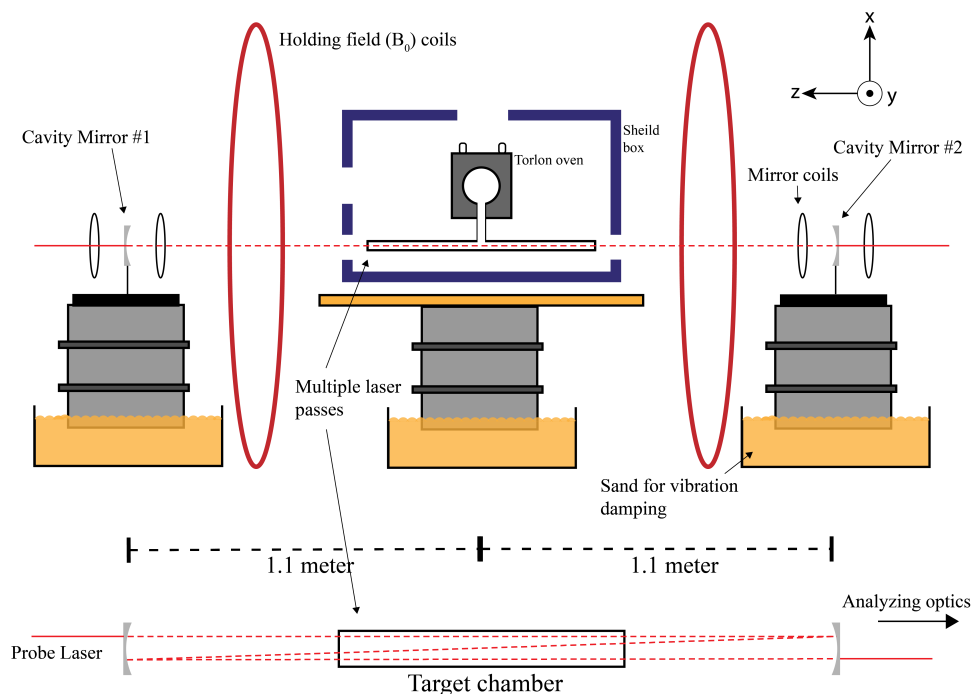
Figure 5.10: Setup for the multipass cavity with the ^{3}He SEOP cell Vivian. The mirrors are on their own platforms that are separate from the target and vibration damped. The coils around each mirror cancel the magnetic field from the B_0 coils. After the probe laser passes through the cell multiple times it continues on to the analyzing optics.

error, the mirror positions and angles are adjusted until a large number of bounces is obtained. Then, the second mirror is rotated until the aperture lines up with the final laser pass. With the typical alignment, neighboring beam spots on the pattern do not correspond to sequential passes. An example of the beam spot correlation with reflection number is given in Fig.(5.11). Minor adjustments are made to the mirror parameters until the final laser pass makes it through the analyzing optics into the detector. A more detailed description of alignment can be found in Appendix.()

In practice, the maximum number of laser passes with the helium cell in and the laser making it back into the detector is 19. When the forced air oven that the pumping chamber is located in is turned on the entire SEOP cell vibrates, these tiny motions cause the beam pattern to vibrate. These shifts lead to the laser scrapping
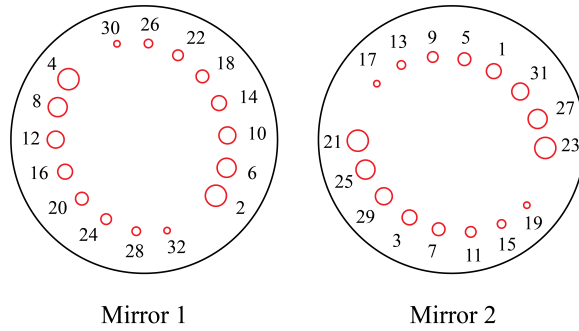
Figure 5.11: Example beam spot on the surface of the mirror correlated with pass number. Sequential passes hit the mirrors with a near 90° offset. The angular separation of sequential beam spots changes with mirror separation and relative orientations with respect to each other.

Table 5.2: Expected rotation angle from the magnetic Faraday effect for a given number of passes through the cell and equilibrium polarization

Laser	Number of passes	P_{eq}	Rotation
HeNe 633nm	13	16%	455 nrad
		7%	199 nrad
External Cavity 405nm	9	16%	315 nrad
		7%	138 nrad

along the aperture in the second mirror instead of passing through unobstructed and introduce errors in the rotation measurement. This effect is worse the more times the probe beam passes through the cell, this again reduces the passes. Under experimental conditions the maximum number of bounces is 13 for the 633 nm wavelength laser. The 405 nm laser has an elliptical beam profile with a larger divergence that is more difficult to compensate for and so has an even lower number at 9 passes. Fig.(5.12) shows the 13 passes beam spot pattern from the HeNe laser on the surface of the cell window and one of the mirrors.

Figure 5.12: 13 pass beam spot pattern on the surface of the end window for Vivian and on the surface on the mirror.

5.3.3   Mirror cavity systematics

To confirm that Faraday rotation is indeed cumulative and that the experimental setup measures this without unexpected errors. The rotation angle is measured for a glass sample with a well known Verdet constant and then the mirrors are placed in and the rotation angle is again measured for multiple passes. The glass sample is a 1 inch diameter piece made from Corning 1723 that is the same as the SEOP cell end windows, however, it does not have an anti-reflective coating like the window does. Several similar pieces were used for pressure testing the glass. With the SEOP cell removed the glass sample is placed on the target table and the rotation is measured for a field amplitude of 5.91 G and a various number of passes. The plot in Fig.(5.13) shows the rotation measurements, with a correction for the Faraday from air subtracted, compare well with the expected value.

As an additional test, the triple modulation setup is operated under the same experimental parameters as the measurement of the magnetic Faraday effect of ^{3}He but without the SEOP cell target. Essentially, the stabilized static holding field and the oscillating transverse magnetic field are on and all of the equipment is running save for the oven for the pumping chamber. With 17 passes through the mirror cavity, the measured Faraday rotation for the bare setup is 0.88±0.53 nrad.
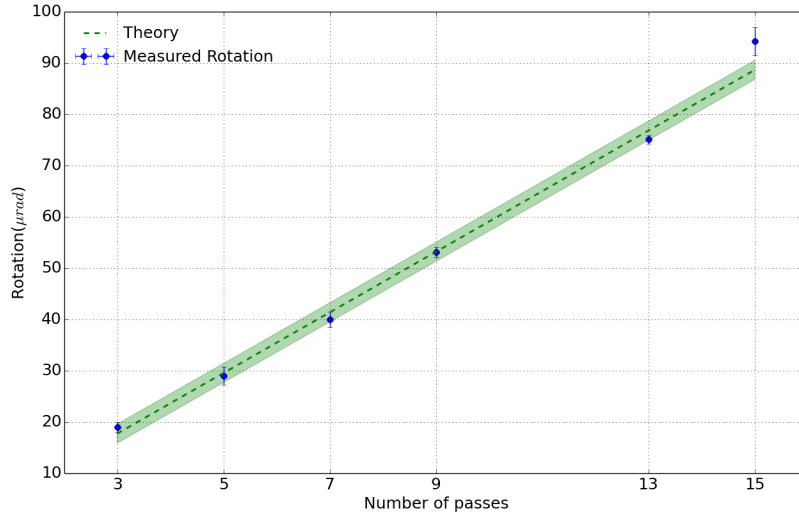
Figure 5.13: Faraday rotation for a single Corning 1723 0.3175 cm thick glass sample in a field of 5.91 G. The rotation is plotted for a varying number of laser passes and compared with the theory calculation. Only odd numbers of passes can make it back into the analyzing optics.

5.4 Depolarization due to cell windows.

The ideal setup to measure Faraday rotation has nothing in between the polarizing optics and the analyzing optics but the sample being measured. This gets rid of any possible systematic errors due to other media. For this experiment, the signal is the magnetically induced Faraday rotation from ^{3}He but the helium is contained inside a glass cell that cannot be removed. The rotation from the nuclear spins is isolated from other sources in the experiment because of the modulation and lock-in amplifier but there is slight depolarization of the linearly polarized laser light due to the glass end windows of the cell. The s and p polarization components of light incident on a boundary between two different indices of refraction have different reflection and transmission coefficients. The coefficients as shown in Eq.(5.1) are based upon the angle of incidence and the value of the refraction indices. Fig.(5.14) shows the transmission coefficients for an air-Corning 1723 boundary versus the angle

of incidence, Corning 1723 has a refractive index of 1.55 Ref[99]. The amplitude of the electric field component after the boundary is given by the initial amplitude times the transmission coefficient $E^T_{s,p} = t_{s,p}E^I_{s,p}$. The difference in coefficients will lead to linearly polarized light undergoing a rotation due to the changing amplitudes, or in the most general case being converted to elliptically polarized light. For small angles the coefficients are nearly the same, differing by only 0.01% at 2 degrees angle of incidence. To check that there are no additional errors associated with the end windows being at some angle with respect to the laser beam and the magnetic field the depolarization is measured from a glass sample.

$$
\begin{aligned}
t_s &= \frac{2n_1 \cos\theta_i}{n_1 \cos\theta_i + n_2 \cos\theta_t} \\
t_p &= \frac{2n_1 \cos\theta_i}{n_1 \cos\theta_t + n_2 \cos\theta_i}.
\end{aligned}
\tag{5.1}
$$
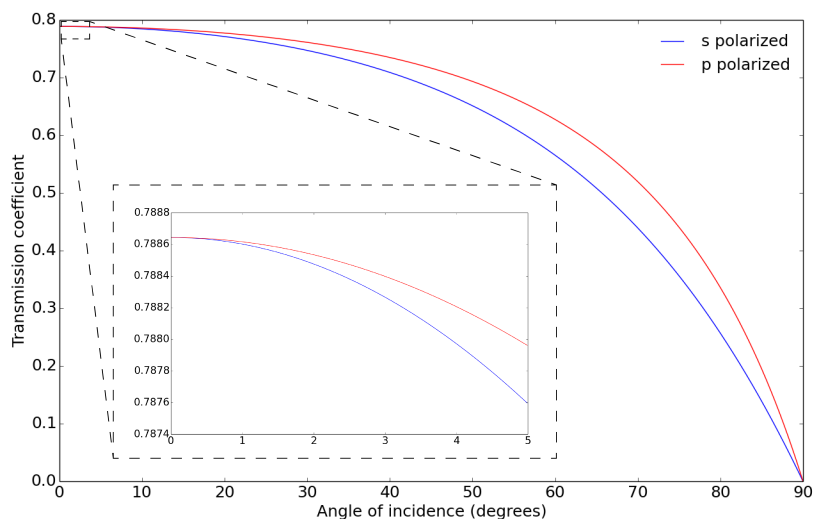
Figure 5.14: The transmission coefficients for an air-Corning 1723 boundary.

The glass samples are spare Corning 1723 windows of the same size as the windows on the cell. The Faraday rotation is measured for two of these windows, each window has a slightly different rotation due to small differences in thicknesses. The combined

Faraday rotation is then measured with both in the magnetic field. This is a partial confirmation that having separate sources of Faraday rotation in the field add up as they are supposed to. One window is rotated until it forms an angle with the laser and the measured Faraday rotation with the triple modulation method is compared to the value when there is no angle of incidence. The depolarization is defined as the ratio of the difference between the normal value and angle of incidence value and the normal value. Fig.(5.15) shows the results for an initial s polarized and p polarized wave. The value is larger than expected from the Fresnel equations, but at small incident angles below 5° it is still exceedingly small. The rotation values are corrected for the change in thickness of the window when it is tilted at an angle.
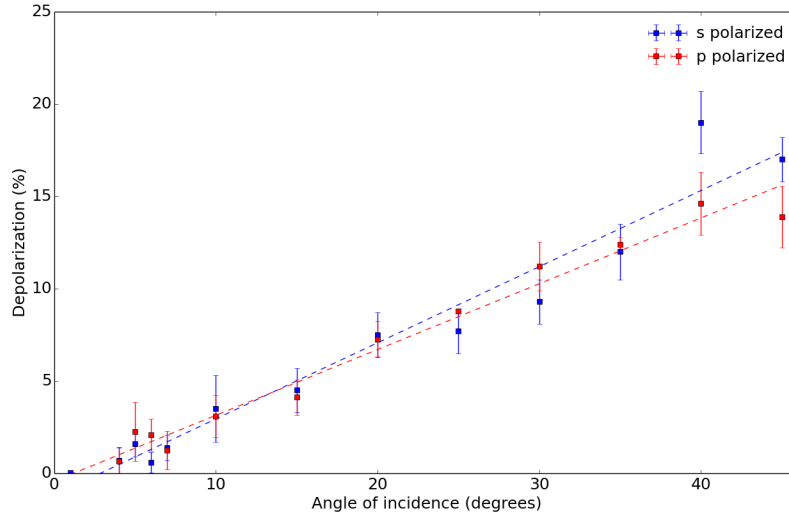
Figure 5.15: The depolarization measured for the Corning 1723 window samples as a function of angle of incidence.

The depolarization effect could result in a systematic error for the magnetic Faraday effect measurement because the cell windows are in the path of the probe laser. The windows of the SEOP cell Vivian are not perfectly parallel with each other, rather, from the construction they sit at some angle. When placed in the target setup the position of the cell is adjusted so the angle that each window makes with

the laser path is minimized. The angle can be measured by looking at the reflection of the probe laser from the surface of the windows, Fig.(5.16). At worst the effect is an offset that needs to be corrected for but since both windows are less than 2° from normal to the laser the error from depolarization is near zero. The angles shown in Fig.(5.16) represent the maximum error as subsequent laser passes from the cavity mirrors have even smaller offsets.
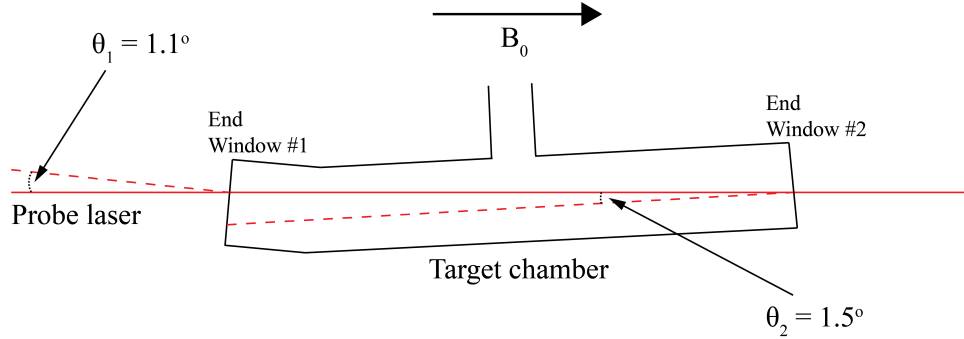
Figure 5.16: Cell position with respect to the probe laser with exaggerated angles and dimensions. The probe laser is aligned along the static magnetic field axis and the angle the windows form with the probe laser can be determined from the lasers reflection from each window.

5.5   The Experiment

In this dissertation, the experimental setup for measuring the magnetic Faraday effect from ^{3}He has been described. The method for measuring small Faraday rotations using a triple modulation technique, polarizing a ^{3}He target with a spin exchange optical pumping scheme, modulating the nuclear spins to isolate the effect, and increasing the signal size with a multipass cavity have all been discussed. These various programs are combined to make the measurements that will be presented in this section.

For the first experimental runs, the 632.8 nm HeNe laser was used. The first step is to align the multipass cavity. Initially the oven for the pumping chamber is off so the laser can be aligned without the vibrations from the air flow. The laser is directed
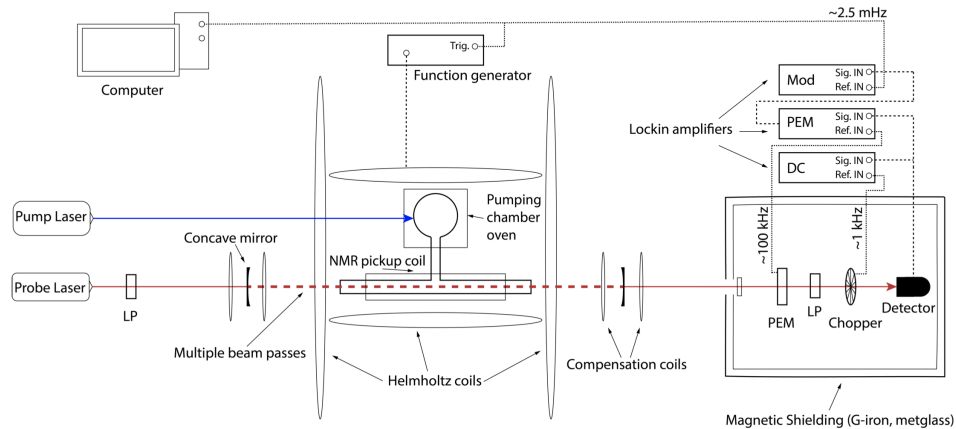
Figure 5.17: Schematic diagram of the full experimental setup used to measure the magnetic Faraday effect from polairzed ^{3}He

into the correct position and the cavity mirrors are added. The first mirror is added into the path of the laser essentially locking its position in the x-y plane, the second mirror is added and small translation and angular adjustments are made until a 13 pass beam spot pattern is visible. Once there are thirteen passes, the second mirror is rotated until the hole lines up with the final pass and small adjustments are made until the beam passes through the analyzing optics and into the detector. The oven is then turned on, while the temperature is rising to the set point the small shifts in the laser path caused by the expanding and contracting materials are corrected for. When the setup is stable, the pumping laser is turned on and the ^{3}He begins to polarize. The target is polarized to near maximum over several hours in addition to higher polarization this allows more time for the oven temperature, magnetic fields, and laser to stabilize. When the helium has reached a high polarization an EPR calibration measurement is performed and then the spin flipping is started via computer. The first runs use a modulation at 2.5 mHz meaning the spins are flipped every 200 s. The curve buffer of the lock-in amplifier connected to the NMR pickup coils is read every 1000 s providing a measure of the ^{3}He polarization. At the same time that the spin flipping is started, the data collection from the three lock-in amplifiers that measure the Faraday rotation is started as well. The voltages from

the lock-in amplifier are read continuously and written to a file. The time constants for the DC and Mod lock-in amplifiers are set to 1000 s due to the small rotation value, thus only one data point every 1000 s is used to calculate the Faraday rotation and the statistical errors. To collect enough data points the experiment is run with spin flipping for 12 hours. Over the entire measurement period most cycles have an average polarization of 16% with up to a few hours in the beginning having higher polarization as it decays to the equilibrium value. Normally this data is not used as the lock-in amplifiers take 5 time constants to stabilize. Once sufficient time has passed the data collection from the lock-in amplifiers is stopped and the pumping laser is turned off or tuned away from the Rb D1 resonance. The ^{3}He polarization then decays to near zero value with the spin flipping still running. The data collection for the Faraday lock-ins is then turned back on and the Faraday rotation is measured for 12 hours while the experiment runs but there is no ^{3}He polarization. Thus there are two data sets where all the experimental parameters are the same except for the polarization, meaning for one data set there should be a Faraday rotation from the helium and the other should measure a noise floor or minimum rotation when there is no real signal, Fig.(5.18). Comparison of the two data sets should show a difference if the gyromagnetic Faraday rotation is there even if it differs from the theoretical prediction. One 24 hour period contains one data set each of a polarized and non-polarized cycle. After the non-polarized run the laser can be turned back on or retuned and the target will re-polarize back to the equilibrium value and another complete cycle can be measured. Several data sets can be taken in this manner as long as everything remains stable. Over the course of a few months many data sets were collected this way. Some were unusable due to excessive noise in the rotation measurements or other equipment failures. The nine best data points are listed in Table.(5.3) and plotted versus the expected rotation value per pass in Fig.(5.19). The error bars for the data points were determined according to $\sigma/\sqrt{n}$ where σ is the standard deviation of the data set and n the number of points. With a time constant of 1000 s there are between 40 and 50 data points per measurement period. The weighted value of all the polarized data points and all the non-polarized data points are plotted along with the expected rotation value from the theory. Not only

112

do the measurements on a polarized target not match the expected value but there is no discernible difference between polarized/non-polarized target indicating that the effect is not there. The rotations have errors nearly equal to the size of the mean suggesting that a noise floor is being measured which is well below were the signal is supposed to be.
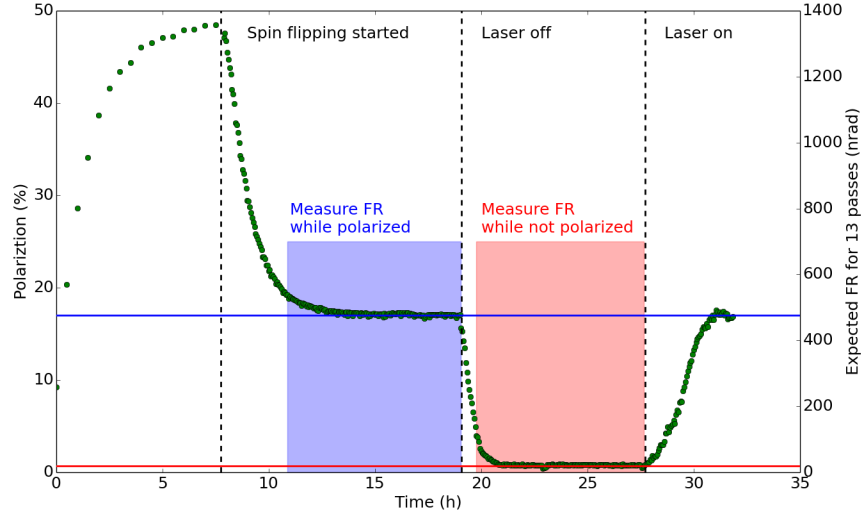
Figure 5.18: Helium polarization and corresponding theoretical Faraday Rotation (FR) during a single measurement cycle. The data collection for the triple modulation lock-ins happens when the polarization is at the equilibrium value and near zero. The expected rotation is calculated for 13 laser passes in the multipass cavity.

The same procedure was repeated with the 405 nm external cavity diode laser. Due to the laser having a more elliptical beam profile and a wider divergence, as well as the cell not having an anti-reflective coating for the wavelength, only 9 passes are possible when the multipass cavity is aligned. With all other experimental parameters the same, several measurement cycles were completed and the nine best data points are listed in Table.(5.4) and shown in Fig.(5.20).

The data for the 405 nm wavelength shows the same result, no difference between a polarized and non-polarized target and both measurements well below the expected value. The error bars for this wavelength are larger and in general data taken with

113

Run number	^{3}He P_{eq}(%)	Polarized (nrad)	Non-Polarized (nrad)
1	16.2	76(30)	58(33)
2	17.0	101(40)	115(43)
3	16.8	84(38)	190(175)
4	17.2	121(110)	105(52)
5	16.5	117(63)	120(100)
6	16.5	75(51)	102(51)
7	16.6	130(73)	95(73)
8	16.4	56(25)	73(50)
9	17.3	109(72)	106(72)

Table 5.3: Magnetic Faraday rotation measurements for a polarized and non-polarized ^{3}He target. Measured at a wavelength of 633 nm.

Run number	^{3}He P_{eq}(%)	Polarized (nrad)	Non-Polarized (nrad)
1	16.9	140(90)	118(80)
2	17.1	70(40)	115(88)
3	16.8	106(44)	190(175)
4	17.3	243(165)	105(52)
5	17.0	116(99)	134(90)
6	17.2	100(44)	150(76)
7	16.9	108(102)	161(184)
8	16.9	147(167)	113(105)
9	17.4	99(100)	97(89)

Table 5.4: Magnetic Faraday rotation measurements for a polarized and non-polarized ^{3}He target. Measured at a wavelength of 405 nm.

this laser has more noise. This is thought to be the interaction of the PEM with this wavelength, although intensity noise in the laser is another possibility. Table.(5.5) summarizes the weighted averages presented in the figures, there is no effect at the scale of 6-10 nrad.
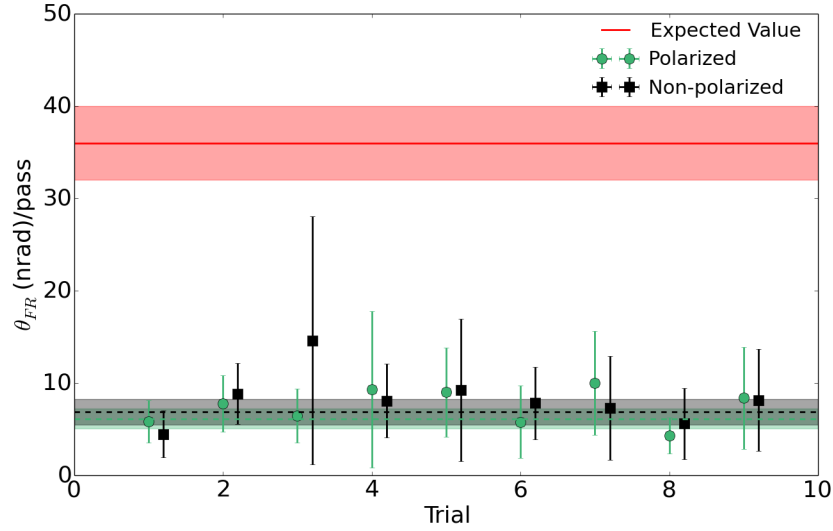
Figure 5.19: Data for the magnetic Faraday rotation experiment with each polarized/non-polarized data set plotted next to each other. The rotation values are plotted as rotation per pass with the weighted average of polarized/non-polarized points given by the dashed line. The theoretical expected value and errors are shown as well. The data is taken at a wavelength of 633 nm.

Wavelength	Weighted average polarized	Weighted average non-Polarized
405 nm	11±2 nrad/pass	14±3 nrad/pass
633 nm	6±1 nrad/pass	7±1 nrad/pass

Table 5.5: Weighted averages of the results for both laser wavelengths. The number of laser passes in the cavity is divided out.

5.6 Systematic effects

The results of the experiment did not agree with the theory, several systematic effects were studied to see if any interfered with or compensated for the signal.
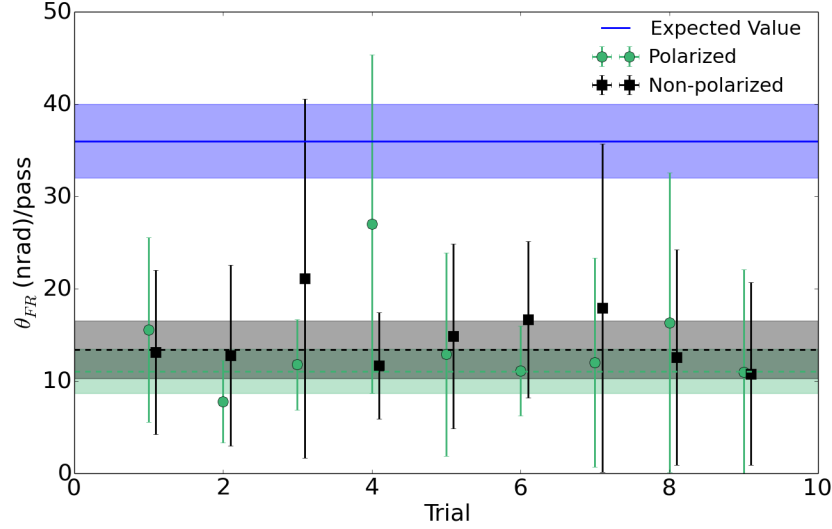
Figure 5.20: Data for the magnetic Faraday rotation experiment with each polarized/non-polarized data set plotted next to each other. The rotation values are plotted as rotation per pass with the weighted average of polarized/non-polarized points given by the dashed line. The theoretical expected value and errors are shown as well. The data is taken at a wavelength of 405 nm.

5.6.1 Different B_0 holding field magnitudes

For both wavelengths the magnitude of the static magnetic field was changed. Changing the holding field also changes the resonance frequency for NMR and the transverse field amplitude, though the spin flipping and P_{eq} are not affected for the range tested. The experiment was repeated with the same conditions and the results are listed in Table.(5.6)

The different field amplitudes did not have an effect on the measurements.

5.6.2 Different spin flip rate

Additional data was taken at a spin flipping frequency of 5 mHz meaning a spin flip every 100 s. The more frequent spin flips mean the P_{eq} is lower because there is less time to repump the ^{3}He in-between flips. At this rate $P_{eq} \sim 7\%$ which keeps

Wavelength (nm)	B_0 amplitude (G)	Polarized (nrad)	Non-Polarized (nrad)
633	15.0	110(55)	90(90)
	10.1	80(51)	121(78)
405	15.1	150(97)	123(102)

Table 5.6: Polarized and non-polarized measurements for different static magnetic field amplitudes.

the expected value in the measurable range. Fig.(5.21) shows the plotted data. No measurements were taken with a spin modulation of 5 mHz for the 405 nm laser. The results are the same as the main experiment.
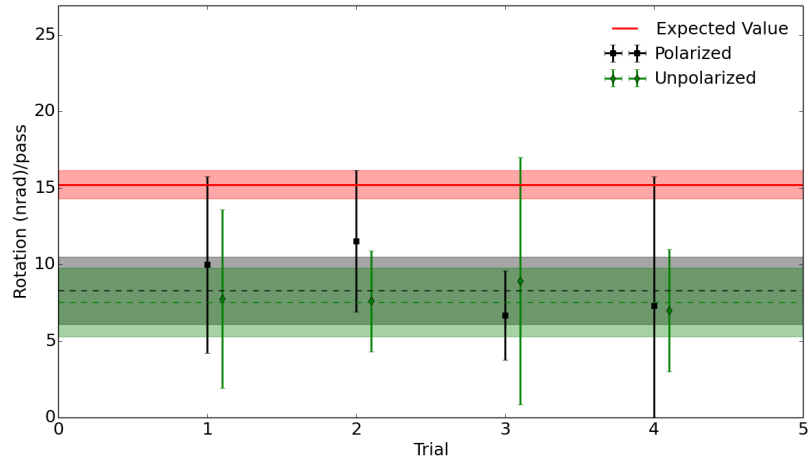
Figure 5.21: Data for the magnetic Faraday rotation experiment with each polarized/non-polarized data set plotted next to each other. The rotation values are plotted as rotation per pass with the weighted average of polarized/non-polarized points given by the dashed line. Data for 633 nm wavelength and a spin flipping frequency of 5 mHz.

5.6.3 Effect of Target Polarization

Before reaching the equilibrium value the ^{3}He polarization decays from a higher value. Though the value is changing it remains larger than P_{eq} for a few hours and

the lock-in amplifiers should theoretically be able to measure the changing quantity. The average expected Faraday rotation over the range is 1 μrad which is well above the noise floor. The rotations measured are compared with the theory calculation in Table.(5.7).
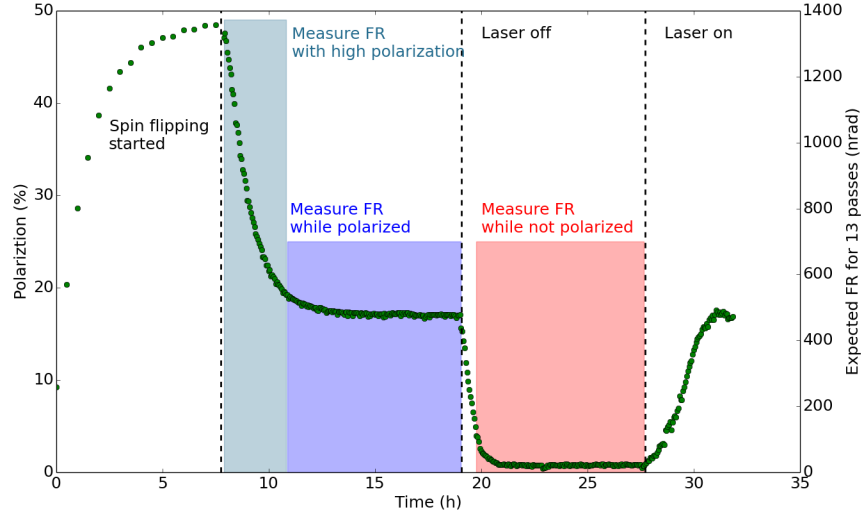
Figure 5.22: Collect lock-in amplifer voltage data while the polarization is decaying from a high value in addition to when the polarization is stable.

Wavelength (nm)	Average polarization (%)	Polarized (nrad)	Theory (nrad)
	36.0	36(9)	1024(11)
633	35.2	127(75)	1002(11)
	30.1	106(36)	857(11)
	29.5	97(60)	840(11)
405	34.7	203(120)	988(11)

Table 5.7: Faraday rotation at high polarization while it decays compared with theory prediction.

5.6.4 Varying probe laser power

It has been shown that an intense laser light inside a medium can induce birefringence via its own electric field [100, 101]. This means a laser propagating in certain media will undergo a change in its ellipticity without an external field present. This effect is usually largest for high power laser light or a laser that has been focused to a small beam width. While the probe lasers are not within such domains to test whether this self induced birefringence could be affecting the small rotations the laser power is varied. The range of initial laser intensities incident upon the cavity and the measured rotations are given in Table.(5.8). The data shows that self induced birefringence is not observed as expected.

Wavelength (nm)	Intensity (mW)	Polarized (nrad)	Non-polarized (nrad)
	28	125(53)	116(79)
	10	101(58)	161(80)
633	2	111(63)	97(60)
	0.5	316(152)	241(104)
	0.23	538(320)	432(240)
405	40	131(83)	133(79)
	10	523(688)	423(224)

Table 5.8: Faraday rotation from the ^{3}He target for varying probe laser power

While the gyromagnetic Faraday effect was not measured and varying the probe laser power seemed to have no affect on the measurements it did highlight that for very low power incident on the detector the sensitivity of the system gets worse. This is likely the system approaching the shot noise limit. Once again, it is useful to check the Fourier transform of the output voltage of the PEM lock-in amplifier. For smaller probe laser powers the Fourier transform appears to have a better sensitivity and a lower noise floor. Fig.(5.23) shows the FT for a laser power before the cavity of 10 mW vs 0.47 mW and the lower noise on the 0.47 mW plot reveals a systematic error that was hidden before. The peak at the spin flipping frequency corresponds to light from the pumping laser leaking into the detector. The Faraday rotation either comes from a resonant effect from the Rb atoms or a tiny difference between

119

the different states of circular polarization due to the quarter wave plates not being perfectly aligned. Either way, the 100 nrad signal disappears when another iris and bandpass filter are added before the analyzing optics to completely block out the pumping laser light.
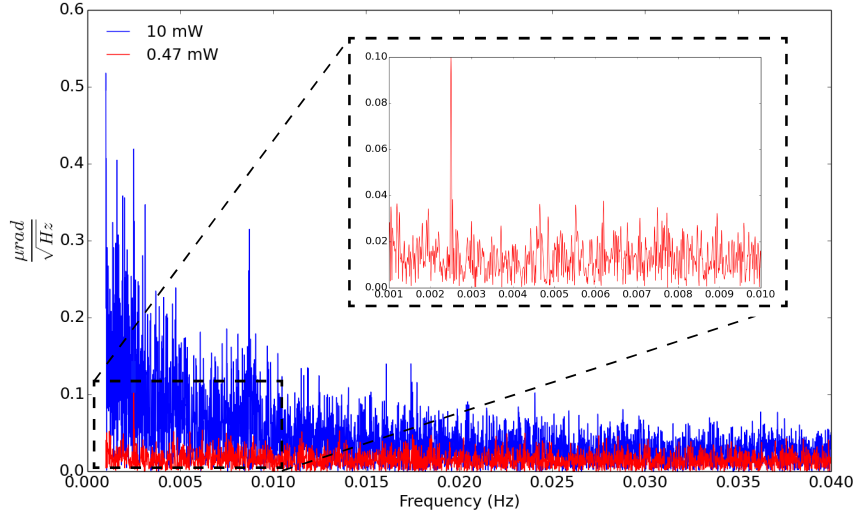
Figure 5.23: Lomb-Scargle periodogram of the output of the PEM lock-in for different probe laser powers. The lower laser power usually has reduced noise. The zoomed in section shows a false signal at the spin flipping frequency due to the pumping laser light.

5.6.5 Misalignment of the spins with the laser

There is a systematic error related to the the spins not being aligned exactly with the laser path. The Faraday rotation is only affected by components along the direction of propagation of the light. A small tilt of the spins means that a smaller signal will be expected, because the spins are aligned with the static magnetic holding field this error can be estimated by measuring the angle between the magnetic field and laser, see Fig.(5.24). To do this, a compass is built by hanging magnets inside the Helmholtz coils. The compass is suspended just above the laser path and once it is

120

stabilized a line is drawn beneath the compass along the direction it points and the angle between the laser path and this line is measured. The angle is measured to be $\phi = 2.25 \pm 0.5$ deg, yielding a component along the laser path $\cos(2.25°) = 0.999$ times smaller, essentially the same as no misalignment. There are additional angles associated with the laser being reflected inside the cavity. At worst the beam moves 1.27 cm over 2 m meaning the angle is much less than 1 deg which is again, essentially no misalingment.
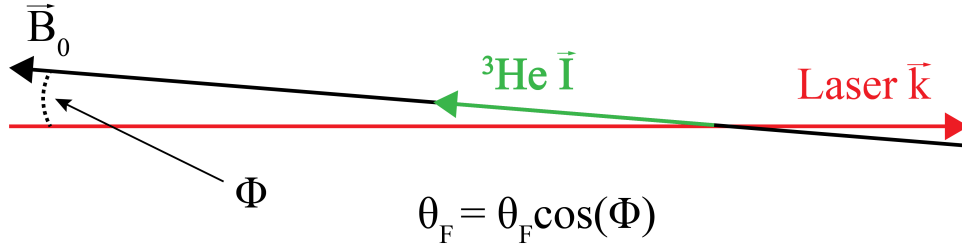
Figure 5.24: The helium spins are aligned with the magnetic field and at a small tilt with the propagation direction of the laser. This will reduce the rotation measured by a factor of $\cos(\phi)$.

5.6.6 Resonant Faraday rotation from Rb and K

The SEOP cell contains rubidium and potassium atoms in addition to the ^{3}He gas. Both Rb and K have atomic transitions which generate comparatively enormous Faraday rotations [8, 20] to the magnetic Faraday effect. The densities of the two alkali metals in the target chamber should be almost undetectable because of the temperature gradient from the pumping chamber, but to confirm this and see if a systematic offset occurs due to the atoms the resonant Faraday rotation is measured. A 10 cm long glass cylinder filled with Rb is placed in the setup with the SEOP cell removed. The glass cell is encased inside an oven that can be connected to the air flow heating system. A tuneable diode laser (Newport Velocity TLB-6000) that has a resolution of 1 picometer and can reach the 780.241 nm resonance replaces the laser for the ^{3}He experiment. The wavelength is measured by using a beam splitter to direct the laser into a Burleigh WA-1500 wavemeter. The Rb cell is heated to 70°

C and the laser is tuned to the resonance to confirm its location, for a magnetic field amplitude of 4 G a rotation of nearly 100 millirad was measured. The cell is then cooled to room temperature and the wavelength of the laser is scanned across the resonance measuring the Faraday rotation. Fig.(5.25) shows the results compared with a theory calculation from the formula(Eq.5.2) given in Ref.[8].

$$\theta = \frac{1}{6}[\text{Rb}]lr_e\lambda_0^2\mu_B B/h\left[\frac{\lambda^2}{c}\left(\frac{0.35}{(\Delta\lambda)_{1/2}^2} + \frac{0.7}{(\Delta\lambda)_{3/2}^2}\right) \pm \frac{h}{k_B T}\left(\frac{1}{(\Delta\lambda)_{1/2}} - \frac{1}{(\Delta\lambda)_{3/2}}\right)\right]$$
(5.2)

Where l is the length, B is the magnetic field and $(\Delta\lambda)_{1/2}, (\Delta\lambda)_{3/2}$ are the wavelength detunings from the D1 and D2 resonances (only the D2 is relevant for this measurement). Most of the data agrees with theory, the diode laser was not very stable at the picometer level so the difference between the rotations measured below the resonance and the theory is most likely due to wavelength shifting during the measurement period. At room temperature the density of the Rb is between 10^9 and 10^{10} per cubic centimeter. This provides confirmation that the triple modulation setup can measure resonant Faraday rotation and further confirmation that it can measure from a collection of gaseous atoms. The next step is to replace the helium cell and try to measure resonant Faraday rotation from Rb in the target chamber while the pumping chamber is heated to 230°. Under these conditions no Faraday rotation was observed in the target chamber indicating a Rb density below the sensitivity level. Furthermore, because the wavelengths for the experiment are so far away from the resonances of Rb the expected value is below a detectable level even if the densities were as high as the sample cell. Meaning the resonances likely have no effect on the magnetic Faraday effect measurements.

Similarly for potassium, a 10 cm long glass cell filled with only K is utilized with a small oven connected to the forced air system. A tuneable external cavity diode laser (Moglabs) that can reach both the 404.721 nm and 404.413 nm resonances replaces the laser for the ³He experiment. The wavelength is measured via fiber by a Bristol 671A-VIS wavemeter. The oven is heated to 190° and the laser is scanned across the resonance while the Faraday rotation is measured. Fig.(5.26) shows the result.

There is also a response from the K 404.721 nm resonance in the target chamber
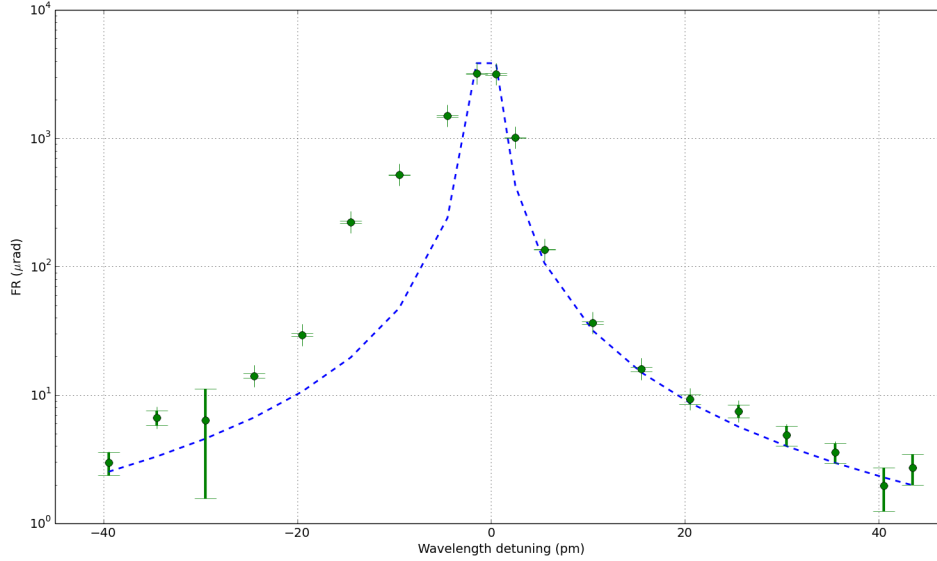
Figure 5.25: Resonant Faraday rotation from the 780 nm D2 resonance of Rb plotted as a function of wavelength detuning. The measurements were performed on a 10 cm long glass cell from Thorlabs filled with Rb. The dashed curve is a fit from Eq.5.2.

of the hybrid SEOP cell Vivian. The resonance curve is measured again with the cell in place and the alkali vapours polarized. In the cell geometry used, the densities of the alkali vapours in the target chamber are typically too low to measure resonant Faraday rotation but it is measureable in Vivian and is correlated with the alkali polarization. Because the K atoms are inside the classical magnetic field produced by the polarized ^{3}He atoms, when the ECDL is tuned close to the resonance there should be a signal at the spin modulation frequency from the oscillating magnetic field. With the ECDL 1 pm away from the K resonance, polarized/unpolarized data sets are collected in the same manner as the magnetic Faraday effect experiment. The results are shown in Fig.(5.27)

This is an additional test that shows the system can measure small optical rotation angles and can measure an effect correlated with the spin modulation of the ^{3}He nuclear spins.
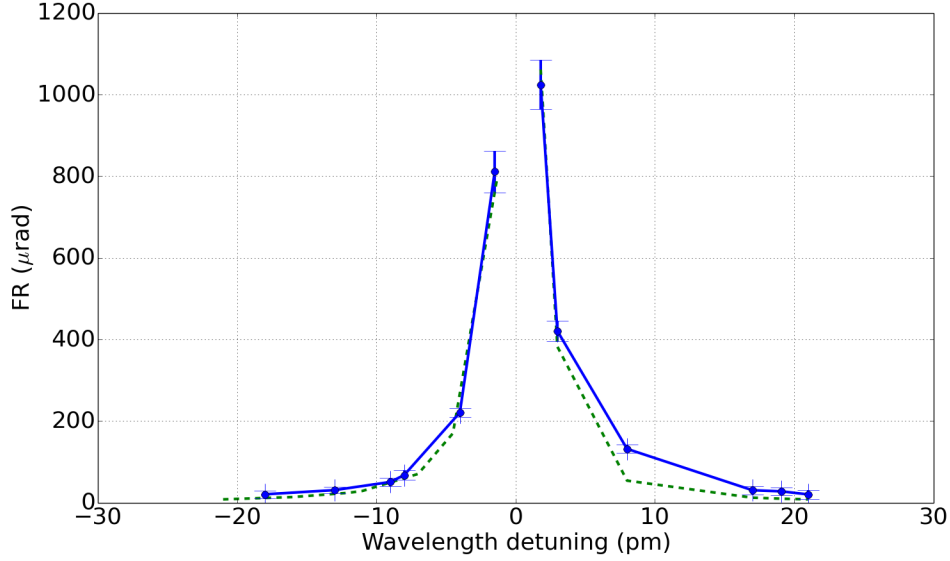
Figure 5.26: Resonant Faraday rotation from the 404.721 nm resonance of K plotted as a function of wavelength detuning. The measurements were performed on a 10 cm long glass cell from Thorlabs filled with K. The dashed curve is a fit from Eq.5.2.

5.6.7   Errors due to the ^{3}He classical magnetic field.

The polarized ^{3}He nuclear spins have a bulk magnetization associated with them. This magnetization, in addition to being the origin of the gyromagnetic Faraday effect, produces a classical magnetic field. This field is part of an effective field that results in additional Zeeman shifts in Rb that can be detected with EPR and is the field that is detected with the NMR pickup coils. The field will cause systematic errors as the glass windows of the cell and the gases inside will experience a regular Faraday effect from being inside it. Moreover, this classic magnetic field is modulated at the same frequency as the spin flipping. The magnitude of the field is easy to calculate for the volume and polarization, the magnetization is given by $M = N\mu_{He}\mu_0 P_{He}$ and the pumping chamber can be modeled as a uniformly magnetized sphere and the target chamber a uniformly magnetized long cylinder. The Verdet constants of Corning 1723 aluminosilicate glass, helium [102], and nitrogen [35] are known so the Faraday rotation from each of these can be estimated. The contribution
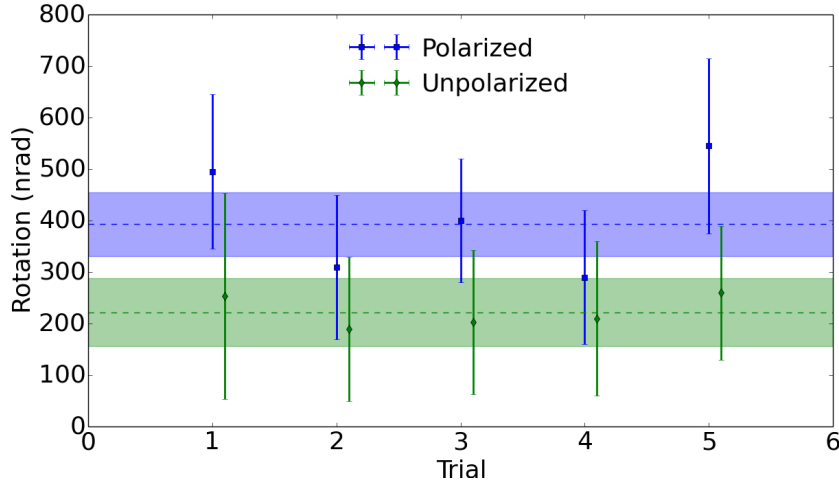
Figure 5.27: Resonant Faraday rotation from the 404.721 nm resonance of K due to the classical magnetic field of the polarized ^{3}He atoms.

from Rb and K can be estimated from the resonant Faraday rotation data. The results for the classical magnetic field produced by ^{3}He polarized to 17% are shown in Table.(5.9)

Wavelength	Laser Passes		Windows	He	N$_2$	Rb
633 nm	13	V (nrad /(mG cm)):	3.15	0.0005	0.002	N/A
		Rotation (nrad):	29.3	0.3	0.1	10^{-6}
405 nm	9	V (nrad /(mG cm)):	7.70	0.001	0.004	N/A
		Rotation (nrad):	49.6	0.5	0.2	10^{-6}

Table 5.9: Upper limits on the Faraday rotation from the glass windows and gases in the cell due to the magnetic field (1.13 mG) from ^{3}He polarized to 17% in the 40 cm long target chamber.

The only source that is not negligible is the Faraday rotation from the end windows. Under the experimental conditions, for 633 nm the estimate is 29 nrad which is below what can be detected as at best the errors in the rotation measurements are larger than this value. In principle, because the windows have some thickness and

the magnetic field from a magnetized cylinder drops off very quickly after the length the average field over the windows could be smaller leading to a smaller Faraday rotation. For 405 nm, the estimate is 49.6 nrad due to the $1/\lambda^2$ dependence of the Verdet constant. Again, this is covered by the typical errors during the experimental runs. It is possible the Faraday rotation from the end windows is contributing to the errors and is the reason they are larger for the blue light.

5.7 Future improvements

There are many improvements that could be made to the existing setup or added to a new setup that could improve the sensitivity of the experiment to measure the magnetic Faraday effect of ^{3}He. One of the limiting factors in the experiment is the helium polarization. The constant spin flipping reduces it due to AFP losses and the need to keep it as high as possible leads to the slow flipping rate and measuring with long time constants at a small frequency. The optical pumping rate has been improved to near the limit and additional 795 nm laser power or a narrower linewidth should not result in significant polarization gains. While the AFP losses are cell dependent, they are also partially due to the static magnetic field gradients. Improving the magnetic fields to reduce gradients and further stabilize them will result in smaller amount of polarization lost per flip leading to high equilibrium polarization values and a larger expected signal. This will also allow for faster spin modulation and measuring at a higher frequency for shorter amounts of time all of which should reduce noise in the experiment. The current field is generated by a pair of Helmholtz coils, adding additional coils in a structure around them will allow magnetic fields to be added to cancel or reduce gradients.

Reducing the noise in the laser is another possibility for the current setup. Incorporating a homodyne interferometry system may reduce the phase and intensity noise in the laser resulting in a smaller noise floor. The probe laser would be split before the detector and then directed back onto the same path so the two beams interfere and reduce the noise. The interferometer would used with a Guidestar laser stabilization system to ensure the beam remains in the same position.

Further improvements rely on building a new ^{3}He target. The cavity method used to increase the signal size is limited by the end windows of the multipass SEOP cell not being optically flat and not coated with an anti-reflective coating for all the wavelengths used. A different cell design, one with larger windows that can be attached and remain optically flat, could be used with a better multipass cavity and reach hundreds of bounces leading to a factor of 10 increase in signal size. A purely cylindrical shaped helium cell can have half the density at similar polarization to the Jefferson National Lab style cell currently used. An even more advanced design would consist of a chamber with a Fabry-Perot cavity inside that can be filled with polarized ^{3}He. A well made cavity can have several hundred thousand laser bounces for a factor of 10^4 increase in the expected rotation which could make up for the loss in density such a chamber would have. A setup such as this could also measure the magnetic Faraday effect as a function of density.

Finally, polarized atomic hydrogen may provide a different system to look for the effect. Through state selection with magnetic fields an atomic hydrogen beam can be polarized with near 100% efficiency. The resulting polarized gas can be collected and stored in a target, with a strong magnetic field (1 kG) and a cold enough gas (100 mK) the target is nearly stable with a very long lifetime. The density of the gas can be as high as 10^{14}(atom/cm^3). The important part being that the electrons in the gas are polarized, and since the electron has a magnetic moment roughly 800 times the magnitude of the helium atom this will result in a increase in the expected signal size from the magnetic Faraday effect. Thus, the polarized hydrogen gas functions as an electron gas target. With a target of the same length as a the helium cell and taking into account the change in density, polarization, and magnetic moment an increase by a factor of 4 can be expected, leading to an optical rotation of 140 nrad for a single pass configuration. However, with no glass windows on the storage cell an addition of a multipass cavity with 100 passes would be possible. Similarly a Fabry-Perot cavity could be put in place, and staying away from wavelengths that are absorbing achieve 10**4 passes making the optical rotation signal trivially easy to measure.

5.8 Summary and conclusions

The gyromagnetic Faraday effect is an optical rotation that is generated solely from a magnetic interaction with an electromagnetic wave. It is a pure magnetic interaction that unlike other electric Faraday effects is independent of the frequency of the electromagnetic wave. It offers a method for a unique polarization monitor for spin polarized targets and a test for the proposed properties of dark matter in a terrestrial dark matter detection experiment. ^{3}He, hyper-polarized via spin exchange optical pumping, provides the perfect system to look for the effect even though the expected signal size is minuscule. Using a triple modulation polarimetry setup, that has a sensitivity below the level of the expected magnetic Faraday rotation from ^{3}He, in combination with a multipass cavity and ^{3}He target numerous studies are conducted to look for the effect. The measurements performed observed no magnetic Faraday effect down to the level of 6 nrad per laser pass when the expected rotation is 35 nrad per pass. The result in surprising and several systematics were examined and none found to have an impact on the measurements. The measured values are so far below what is expected from the theory that various unanticipated explanations are considered to account for this. Phase noise from the magnetic moments of the electrons, which are several orders of magnitude larger than the nuclear magnetic moment, may drown out the accumulated Faraday rotation from the individual helium nuclei. The electrons are in a singlet state and their contributions should cancel but the timescale or the order of the interaction may affect this. Another explanations could be shielding of the nucleus from the photon by some unknown Schiff moment like effect. Although the reason is uncertain, the results of the experiment are clear. The experimental setup with extraordinary angular sensitivity detects no Faraday rotation due to the nuclear spins of the ^{3}He in the first attempted measurement of the magnetic Faraday effect with a polarized target.

Appendices

Cavity Mirror Alignment

To align the cavity mirrors the first step is to have the helium cell in place inside the setup and preferably heated to a high operating temperature. The alignment is easier with the shielding removed so the laser beam spot pattern is visible on the surface of the cell end windows. With the cavity mirrors removed from the optics train, adjust the lens combination until the smallest possible laser beam spot size is achieved just after the cell and before the entrance to the analyzing optics. There are several different initial conditions that work the easiest is to have the single laser pass through the top right quadrant of the first cell window as shown in Fig.(1). If the cell is at the proper tilt the laser beam spot should be near the center of the rear window. Next, place the upstream cavity mirror in the mount and adjust it so the laser passes through the aperture and the aperture is at the 3 o'clock position when facing downstream. So the hole of the mirror will be in line with the top right quadrant of the cell. Adjust the position and laser beam size as needed to ensure the laser does not scrape along the edge of the mirror aperture. Then place the downstream mirror inside the mount and adjust its position until the laser is slightly off the mirrors center. Using the adjustment screws on the kinematic mount, move the laser spot from the reflected beam next to the initial spot as shown in Fig.(2). In this position the first reflection should be going back through the cell and hitting the surface of the upstream mirror. From here adjust the kinematic mount of the upstream mirror until the second reflection goes through the cell and hits the surface of the downstream mirror. There will immediately be more than two beam spots on the surface of each window, keep adjusting the mounts of each mirror until the beam spots form an ellipse. When there is an ellipse on the surface of both windows and mirrors the number of laser passes can be counted by counting the laser beam spots on the surface of a mirror (laser passes = 2×spots). The shape of the ellipse can be controlled by making small alterations with the set screws on the kinematic

129

mounts. Using the downstream mirror, changing the shape of the ellipse combined with small movements of the translation stage in the $\hat{z}$ direction (along the axis of the laser beam) will alter the number of laser passes. In general, reducing the size of the ellipse will help achieve a higher number of passes. When the desired number of passes are achieved the next step is locate the final reflection on the surface of the downstream mirror. Block each individual spot on the surface of the mirror, if the spot is not the final laser pass other spots in the ellipse will disappear. Once the final laser pass is located, rotate the downstream mirror in the mount until the aperture lines up with the final spot. Make small adjustments with the mirrors to maintain the laser beam spot pattern and direct the final lass pass into the analyzing optics and detector.
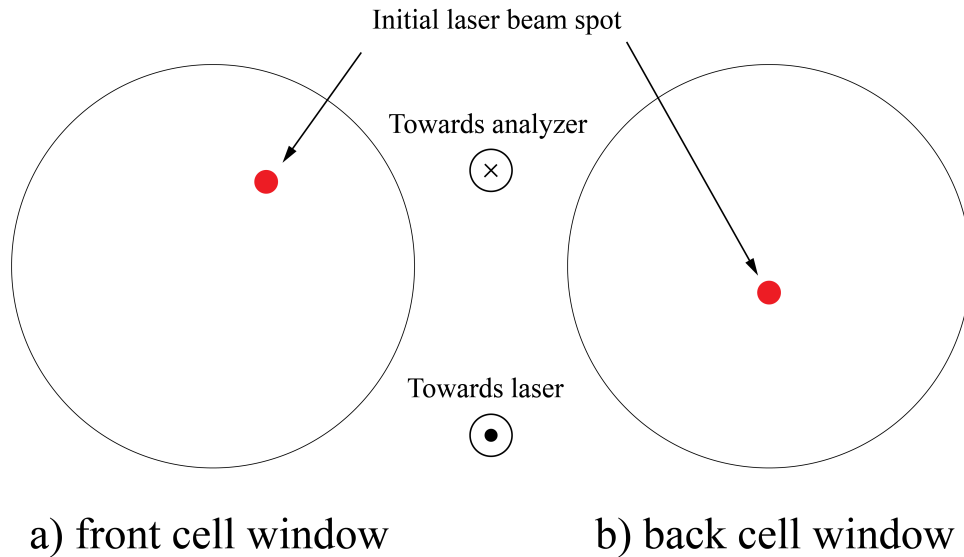
Figure 1: a) initial laser beam spot on front window of the cell. b) initial laser beam spot on back window of the cell

Changing the Pumping Laser Diode

To change the pumping laser diode, first make certain all equipment related to the laser (power supply, water cooler, etc...) are turned off. Unplug the power supply
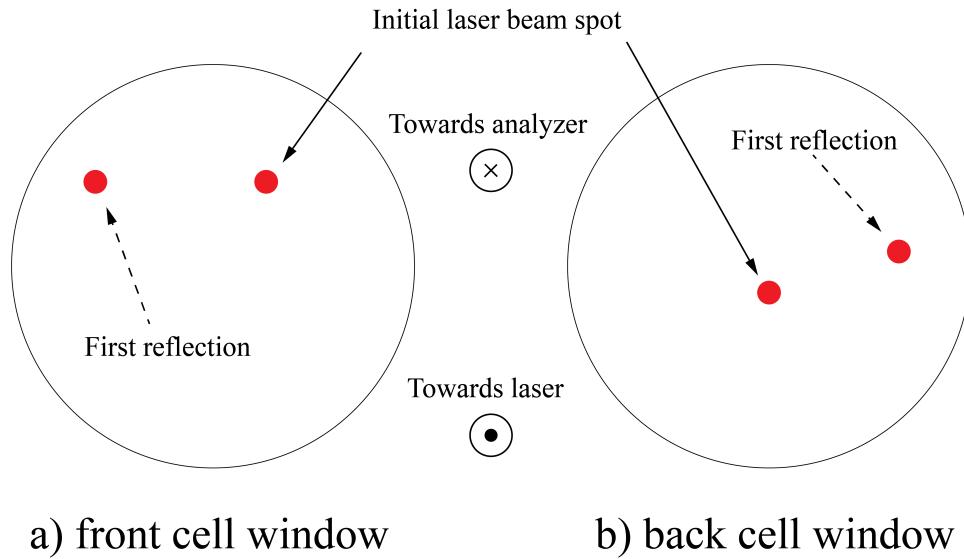
Figure 2: a) first reflection laser beam spot on front window of the cell. b) first reflection laser beam spot on back window of the cell

from the outlet and disconnect the cables connecting the diode to the power supply. Release the clamps on the connections for the water cooling at the base of the diode mount and pull the pipes out of the way. The square base mount has two plastic screws that hold the mount to the translation stage, remove these and lift the base mount from the stage, there will still be a small amount of water inside the diode and mount that needs to be caught with a towel. The bottom of the diode is as shown in Fig.(3), it has 4 screws to connect it to the mount and two ports for the water flow in and out.

Remove the screws located on the bottom of the mount and set aside. Pull the diode, gripping it by its sides, straight up and off the mount being careful to not damage or move the microlens on the front. Setting the old diode aside, place the new diode array in the same configuration on the mount with the water process in and process out matching the corresponding pipe on the mount. Re-attach the screws on the bottom of the mount and tighten them until the diode is secure against the o-rings. Replace the mount on the translation stage with the plastic screws and reconnect the water in and out and the power cables for the power supply.
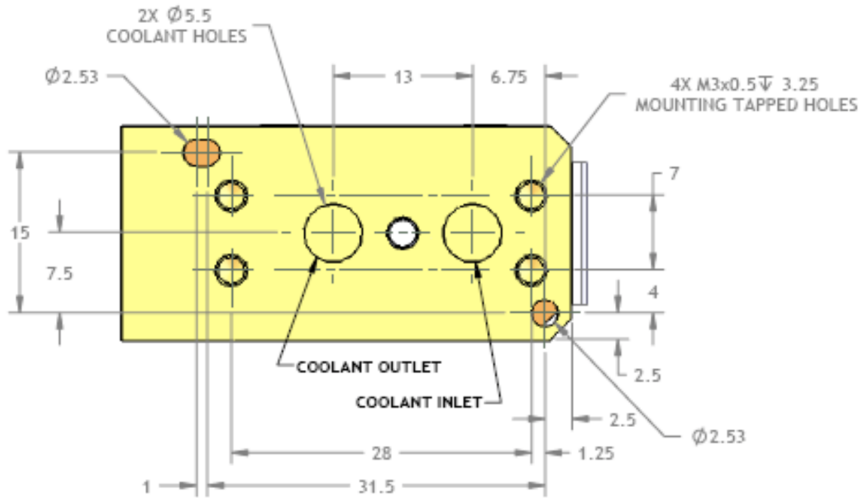
Figure 3: Schematic of the bottom of the nlight pumping laser diode

DAQ electronics settings

Some optimum lock-in amplifier settings to start with when taking precision measurements.

DC lock-in amplifier

- TC: 1-100s, for rotations less than 50 μrad: 500-1000s

- Input Device: FET

- Input Connector Shell: Float

- Coupling: AC

PEM lock-in amplifier

- TC: 40μs-5ms

- Sensitivity: Greater than 2×input voltage

- Output Filter Slope: 24 dB/octave

- Input Device: FET

- Input Connector Shell: Float

- Coupling: AC

Mod lock-in amplifier

- TC: 1-100s, for rotations less than 50 μrad: 500-1000s

- Input Device: Bipolar

- Input Connector Shell: Float

- Coupling: AC, DC for reference frequencies < 1 Hz

The LabView program that controls the three LIAs is called ReadFaradayLockinsRealtimeplot.vi where the length parameter controls the number of data points collected. To view the data files use the program called TripleLockinplot.vi where the only parameter that needs to be typed in is the sensitivity of the PEM LIA. Both are located in the "Triple Modulation folder" on the computer, there is a folder inside called data files where all the data files are stored.

EPR electronics settings

Typical equipment settings when trying to take an EPR measurement.

Function generator HP E4400B

- FM mode: DC coupling

- Amplitude: -5.00 dB to 2.50 dB to change the height of the dispersion curve

- FM deviation: 20 kHz to 100 kHz, affects the height and width of the dispersion curve

Modulation source HP 33120a

- Function: Sine wave

- Frequency: between 200 Hz and 1000 Hz

- Amplitude: 1 V_{pp}

Lock-in DSP 7265

- Measurement channel: X or Y depending on which has larger signal

- TC: 500 μs

- AC gain: as high as possible

- Slope on Filter: 24 dB/octave

The gain settings on the PI box need to be adjusted each time to find the optimum settings to lock the circuit. Similarly the diode used to detect the D2 light needs to be moved as well, the best position is typically 1' from the oven window with the diode angled so it is facing away from the pumping laser light.

NMR electronics settings

Settings for the equipment used to perform NMR on the helium atoms.

Lock-in DSP 7270

- Input Device: FET

- TC: 320 μs

- AC gain: as high as possible

- Sensitivity: Between 200 and 500 mV

- Curve buffer length: 100000 points

- Curve buffer time per point: 0.000130 s

- Curve buffer channels: X and Y

- Curve buffer mode: Fast

Pick up coils pre-Amplifier

- Gain: 5x

- AC coupling

- Mode: Channel A - Channel B

- High pass filter: 300 kHz

- Low pass filter: 5 Hz

Function Generator

- Single linear sweep mode

- Sweep range: 10 kHz

- Sweep time: 6.66 s (also depends on which sweep frequency is needed)

- Retrace time: 0.02 s

- Rest time: 0.02 s

These settings are for a single sweep across the helium resonance and a single return sweep to return the spins to their original orientation. The LabView program to control the electronics and read the curve buffer from the lock-in amplifier is NMRsweepwithcurvebuffer.vi and is located in the "NMR with new laser" folder on the computer. The program controls the settings for the sweep generator and curve buffer and will plot the data from the curve buffer after the sweep is finished. If the store data file option is checked the data file will be stored in the same folder.

Pumping laser electronics settings

<u>DAB</u>

- Operating Voltage: 1.8 V per DAB

- Threshold current: 14 A

- Max operating current: 110 A

- Water cooling flow rate: 0.250 Liter/minute

- Series resistance per bar: 0.005 ohm

The DABs vary for operating temperature, the range is 20-35° C. The temperature should be adjusted on the water cooler until the output wavelength spectrum as viewed with the spectrometer is close to the D1 line of Rb. The 3 nm wide unnarrowed spectrum should ideally be on top of the wavelength for the D1 line but in practice can be up to 3 nm away.

DAB power supply

The power supply is controlled via input pins on the back. The diagram is listed in the manual. The 5 V signal to turn the power supply on is provided by the additional power supply, this also turns on the warning light outside the door. The current is controlled by an input voltage from a Wavetek 81 function generator which is itself controlled by the Lasercontrol.vi LabView program on the "desktop" folder of the computer. 0-3 V DC from the function generator corresponds to 0-105 A current from the power supply.

DAB wavelength spectrum

To tune the wavelength of the DAB use the ocean optics 4000 spectrometer with the fiber input located just after the laser and ideally after an optical diffuser so

light from all the elements can be sampled. Adjusted the fiber until the wavelength spectrum shown is not saturating the spectrometer. The VHG angles can be adjusted with the "APT User" program on the computer which controls the piezo elements on the 6-axis stage. Adjust the angles in large increments until a narrowed spectrum appears, an example is shown in Fig.(4). Then use smaller increments until the spectrum is fully within the narrowed peak.

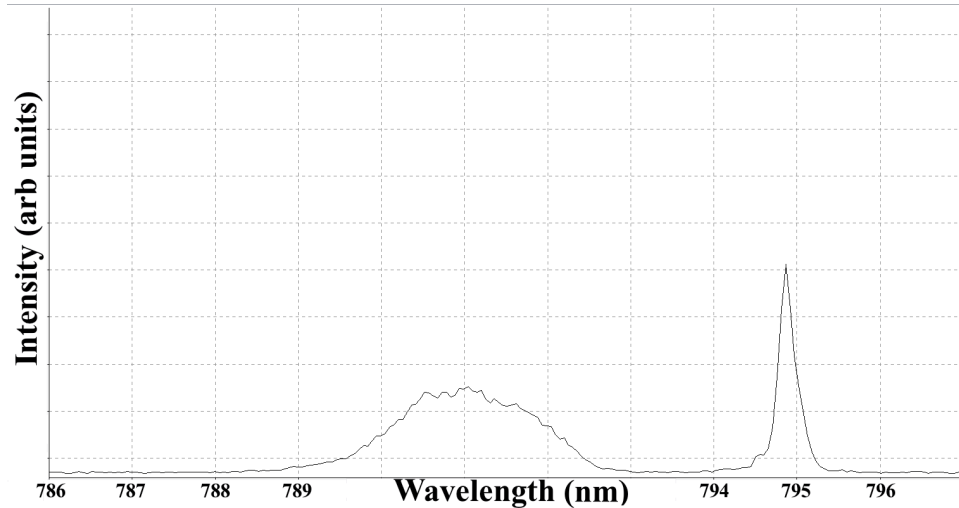Figure 4: Partially narrowed spectrum of a DAB

Moglabs ECDL settings

- Temperature: 24° C

- Operating current 40-60 mA

The piezo element connected to the grating can be controlled in combination with the diode current to find a stable wavelength where the diode no longer switches between modes. Wavelength can be controlled by changing the grating angle and using the fine wavelength adjustment set screw.

Bibliography

1. Gardner, S. Shedding light on dark matter: A Faraday rotation experiment to limit a dark magnetic moment. *Phys. Rev. D* **79,** 055007 (5 Mar. 2009).

2. Graner, B., Chen, Y., Lindahl, E. G. & Heckel, B. R. Reduced Limit on the Permanent Electric Dipole Moment of ^{199}Hg. *Phys. Rev. Lett.* **116,** 161601 (16 Apr. 2016).

3. Smith, F. G. Faraday Rotation of Radio Waves from the Pulsars. *Nature* **220,** 891 (1968).

4. Smiciklas, M., Brown, J. M., Cheuk, L. W., Smullin, S. J. & Romalis, M. V. New Test of Local Lorentz Invariance Using a ^{21}Ne$-$Rb$-$**K** Comagnetometer. *Phys. Rev. Lett.* **107,** 171604 (17 Oct. 2011).

5. Crooker, S. A., Rickel, D. G., Balatsky, A. V. & Smith, D. L. Spectroscopy of spontaneous spin noise as a probe of spin dynamics and magnetic resonance. *Nature* **431,** 49 (2004).

6. T., T., M., F., R., N. & Y., T. Spin Squeezing of a Cold Atomic Ensemble with the Nuclear Spin of One-Half. *Phys. Rev. Lett.* **102,** 033601 (3 Jan. 2009).

7. Buckingham, A. & Stephens, P. Magnetic Optical Activity. *Annual Review of Physical Chemistry* **17,** 399–432 (1966).

8. Vliegen, E. *et al.* Faraday rotation density measurements of optically thick alkali metal vapors. *Nuclear Instruments and Methods in Physics Research A* **460,** 444–450 (Mar. 2001).

9. Wu, Z., Kitano, M., Happer, W., Hou, M. & Daniels, J. Optical determination of alkali metal vapor number density using Faraday rota tion. *Appl. Opt.* **25,** 4483–4492 (Dec. 1986).

10. Korver, A., Thrasher, D., Bulatowicz, M. & Walker, T. G. Synchronous Spin-Exchange Optical Pumping. *Phys. Rev. Lett.* **115,** 253001 (25 Dec. 2015).

11. Kominis, I. K., Kornack, T. W., Allred, J. C. & Romalis, M. V. A subfemtotesla multichannel atomic magnetometer. *Nature* **422,** 596–600 (Apr. 2003).

12. Pennanen, T. S., Ikalainen, S., Lantto, P. & Vaara, J. Nuclear spin optical rotation and Faraday effect in gaseous and liquid water. *The Journal of Chemical Physics* **136,** 184502 (2012).

13. Savukov, I., Lee, S.-K. & Romalis, M. Optical detection of liquid-state NMR. *Nature* **442,** 1021–4 (Sept. 2006).

14. Goldstein, D. *Polarized Light* (Marcel Dekker, 1993).

15. Born, M. & Wolf, E. *Principles of Optics* (Pergamon Press, Oxford, 1970).

16. Faraday, M. Experimental Researches in Electricity. Nineteenth Series. *Phil. Trans. R. Soc. Lond.* **136,** 1–20 (Nov. 1846).

17. Zvezdin, A. K. & Kotov, V. A. *Modern Magnetooptics and Magnetoptical Materials* (Taylor and Francis Group, 1997).

18. Hougen, J. T. Anomalous Faraday Dispersion of O2. *The Journal of Chemical Physics* **32,** 1122–1125 (1960).

19. Hecht, E. *Optics* (Addison-Wesley, 2002).

20. Budker, D. *et al.* Resonant nonlinear magneto-optical effects in atoms. *Rev. Mod. Phys.* **74,** 1153–1201 (4 Nov. 2002).

21. Meriles, C. A. Optical detection of NMR in organic fluids. *Concepts in Magnetic Resonance Part A* **32A,** 79–87 (2008).

22. Barron, L. D. *Molecular Light Scattering and Optical Activity* (Cambridge University Press, 2004).

23. Hogan, C. L. The Ferromagnetic Faraday Effect at Microwave Frequencies and its Applications. *Rev. Mod. Phys.* **25,** 253–262 (1 Jan. 1953).

24. Polder, D. VIII. On the theory of ferromagnetic resonance. **40,** 99–115 (Jan. 1949).

25. Gardner, S. Possibility of Observing Dark Matter via the Gyromagnetic Faraday Effect. *Phys. Rev. Lett.* **100,** 041303 (4 Jan. 2008).

26. Krinchik, G. S. & Chetkin, M. V. Exchange interaction and magneto-optical effects in ferrite garnets. *JETP* **14,** 485 (1962).

27. Krinchik, G. S. & Chetkin, M. V. Faraday effect in yttrium garnet at infrared frequencies. *JETP* **38,** 1643–1644 (1960).

28. Newton, R. *Scattering theory of waves and particles* (McGraw-Hill, 1966).

29. Peskin, M. & Schroeder, D. *An Introduction To Quantum Field Theory* (Avalon Publishing, 1995).

30. S. Gardner and M. Roy, private communication (2017).

31. Low, F. E. Scattering of Light of Very Low Frequency by Systems of Spin. *Phys. Rev.* **96,** 1428–1432 (5 Dec. 1954).

32. Gell-Mann, M. & Goldberger, M. L. Scattering of Low-Energy Photons by Particles of Spin. *Phys. Rev.* **96,** 1433–1438 (5 Dec. 1954).

33. Gardner, S. & Latimer, D. C. Dark matter constraints from a cosmic index of refraction. *Phys. Rev. D* **82,** 063506 (6 Sept. 2010).

34. Zavattini, E. e. a. New PVLAS results and limits on magnetically induced optical rotation and ellipticity in vacuum. *Phys. Rev. D* **77,** 032006 (3 Feb. 2008).

35. Phelps, G. *Magneto-optical Effects and precision measurement physics: Accessing the Magnetic Faraday Effect of Polarized ^3He with a Triple Modulation Technique* PhD thesis (University of Kentucky, 2014).

36. Phelps, G., Abney, J., Broering, M. & Korsch, W. A sensitive Faraday rotation setup using triple modulation. *Review of Scientific Instruments* **86,** 073107 (2015).

37. G. E. Jellison, J. & Modine, F. A. *Handbook of Spectroscopic Ellipsometry* (2003).

38. `http://web.nmsu.edu/{fffd}{fffd}{fffd}kburke/Instrumentation/` `CDPEM.html2013..`

39. Weber, M. J. *Handbook of Optical Materials* (CRC Press, 2003).

40. David, J. e. a. Small Faraday rotation measurement with a Fabry-Perot cavity. *Applied Physics Letters* **66,** 3546–3548 (1995).

41. Chang, C.-Y. & Shy, J.-T. Cavity-enhanced Faraday rotation measurement with auto-balanced photodetection. **54,** 8526 (Oct. 2015).

42. Li, J. *et al.* Shot-noise-limited optical Faraday polarimetry with enhanced laser noise cancelling. *Journal of Applied Physics* **115,** 103101 (2014).

43. Gangopadhyay, P. e. a. Faraday Rotation Measurements on Thin Films of Regioregular Alkyl-Substituted Polythio phene Derivatives. *The Journal of Physical Chemistry C* **112,** 8032–8037 (2008).

44. Friar, J. L., Gibson, B. F., Payne, G. L., Bernstein, A. M. & Chupp, T. E. Neutron polarization in polarized ^{3}He targets. **42,** 2310–2314 (Dec. 1990).

45. Singh, J. T. *et al.* The development of high-performance alkali-hybrid polarized He 3 targets for electron scattering. *Physical Review. C, Nuclear Physics* **91** (May 2015).

46. Ye, Q. *et al.* A high-pressure polarized 3He gas target for nuclear-physics experiments using a polarized photon beam. *The European Physical Journal A* **44,** 55–61. ISSN: 1434-601X (Apr. 2010).

47. Brash, E. J. *et al.* Spin observables in elastic proton scattering from polarized ^{3}He. *Phys. Rev. C* **52,** 807–817 (2 Aug. 1995).

48. Coulter, K. P. *et al.* Neutron polarization with a polarized ^{3}He spin filter. *Nuclear Instruments and Methods in Physics Research A* **288,** 463–466 (Mar. 1990).

49. Ino, T., Muto, S., Masuda, Y., Kim, G. & Skoy, V. R. Development of ^{3}He polarized neutron spin filters at KEK. *Physica B Condensed Matter* **356,** 109–113 (Feb. 2005).

50. Moller, H. E. *et al.* MRI of the lungs using hyperpolarized noble gases. *Magnetic Resonance in Medicine* **47,** 1029–1051 (2002).

141

51. Leawoods, J. C., Yablonskiy, D. A., Saam, B., Gierada, D. S. & Conradi, M. S. Hyperpolarized 3He gas production and MR imaging of the lung. *Concepts in Magnetic Resonance* **13,** 277–293. ISSN: 1099-0534 (2001).

52. Talbot, C., Batz, M., Nacher, P. .-.-J. & Tastevin, G. An accurate optical technique for measuring the nuclear polarisation o f 3 He gas. *Journal of Physics: Conference Series* **294,** 012008 (2011).

53. Colegrove, F. D., Schearer, L. D. & Walters, G. K. Polarization of He^3 Gas by Optical Pumping. *Phys. Rev.* **132,** 2561–2572 (6 Dec. 1963).

54. Hawkins, W. B. & Dicke, R. H. The Polarization of Sodium Atoms. *Phys. Rev.* **91,** 1008–1009 (4 Aug. 1953).

55. Franzen, W. & Emslie, A. G. Atomic Orientation by Optical Pumping. *Phys. Rev.* **108,** 1453–1458 (6 Dec. 1957).

56. Wittke, J. P. & Dicke, R. H. Redetermination of the Hyperfine Splitting in the Ground State of Atomic Hydrogen. *Phys. Rev.* **103,** 620–631 (3 Aug. 1956).

57. Purcell, E. M. & Field, G. B. Influence of Collisions upon Population of Hyperfine States in Hydrogen. **124,** 542 (Nov. 1956).

58. Overhauser, A. W. Polarization of Nuclei in Metals. *Phys. Rev.* **92,** 411–415 (2 Oct. 1953).

59. Carver, T. R. & Slichter, C. P. Experimental Verification of the Overhauser Nuclear Polarization Effect. *Phys. Rev.* **102,** 975–980 (4 May 1956).

60. Chupp, T. E., Wagshul, M. E., Coulter, K. P., McDonald, A. B. & Happer, W. Polarized, high-density, gaseous ^{3}He targets. *Phys. Rev. C* **36,** 2244–2251 (6 Dec. 1987).

61. Gentile, T. R., Nacher, P. J., Saam, B. & Walker, T. G. Optically polarized ^{3}He. *Rev. Mod. Phys.* **89,** 045004 (4 Dec. 2017).

62. W., H. Optical Pumping. *Rev. Mod. Phys.* **44,** 169–249 (2 Apr. 1972).

63. Wu, Z., Walker, T. G. & Happer, W. Spin-Rotation Interaction of Noble-Gas Alkali-Metal Atom Pairs. *Phys. Rev. Lett.* **54,** 1921–1924 (17 Apr. 1985).

64. Babcock, E. *Spin-Exchange Optical Pumping with Alkali-Metal Vapors* PhD thesis (University of Wisconsin-Madison, 2005).

65. Walker, T. G. Estimates of spin-exchange parameters for alkali-metalnoble-gas pairs. *Phys. Rev. A* **40,** 4959–4964 (9 Nov. 1989).

66. Klutz, K. *Studies of polarized and unpolarized 3he in the presence of alkali vapor* PhD thesis (College of William and Mary, 2012).

67. Singh, J. T. *et al.* Development of high-performance alkali-hybrid polarized ^{3}He targets for electron scattering. *Phys. Rev. C* **91,** 055205 (5 May 2015).

68. Chen, W. C., Gentile, T. R., Walker, T. G. & Babcock, E. Spin-exchange optical pumping of ^{3}He with Rb-K mixtures and pure K. *Phys. Rev. A* **75,** 013416 (1 Jan. 2007).

69. Gamblin, R. L. & Carver, T. R. Polarization and Relaxation Processes in He^3 Gas. *Phys. Rev.* **138,** A946–A960 (4A May 1965).

70. Newbury, N. R., Barton, A. S., Cates, G. D., Happer, W. & Middleton, H. Gaseous $^3-^3$He magnetic dipolar spin relaxation. *Phys. Rev. A* **48,** 4411–4420 (6 Dec. 1993).

71. Romalis, M. *Laser polarized 3He target used for a precision measurement of the neutron spin structure* PhD thesis (Princeton, 1997).

72. Larson, B., Häusser, O., Delheij, P. P. J., Whittal, D. M. & Thiessen, D. Optical pumping of Rb in the presence of high-pressure ^{3}He buffer gas. *Phys. Rev. A* **44,** 3108–3118 (5 Sept. 1991).

73. Romalis, M. V., Miron, E. & Cates, G. D. Pressure broadening of Rb D_1 and D_2 lines by ^{3}He, ^{4}He, N_2, and Xe: Line cores and near wings. **56,** 4569–4578 (Dec. 1997).

74. Chen, W. C., Gentile, T. R., Ye, Q., Walker, T. G. & Babcock, E. On the limits of spin-exchange optical pumping of ^{3}He. *Journal of Applied Physics* **116,** 014903 (July 2014).

75. Rabi, I. I., Ramsey, N. F. & Schwinger, J. Use of Rotating Coordinates in Magnetic Resonance Problems. *Rev. Mod. Phys.* **26,** 167–171 (2 Apr. 1954).

76. Rabi, I. I. Space Quantization in a Gyrating Magnetic Field. *Phys. Rev.* **51,** 652–654 (8 Apr. 1937).

77. Cates, G. D., White, D. J., Chien, T.-R., Schaefer, S. R. & Happer, W. Spin relaxation in gases due to inhomogeneous static and oscillating magnetic fields. *Phys. Rev. A* **38,** 5092–5106 (10 Nov. 1988).

78. Singh, J. *Alkali-Hybrid Spin-Exchange Optically-Pumped Polarized 3 He Targets Used for Studying Neutron Structure* PhD thesis (University of Virginia, 2000).

79. Kolarkar, A. *Precision measurements of the neutron electric form factor at high momentum transfers* PhD thesis (University of Kentucky, 2008).

80. Abragam, A. *The Principles of Nuclear Magnetism* (Clarendon Press, 1961).

81. Slichter, C. *Principles of Magnetic Resonance* (Springer Berlin Heidelberg, 2013).

82. Balling, L. C., Hanson, R. J. & Pipkin, F. M. Frequency Shifts in Spin-Exchange Optical Pumping Experiments. *Phys. Rev.* **135** (7AB Sept. 1964).

83. Schaefer, S. R. *et al.* Frequency shifts of the magnetic-resonance spectrum of mixtures of nuclear spin-polarized noble gases and vapors of spin-polarized alkali-metal atoms. *Phys. Rev. A* **39,** 5613–5623 (11 June 1989).

84. Newbury, N. R. *et al.* Polarization-dependent frequency shifts from Rb$-^3$He collisions. *Phys. Rev. A* **48,** 558–568 (1 July 1993).

85. Romalis, M. V. & Cates, G. D. Accurate ^{3}He polarimetry using the Rb Zeeman frequency shift due to the Rb$-^3$He spin-exchange collisions. *Phys. Rev. A* **58,** 3004–3011 (4 Oct. 1998).

86. Balling, L. C., Hanson, R. J. & Pipkin, F. M. Frequency Shifts in Spin-Exchange Optical Pumping Experiments. *Phys. Rev.* **133,** A607–A626 (3A Feb. 1964).

87. Jackson, J. D. *Classical electrodynamics* 3rd ed. (Wiley, New York, NY, 1999).

88. Babcock, E., Nelson, I. A., Kadlecek, S. & Walker, T. G. ^{3}He. *Phys. Rev. A* **71,** 013414 (1 Jan. 2005).

89. Dutta, C. *Measurement of single-target spin asymmetries in the electroproduction of negative pions in the semi-inclusive deep inelastic reaction n(e,e') on a transversely polarized 3He target* PhD thesis (University of Kentucky, 2010).

90. Li, S., Vachaspati, P., Sheng, D., Dural, N. & Romalis, M. V. Optical rotation in excess of 100 rad generated by Rb vapor in a multipass cell. *Phys. Rev. A* **84,** 061403 (6 Dec. 2011).

91. KC, U., Silver, J. A., Hovde, D. C. & Varghese, P. L. Improved multiple-pass Raman spectrometer. *Appl. Opt.* **50,** 4805–4816 (Aug. 2011).

92. Sheng, D., Li, S., Dural, N. & Romalis, M. V. Subfemtotesla Scalar Atomic Magnetometry Using Multipass Cells. *Phys. Rev. Lett.* **110,** 160802 (16 Apr. 2013).

93. Tuzson, B., Mangold, M., Looser, H., Manninen, A. & mmenegger, L. E. Compact multipass optical cell for laser spectroscopy. *Opt. Lett.* **38,** 257–259 (Feb. 2013).

94. White, J. U. Long Optical Paths of Large Aperture. *J. Opt. Soc. Am.* **32,** 285–288 (May 1942).

95. Herriott, D., Kogelnik, H. & Kompfner, R. Off-Axis Paths in Spherical Mirror Interferometers. *Appl. Opt.* **3,** 523–526 (Apr. 1964).

96. McManus, J. B., Kebabian, P. L. & Zahniser, M. S. Astigmatic mirror multipass absorption cells for long-path-length spectroscopy. *Appl. Opt.* **34,** 3336–3348 (June 1995).

97. Silver, J. A. Simple dense-pattern optical multipass cells. *Appl. Opt.* **44,** 6545–6556 (Nov. 2005).

98. *Geant4 Software* `http://geant4.cern.ch/`.

99. Ghosh, G. *Handbook of Optical Constants of Solids: Handbook of Thermo-Optic Coefficients of Opti cal Materials with Applications* (Elsevier Science, 1998).

100. Kielich, S. & Zawodny, R. Laser-beam intensity dependent, optical circular birefringence in crystals. *Optics Communications* **15,** 267–272 (1975).

101. Laser induced birefringence in liquids and solutions. *Proceedings of the Royal Society of London A: Mathematical, Physical and Engineering Sciences* **348,** 525–538 (1976).

102. Cadène, A. *et al.* Faraday and Cotton-Mouton effects of helium at $\lambda = 1064$ nm. *Phys. Rev. A* **88,** 043815 (4 Oct. 2013).

Vita

Personal Information

Name: Josh Abney

Educational Institutions

M.S. Physics
University of Kentucky, Lexington, KY
December 2015

B.S. Physics
University of Kentucky, Lexington, KY
July 2013

Professional Positions

Graduate Research Assistant
University of Kentucky, Lexington, KY
Department of Physics and Astronomy
2013 2018

Graduate Teaching Assistant
University of Kentucky, Lexington, KY
Department of Physics and Astronomy
2013 2014